NACA TN 4280

NATIONAL ADVISORY COMMITTEE FOR AERONAUTICS

TECHNICAL NOTE 4280

PRESSURE DISTRIBUTIONS AT TRANSONIC SPEEDS FOR SLENDER BODIES HAVING VARIOUS AXIAL LOCATIONS OF MAXIMUM DIAMETER

By John B. McDevitt and Robert A. Taylor

Ames Aeronautical Laboratory
Moffett Field, Calif.

Washington
July 1958

NATIONAL ADVISORY COMMITTEE FOR AERONAUTICS

TECHNICAL NOTE 4280

PRESSURE DISTRIBUTIONS AT TRANSONIC SPEEDS FOR SLENDER BODIES HAVING VARIOUS AXIAL LOCATIONS OF MAXIMUM DIAMETER

By John B. McDevitt and Robert A. Taylor

SUMMARY

The measured static-pressure distributions at the model surfaces and in the surrounding flow field are presented for a related series of bodies of revolution having locations of maximum cross-sectional areas at 0.3, 0.4, 0.5, 0.6, and 0.7 of the body length. The data were obtained with the various bodies, all of fineness ratio 12, at zero angle of attack. The Mach number varied from 0.80 to 1.20, and the Reynolds number (based on body length) varied from approximately 23.4×10^6 to 24.6×10^6.

INTRODUCTION

In order to provide experimental data concerning pressure distributions on and near bodies at transonic speeds, a series of related experimental investigations has been initiated in the Ames 14-foot transonic wind tunnel. In a previous report (ref. 1) the experimental pressure distributions at transonic speeds for parabolic-arc bodies of revolution having fineness ratios of 10, 12, and 14 were presented. The present report presents experimental pressure distributions at transonic speeds for a series of bodies of revolution all having fineness ratios of 12, but with various axial locations of maximum cross-sectional area.

NOTATION

C_D	drag coefficient, $\frac{D}{q_\infty l^2}$
$C_{D_{bp}}$	base-pressure drag coefficient (see eq. (5))
C_{D_f}	friction drag coefficient
C_{D_p}	pressure drag coefficient, $C_{D_{sp}} + C_{D_{bp}}$
$C_{D_{sp}}$	surface-pressure drag coefficient (see eq. (4))

C_p	pressure coefficient, $\frac{p - p_\infty}{q_\infty}$
D	drag
D_f	friction drag
d	body diameter
l	body length, measured from nose to point of closure
M_∞	free-stream Mach number
p	local static pressure
q_∞	free-stream dynamic pressure
Re	Reynolds number based on body length l
S	body cross-sectional area normalized by dividing by body length squared, πH^2
u,v	streamwise and radial perturbation velocities normalized by dividing by the free-stream velocity
ξ,η,θ	cylindrical coordinate system (see sketch (a)) where ξ and η are streamwise and radial distances normalized by dividing by the body length l
H	body radius normalized by dividing by the body length l
φ	perturbation velocity potential
$( )'$, $( )''$	first and second derivatives with respect to the normalized streamwise coordinate ξ

Subscripts

b	body base
max	maximum
∞	free-stream conditions

APPARATUS AND MODELS

Tunnel

This investigation was conducted in the Ames 14-foot transonic wind tunnel, which is a closed-return tunnel equipped with a perforated test section permitting continuous operation from subsonic to low supersonic speeds (fig. 1). Each wall of the test section contains 16 longitudinal slots with each slot containing a corrugated strip as indicated in figure 1. The ratio of accumulated slot widths (minus the accumulated widths of the corrugated inserts) to tunnel perimeter in the plane normal to the air stream is equal to 0.054 (usually referred to as the porosity factor).

Models

The bodies of revolution considered in this investigation had axial locations of maximum cross-sectional area at 0.3, 0.4, 0.5, 0.6, and 0.7 of the body length (fig. 2). All of the bodies had a fineness ratio of 12 (the fineness ratio is defined as the ratio of body length, from nose to theoretical point of closure, to maximum body diameter).

The radii for the bodies having locations of maximum cross-sectional areas forward of the midpoint of the body length are given by

$$H = CH_{max}\left[1 - \xi - (1 - \xi)^n\right] \tag{1}$$

and for bodies having maximum cross-sectional areas aft of the midpoint,[1]

$$H = CH_{max}\left(\xi - \xi^n\right) \tag{2}$$

[1]The functional form of equation (2) is identical to that used in reference 2 for the ordinates of a related family of two-dimensional airfoils.

where the coordinate system (dimensionless with respect to body length) is illustrated in sketch (a).

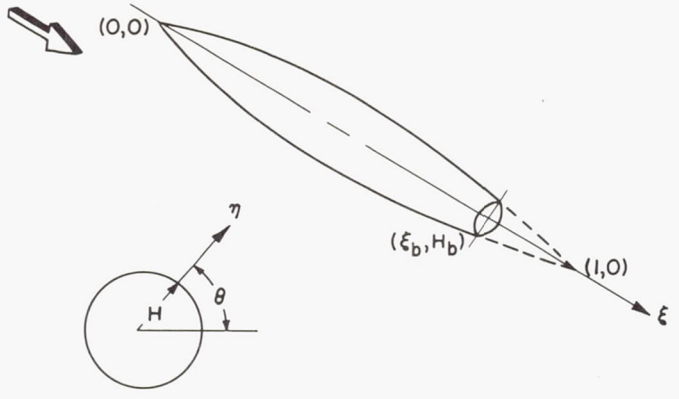

Sketch (a)

The parabolic-arc body of revolution is a special case in the present family of bodies which results when the constant C is set equal to 4 and the exponent n equal to 2.

Values for the constant C and exponent n are tabulated below for the five bodies considered in this investigation:

Location of maximum cross-sectional area, ξ	C	n	H
0.3	1.71	6.03	Eq. (1)
.4	2.36	3.39	Eq. (1)
.5	4.00	2.00	Eq. (1) or (2)
.6	2.36	3.39	Eq. (2)
.7	1.71	6.03	Eq. (2)

In each case the length of the body from nose to theoretical point of closure was 72 inches and the maximum diameter was 6 inches ($H_{max} = 1/24$). All of the bodies were truncated to permit mounting on the sting (see figs. 2 and 3). The base area in all cases was equal to 25 percent of the maximum cross-sectional area.

The variations of the normalized body radius H, and body slope H', are presented in figures 4(a) and 4(b). The variations of the normalized cross-sectional area, S, and the first and second derivatives are shown in figures 4(c), 4(d), and 4(e).

Instrumentation

The axial force was measured by a strain-gage balance enclosed within the model. Multiple-tube manometers using tetrabromoethane (specific gravity = 2.96) were photographed to record the pressure data.

Body-pressure data were obtained by the use of two rows of static-pressure orifices (located on the upper and lower surfaces of the models) extending from nose to base. Additional orifices were located at the model base and in the cavity between the body and sting support in order to measure base pressures.

Local static-pressure data in the flow field below the model were obtained by means of a survey tube (see fig. 5). The survey tube was 1 inch in diameter and contained static-pressure orifices located 90° with respect to a vertical plane passing through the longitudinal axes of the model and survey tube. The experimental data were obtained with the survey tube at various vertical locations with respect to the model center line. Survey-tube locations equal to multiples of the maximum body diameter (d_{max} = 6 in.) were chosen. The first four survey-tube positions are illustrated in figure 5(b).

Movement of the survey tube during model testing was made possible by supporting the survey tube at the model support strut normally used for changing model angle of attack. Arrangement was also provided for the vertical movement of the tension cable in order that the survey tube would always be horizontal.

Additional static pressures were measured at locations slightly ahead of the model nose for one of the models by the use of a special static-pressure prob illustrated in sketch (b).

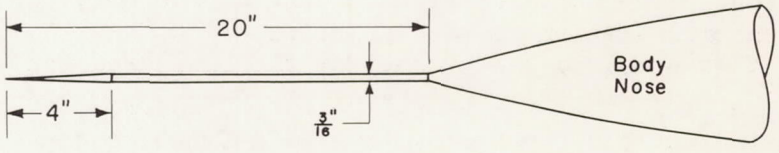

Sketch (b)

TESTS AND PROCEDURE

The models were tested at zero angle of attack through a Mach number range from 0.80 to 1.20. Reynolds number varied from 23.4×10^6 to 24.6×10^6 (based on model length l), see figure 6. To promote transition, No. 60 carborundum grits were cemented on the nose of each model.

The experimental data were not corrected for tunnel-wall interference effects. Considerations of the testing procedure and the data-reduction process indicate that the free-stream Mach numbers are repeatable within approximately ±0.002, the angle of attack is accurate within approximately ±0.1°, and the pressure-coefficient data are repeatable within approximately ±0.005. An additional error in pressure coefficient is due to transverse flow, induced by body curvature, at the survey tube. This error is negligible except for the survey-tube position closest to the body where the absolute value of the error exceeds 0.005 only for the values of ξ where $|S'(\xi)|$ exceeds about 0.022 (see fig. 4(d)).

The force and pressure data were obtained simultaneously and reduced to standard coefficient form. The drag coefficient is defined by the following relationship

$$C_D = \frac{d}{q_\infty l^2} = C_{D_{sp}} + C_{D_{bp}} + C_{D_f} \tag{3}$$

where the component parts are defined as

$$C_{D_{sp}} = \int_0^{\xi_b} C_p S' d\xi \tag{4}$$

$$C_{D_{bp}} = -C_{p_b} S_b \tag{5}$$

$$C_{D_f} = \frac{D_f}{q_\infty l^2} \tag{6}$$

The drag coefficient was calculated by the use of measured pressure distributions. The surface pressure drag of the body, $C_{D_{sp}}$, was obtained by graphical integration of the variation of $C_p S'$ with ξ. The base drag, $C_{D_{bp}}$, is equal to the product of the base area and the measured pressure coefficient at the base (the base pressure coefficient is assumed to be constant across the base). The skin-friction coefficient, C_{D_f}, was estimated by the use of the charts in reference 3.

DATA PRESENTATION

The data presented in this report consist of drag forces, body surface pressures, and field pressures with the models at zero angle of attack. Additional data for parabolic-arc bodies having fineness ratios from 6 to 14 may be obtained from references 1 and 4.

Pressure Data

Surface-pressure distributions and flow field pressure surveys are presented in figures 7 through 11. Although considerable scatter is evident in portions of the pressure data, smooth curves have been faired through the data points except where shock waves are known or believed to exist.

Radial Attenuation of Pressures

The radial attenuation of pressure coefficient can be compared with that predicted by slender-body theory. According to slender-body concepts (see, e.g., refs. 5 to 7) the perturbation potential in the vicinity of the body may be expressed in the form

$$4\pi\varphi(\xi,\eta) = 2S'(\xi)\ln\eta + g(\xi;M_\infty) \tag{7}$$

If the pressure coefficient is related to the velocity perturbations approximately as

$$C_p \approx -2u - v^2 \tag{8}$$

and if equation (7) is differentiated to obtain the perturbation velocities, the pressure coefficient in slender-body theory may be written as

$$C_p = -\frac{S''(\xi)\ln\eta}{\pi} - \frac{[S'(\xi)]^2}{4\pi^2\eta^2} - \frac{g'(\xi;M_\infty)}{2\pi} \tag{9}$$

or

$$C_p + v^2 = C_p + \frac{[S'(\xi)]^2}{4\pi^2\eta^2} = -\frac{S''(\xi)\ln\eta}{\pi} - \frac{g'(\xi;M_\infty)}{2\pi} \tag{10}$$

and the derivative of the quantity $C_p + v^2$ with respect to $\ln\eta$ is

$$\frac{d\left\{C_p + \frac{[S'(\xi)]^2}{4\pi^2\eta^2}\right\}}{d(\ln\eta)} = -\frac{S''(\xi)}{\pi} \tag{11}$$

The experimental results will now be examined with the help of equation (11).[2] In figures 12 through 16 the experimentally determined values for $C_p + \frac{[S'(\xi)]^2}{4\pi^2\eta^2}$ are plotted versus η with a logarithmic horizontal scale. In order for the experimental data to agree with slender-body concepts the data must fall along straight lines with slope equal to $-\frac{S''(\xi)}{\pi}$. Dashed lines with this slope are included in figures 12 through 16 for convenience in analyzing the data (the vertical locations of the dashed lines are arbitrary).

At subsonic speeds the range of agreement with the slender-body concept, equation (9), increases with increasing Mach number. At transonic speeds the agreement is not restricted to the near vicinity of the body but apparently extends to considerable radial distances from the body center line.

Drag Data

The measured drag coefficients (adjusted to represent free-stream static pressure at the model base) and the measured base drag are presented in figure 17 for the various test Mach numbers. Also presented in figure 17 are the computed drag coefficients $C_{D_f} + C_{D_{sp}}$ (see eqs. (4) and (6)). Typical variations of C_pS', required for the numerical evaluation of equation (4), are presented in figures 18 through 22.

Ames Aeronautical Laboratory
National Advisory Committee for Aeronautics
Moffett Field, Calif., Apr. 25, 1958

[2]From experiment C_p is known but v must be approximated by use of the slender-body result. However, the slender-body result for v is exact, within the framework of small-disturbance theory, at the body surface and attenuates rapidly with η so that the slender-body result for v is either sufficiently accurate or is negligible in comparison with C_p.

REFERENCES

1. Taylor, Robert A., and McDevitt, John B.: Pressure Distributions at Transonic Speeds for Parabolic-Arc Bodies of Revolution Having Fineness Ratios of 10, 12, and 14. NACA TN 4234, 1958.

2. Michel, R., Marchand, F., and Le Gallo, J.: Influence de la position du maitre-couple sur les écoulements transsoniques autour de profils a pointes. O.N.E.R.A. Pub. No. 72, 1954.

3. Lee, Dorothy B., and Faget, Maxime A.: Charts Adapted From Van Driest's Turbulent Flat-Plate Theory for Determining Values of Turbulent Aerodynamic Friction and Heat-Transfer Coefficients. NACA TN 3811, 1956.

4. Drougge, Georg: Some Measurements on Bodies of Revolution at Transonic Speeds. Int. Cong. Appl. Mech., Brussels, 1956.

5. Adams, Mac. C., and Sears, W. R.: Slender-Body Theory - Review and Extension. Jour. Aero. Sci., vol. 20, no. 2, Feb. 1953, pp. 85-98.

6. Heaslet, Max. A., and Spreiter, John R.: Three-Dimensional Transonic Flow Theory Applied to Slender Wings and Bodies. NACA TN 3717, 1956.

7. Oswatitsch, K., and Kuene, F.: The Flow Around Bodies of Revolution at Mach Number 1. Proc. Conf. on High-Speed Aeronautics, Polytechnic Institute of Brooklyn, Brooklyn, N.Y., Jan. 20-22, 1955, pp. 113-131.

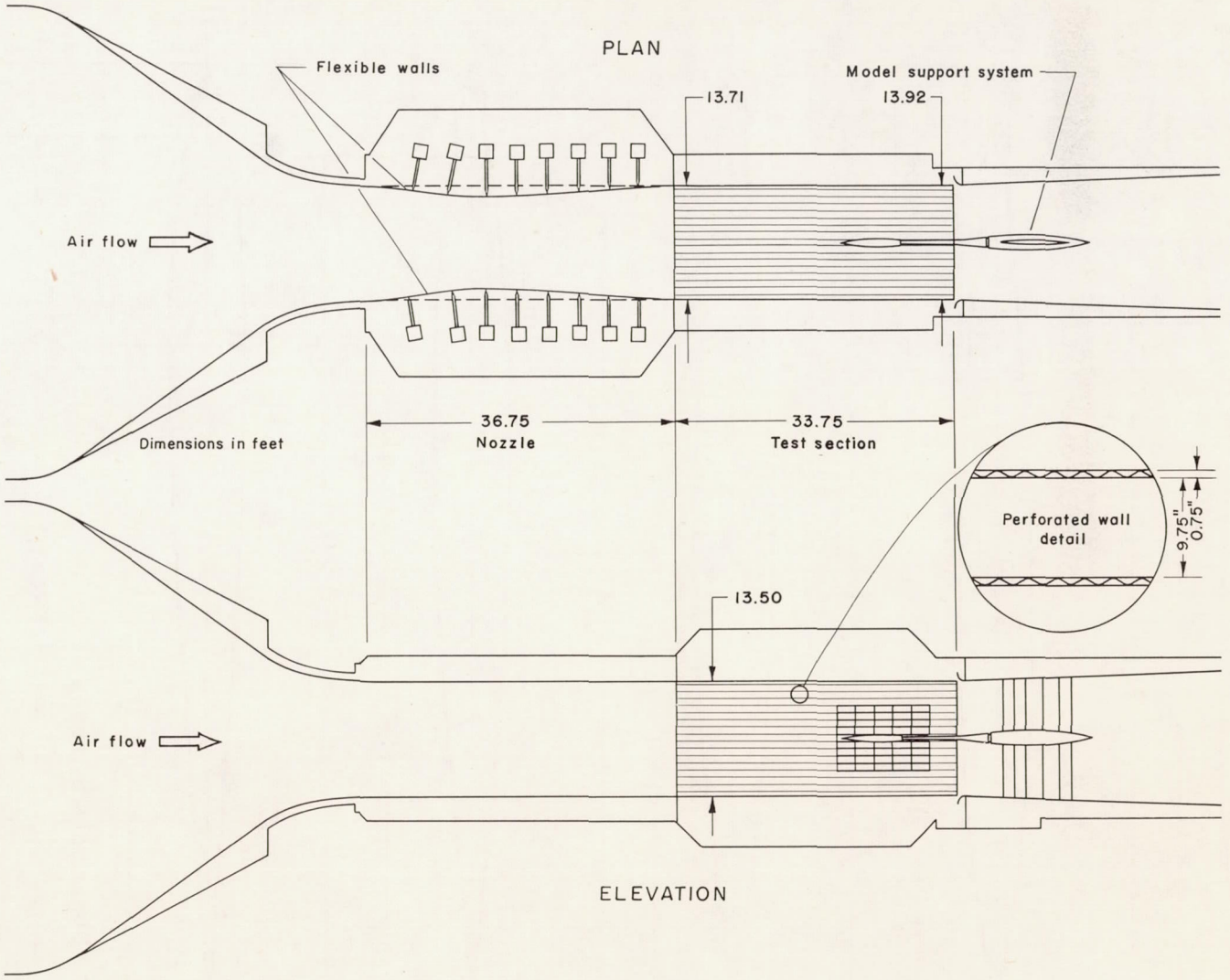

Figure 1.- General arrangement of the test section of the Ames 14-foot transonic wind tunnel.

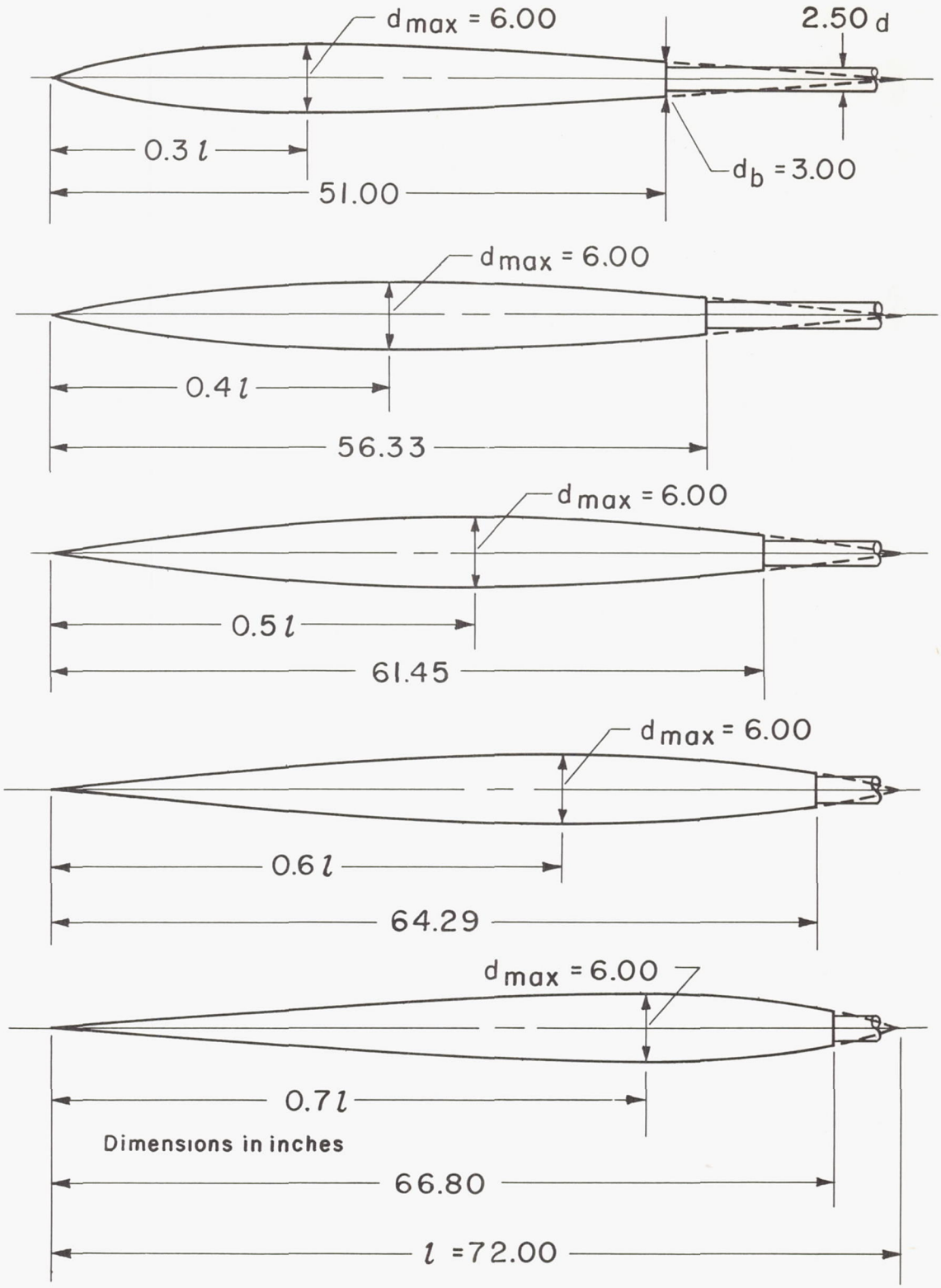

Figure 2.- Basic dimensions of the models.

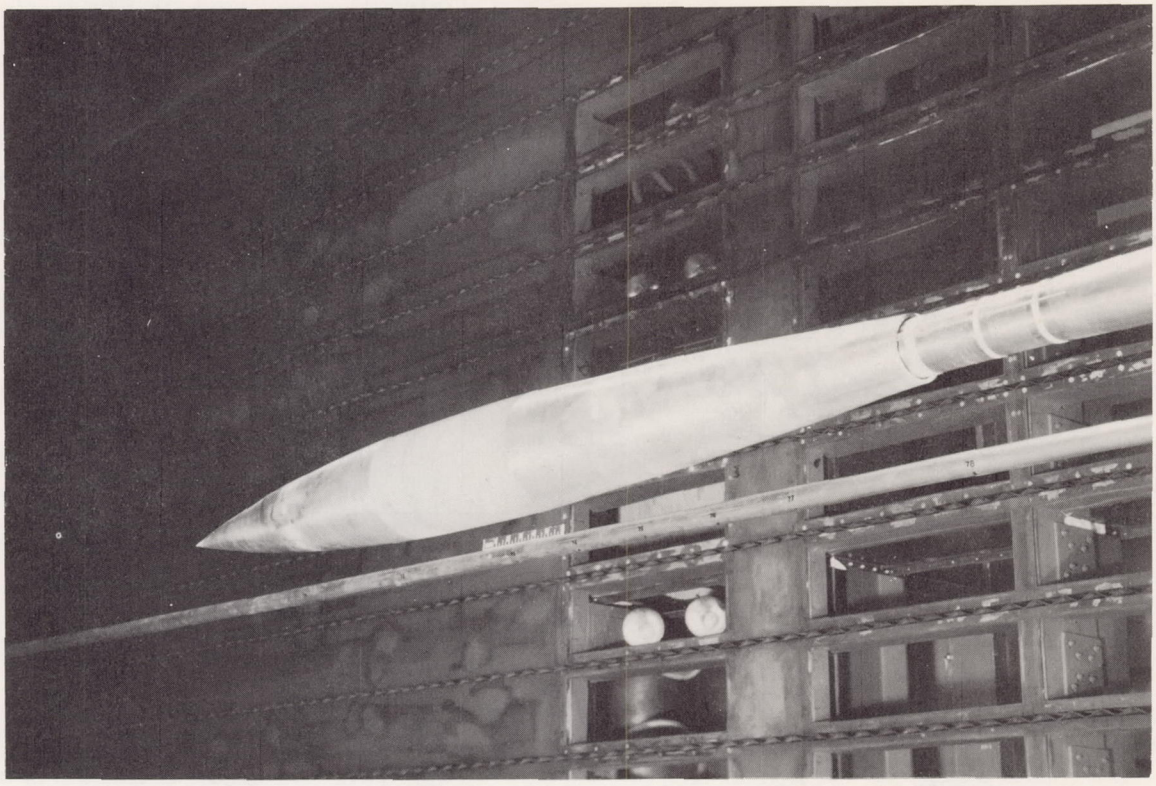

A-22300

Figure 3.- Photograph of body with maximum cross-sectional area located at $\xi = 0.4$.

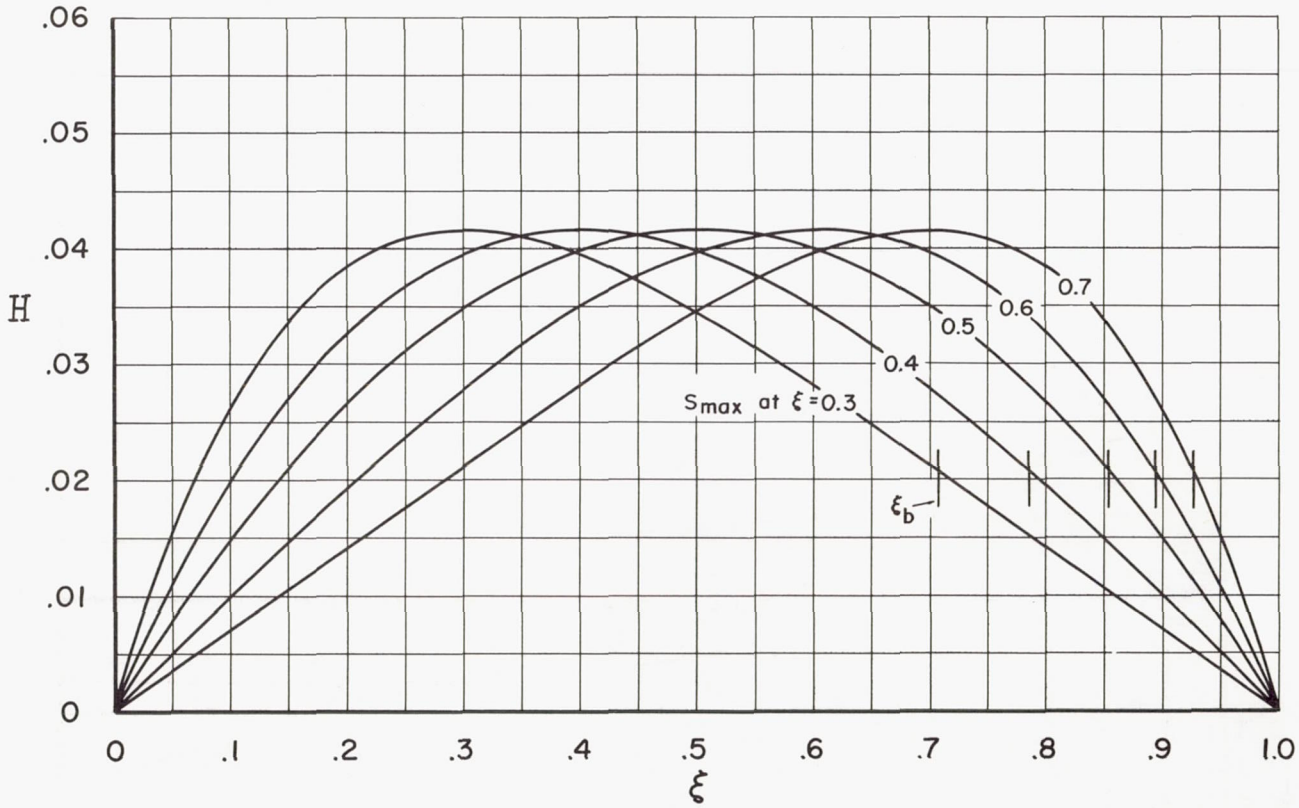

(a) Variation of H with ξ.

Figure 4.- Model geometry.

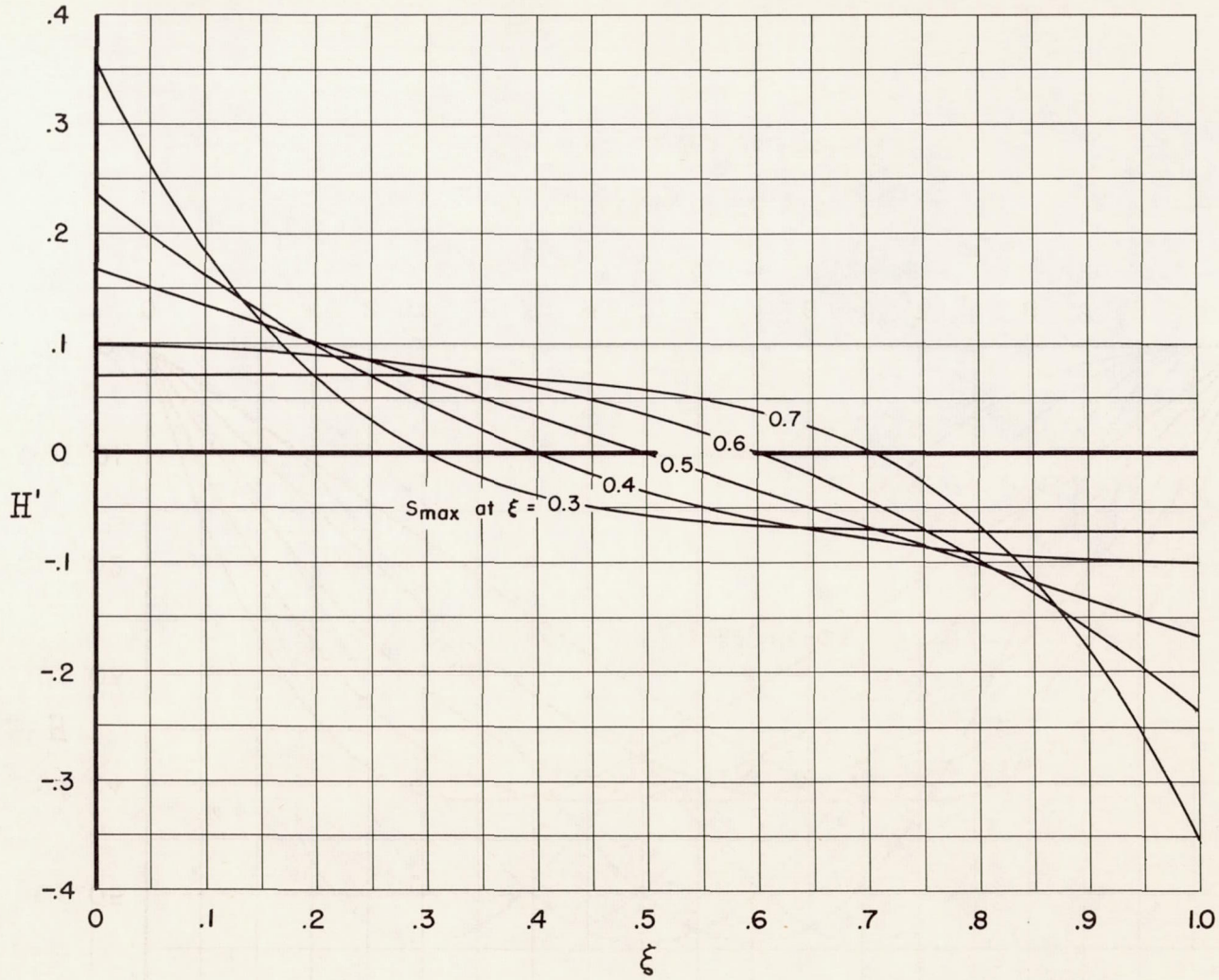

(b) Variation of H' with ξ.

Figure 4.- Continued.

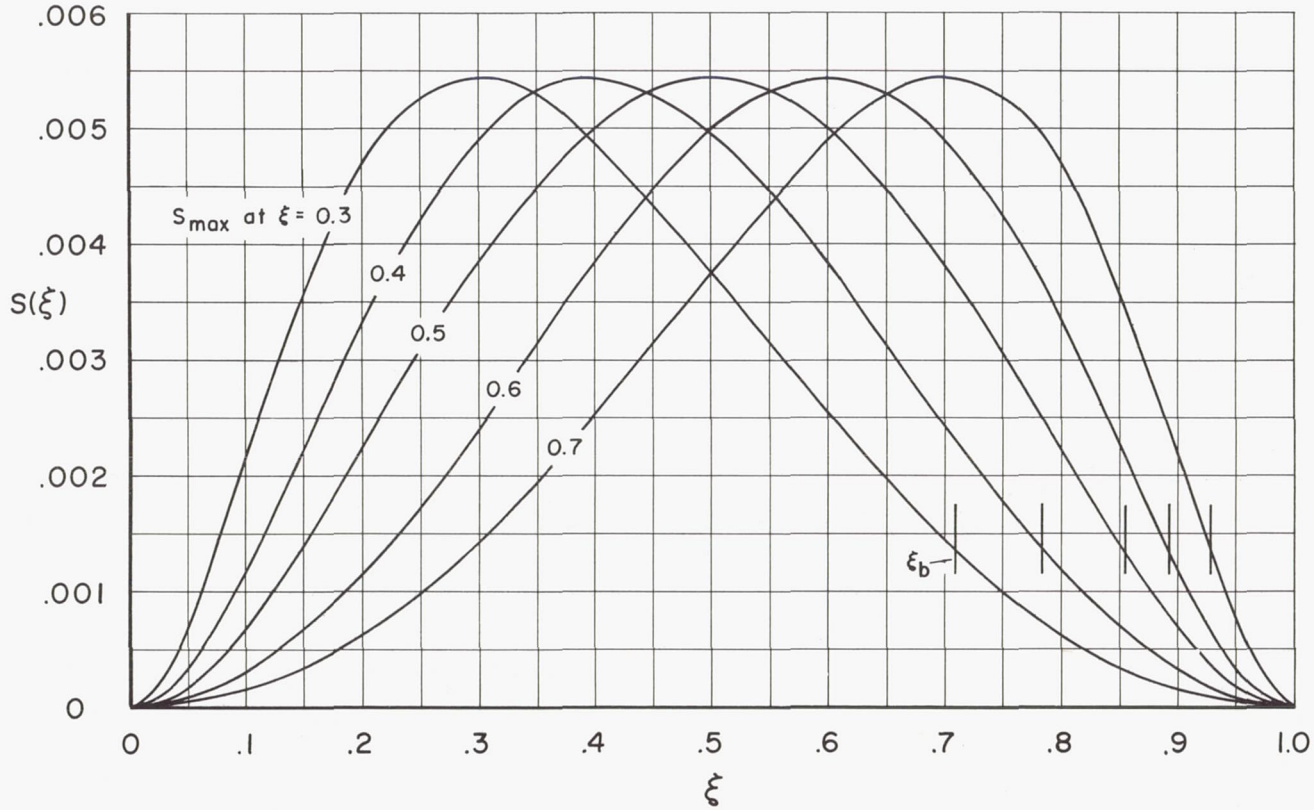

(c) Variation of $S(\xi)$ with ξ.

Figure 4.- Continued.

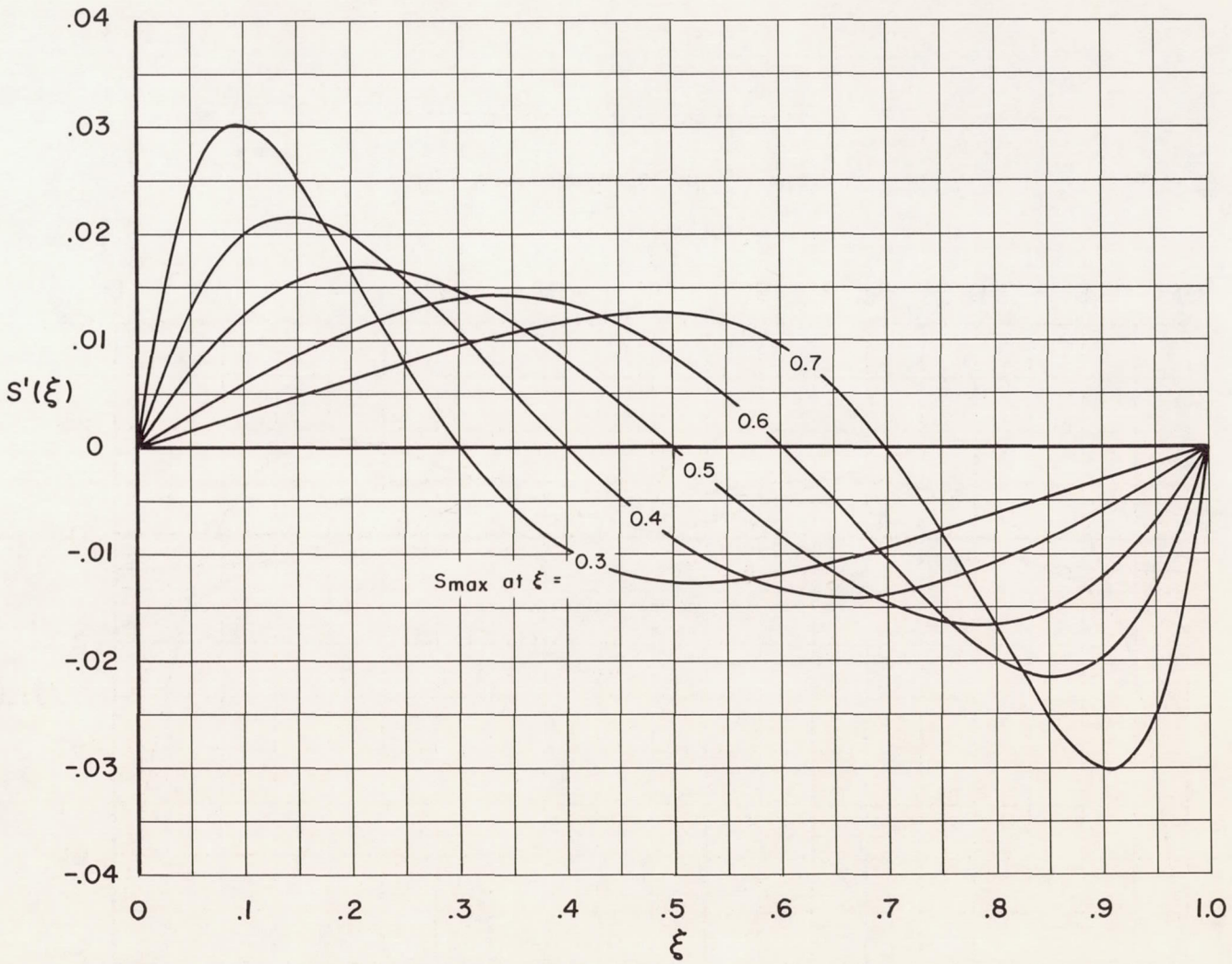

(d) Variation of $S'(\xi)$ with ξ.

Figure 4.- Continued.

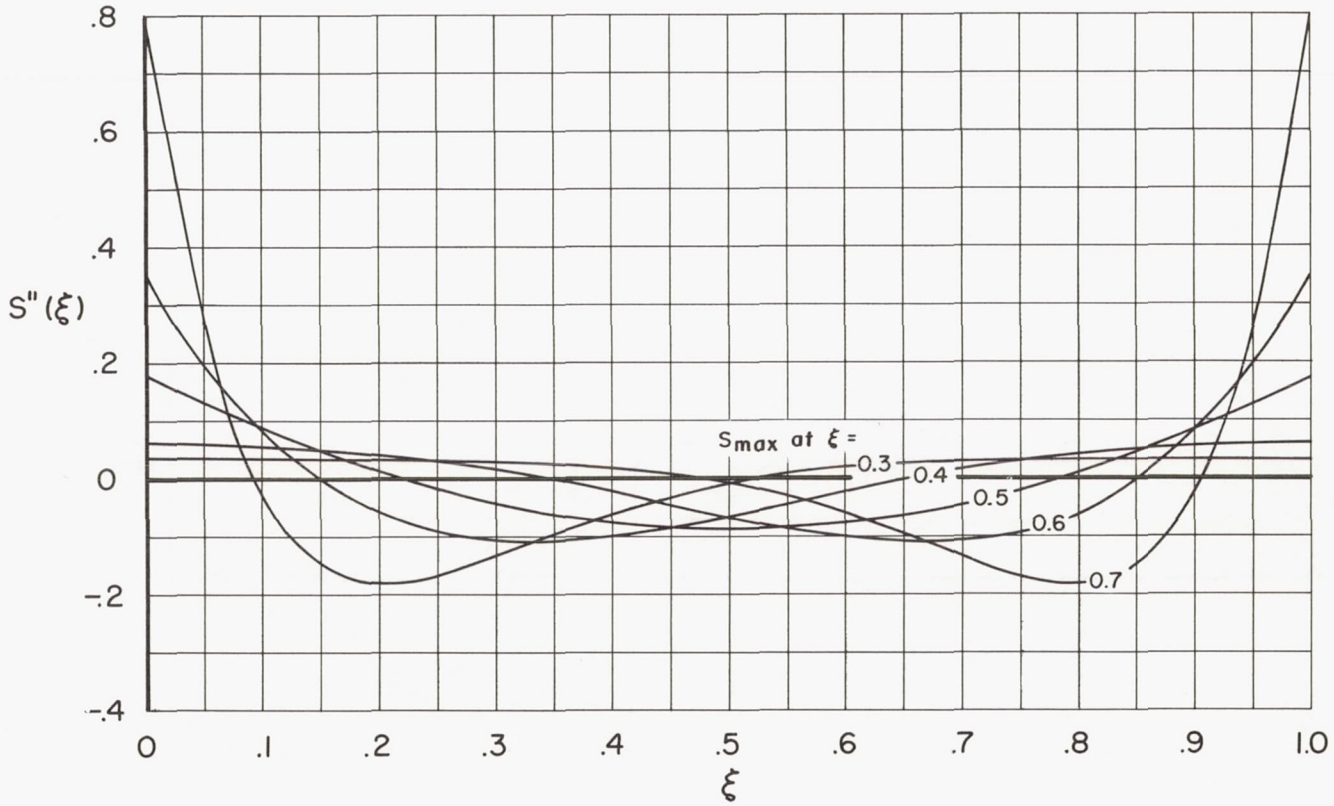

(e) Variation of $S''(\xi)$ with ξ.

Figure 4.- Concluded.

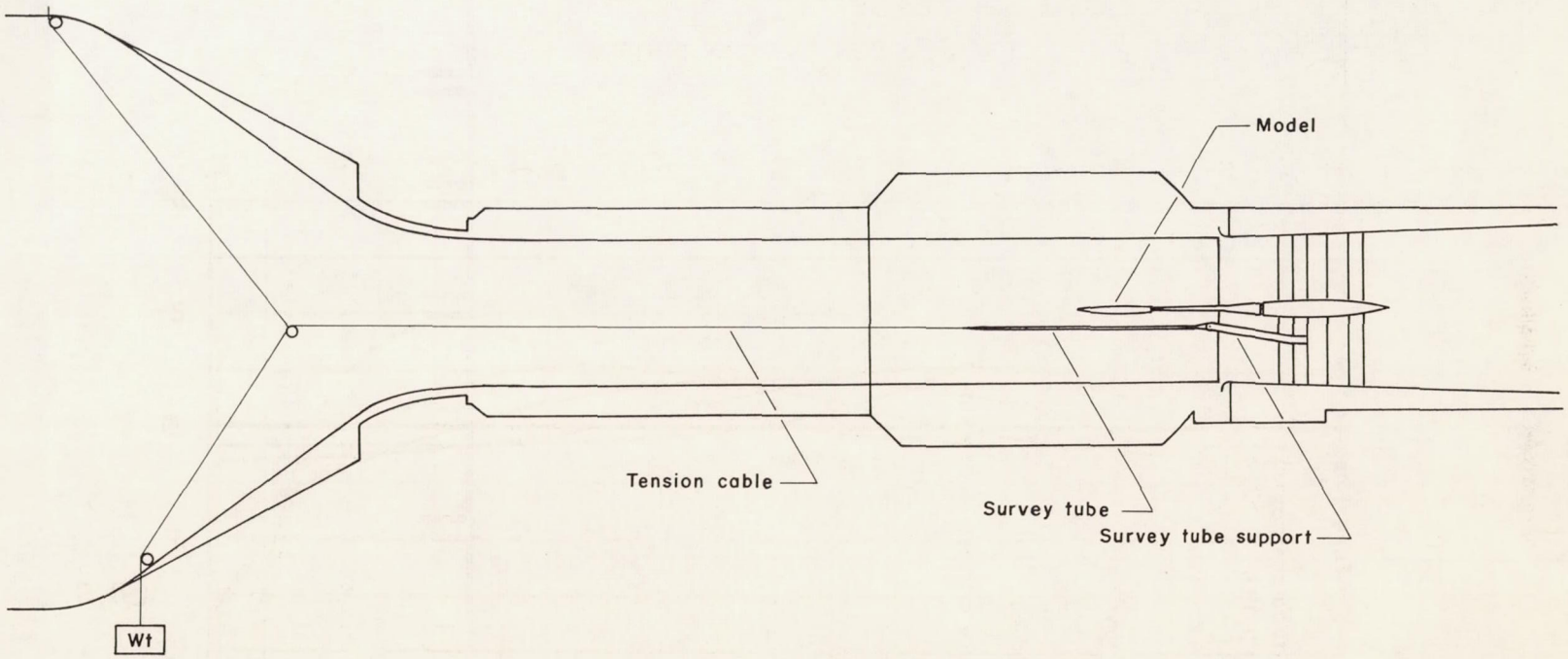

(a) Survey tube support system.

Figure 5.- Schematic drawings of the model and survey tube.

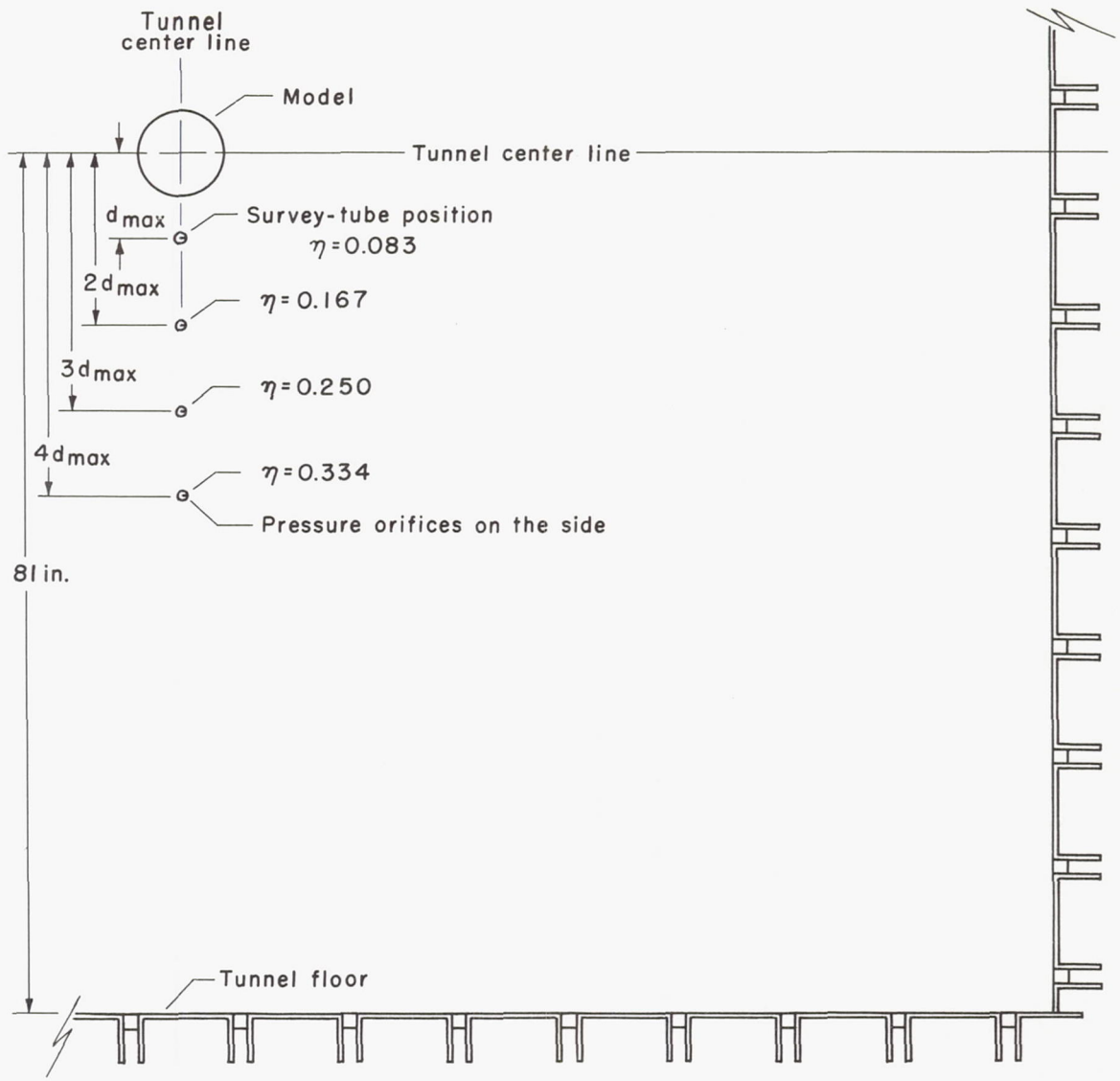

(b) Relative positions of the survey tube with respect to the model.

Figure 5.- Concluded.

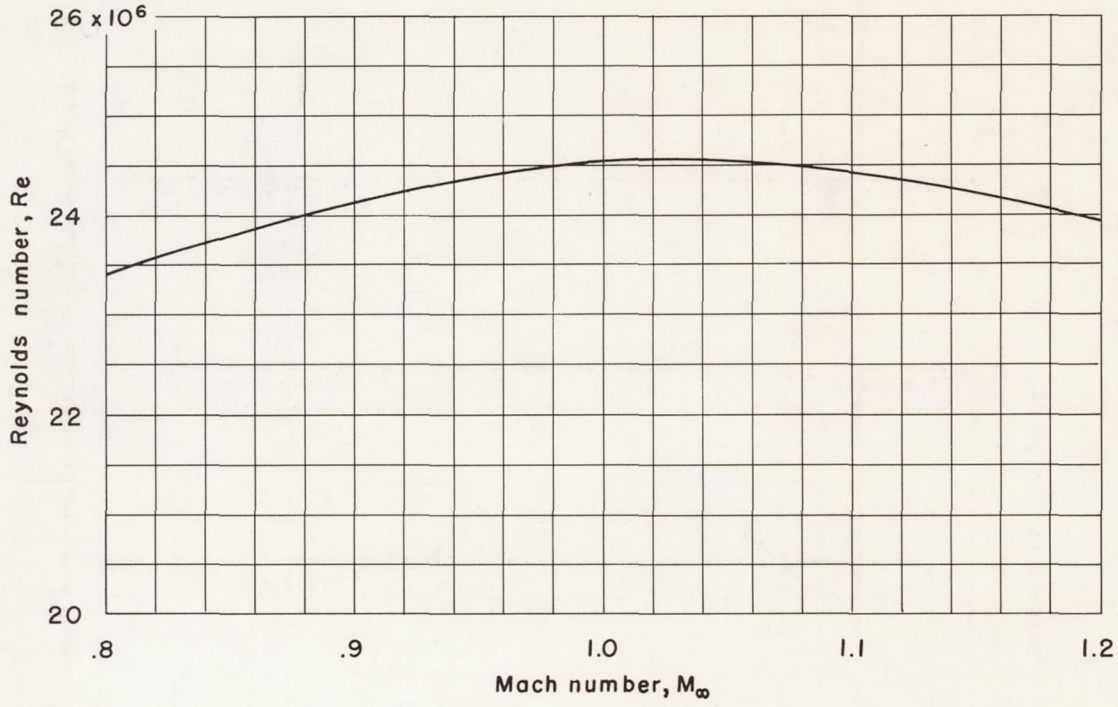

Figure 6.- Variation of Reynolds number with Mach number based on average temperatures.

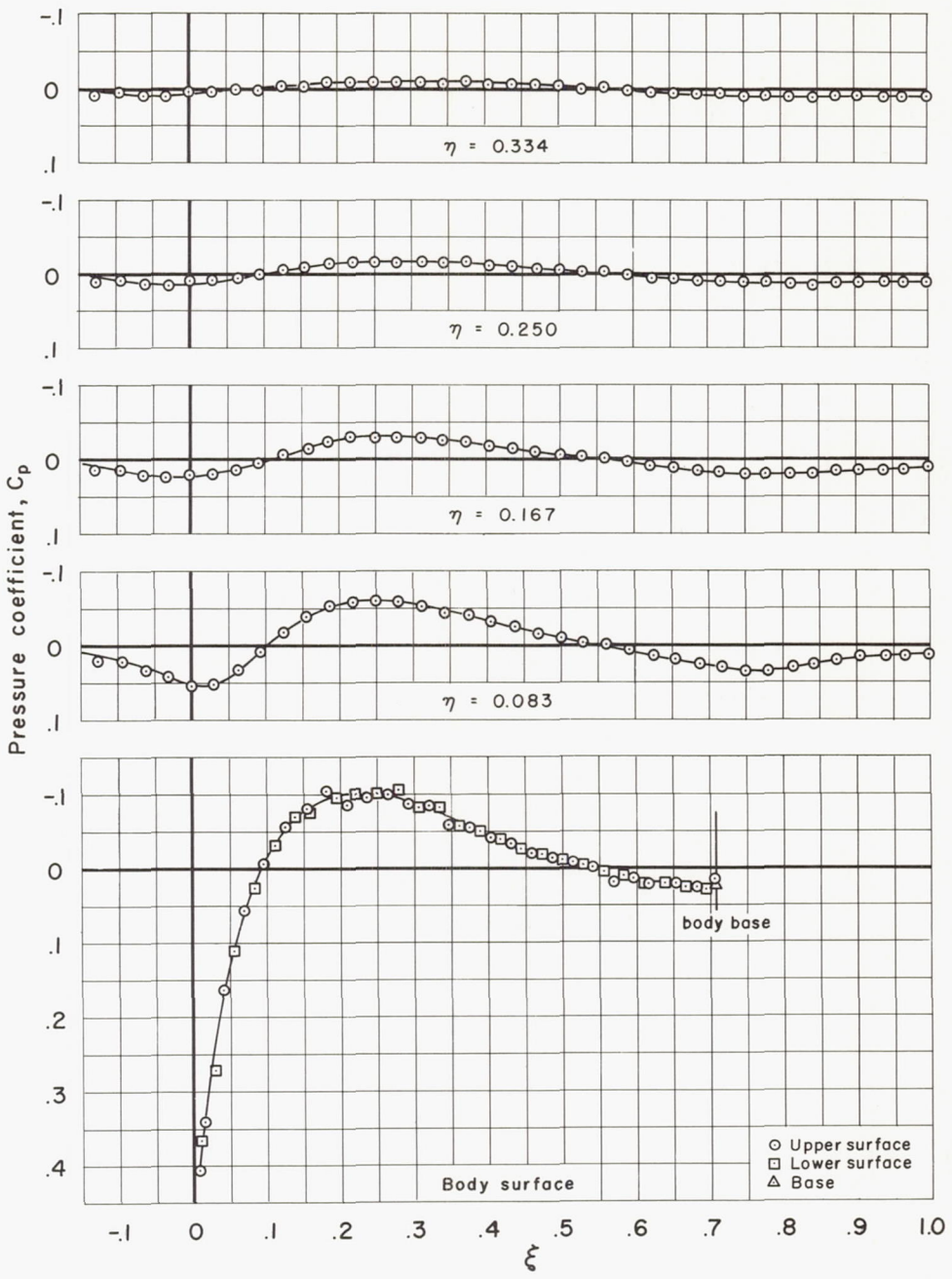

(a) $M_\infty = 0.80$, S_{max} at $\xi = 0.30$

Figure 7.- Experimental pressure distributions for the body with maximum cross-sectional area at $\xi = 0.30$.

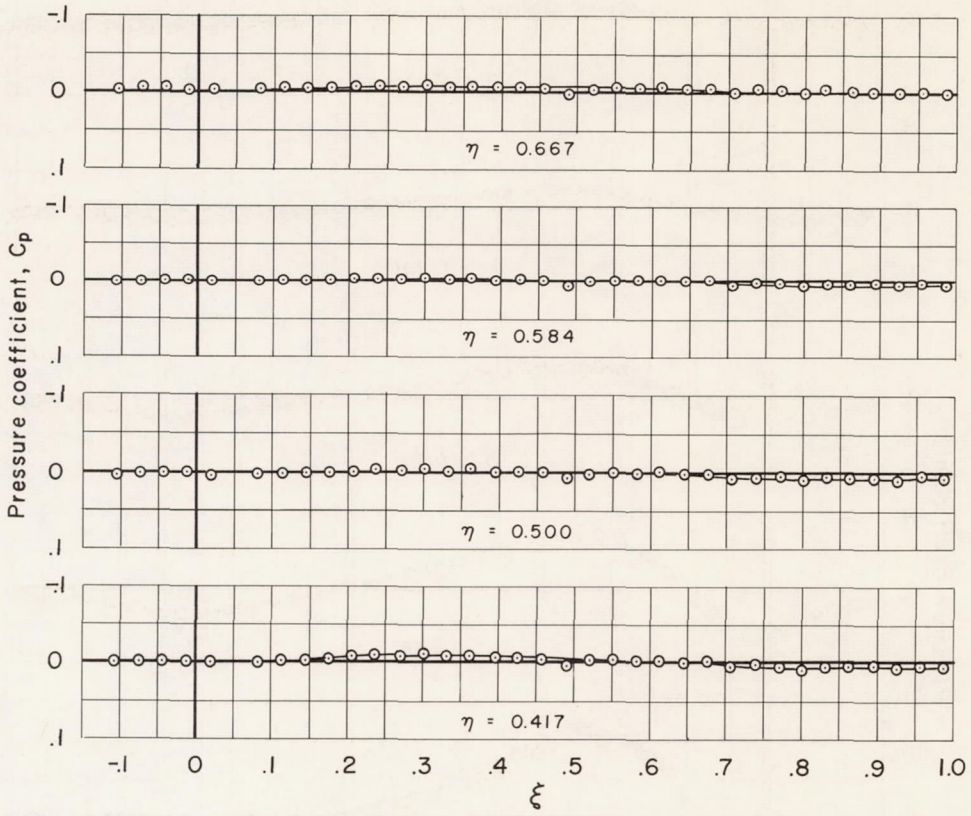

(a) $M_\infty = 0.80$, S_{max} at $\xi = 0.30$ - Concluded.

Figure 7.- Continued.

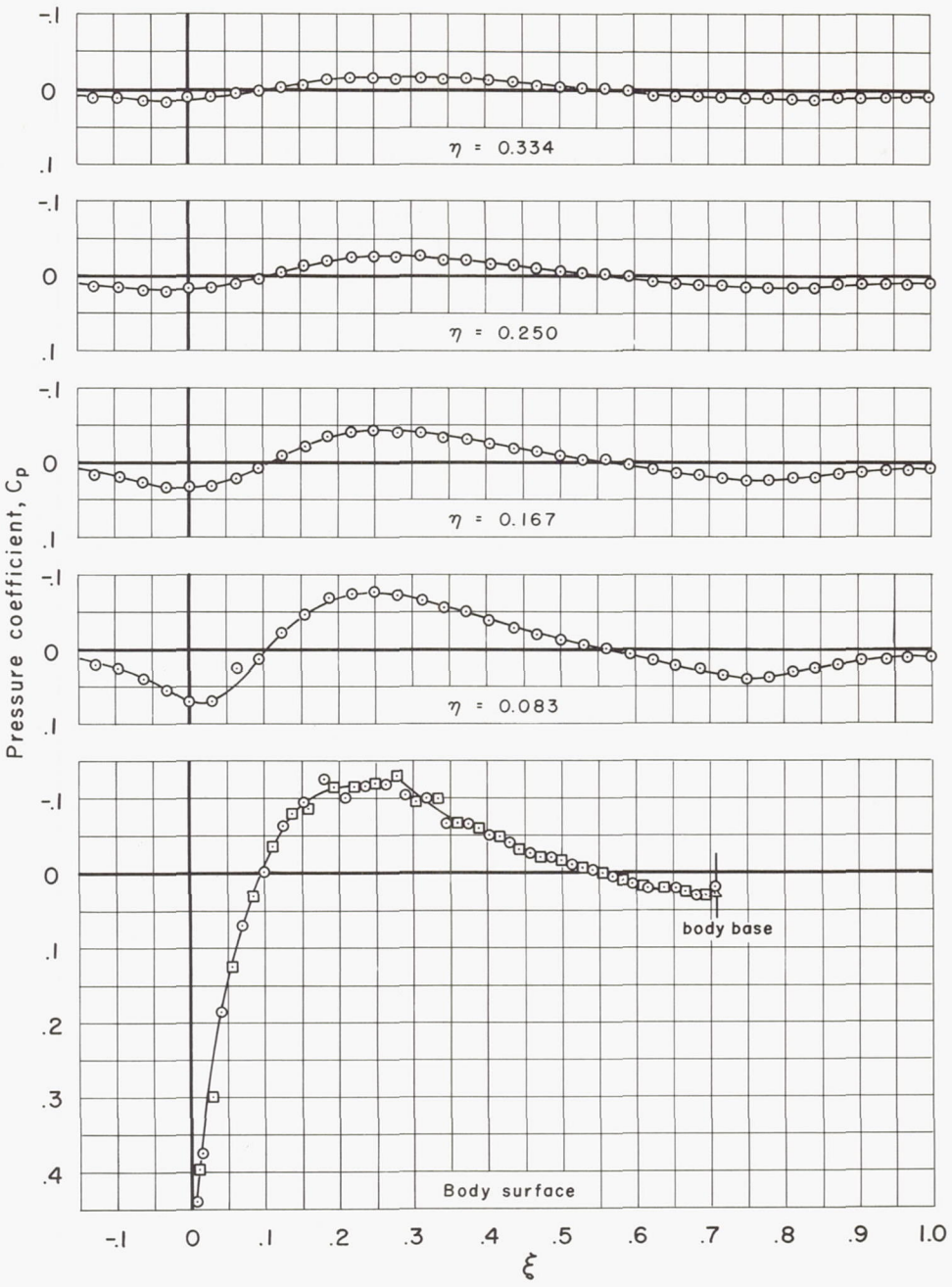

(b) $M_\infty = 0.90$, S_{max} at $\xi = 0.30$

Figure 7.- Continued.

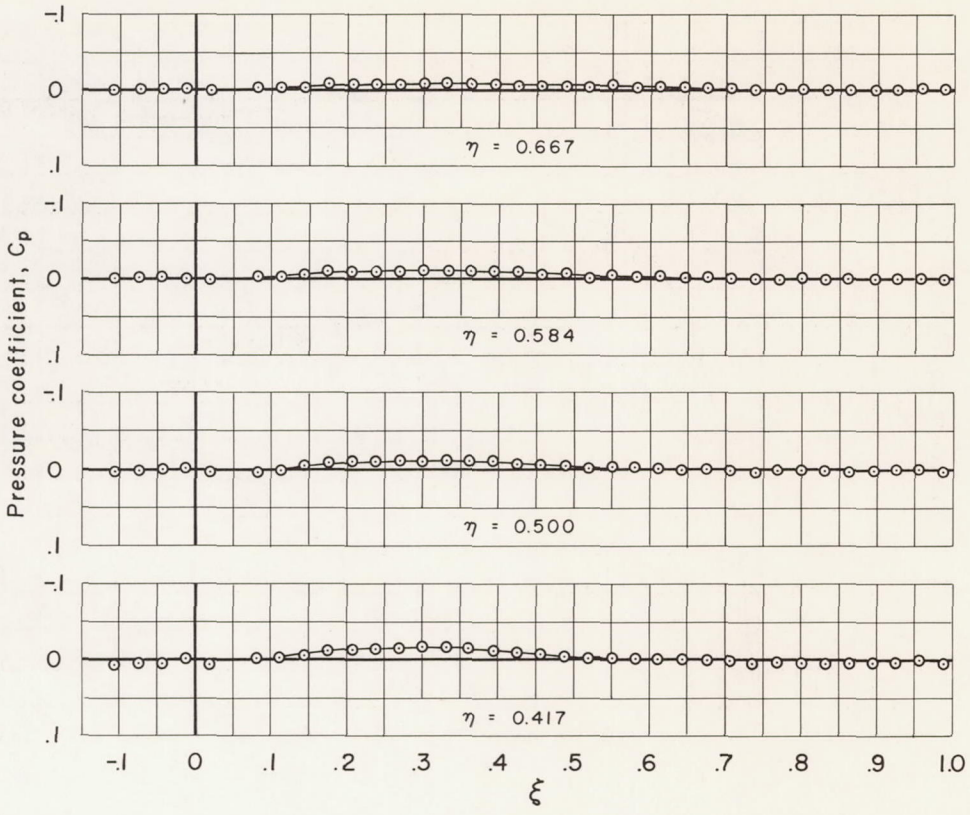

(b) $M_\infty = 0.90$, S_{max} at $\xi = 0.30$ - Concluded.

Figure 7.- Continued.

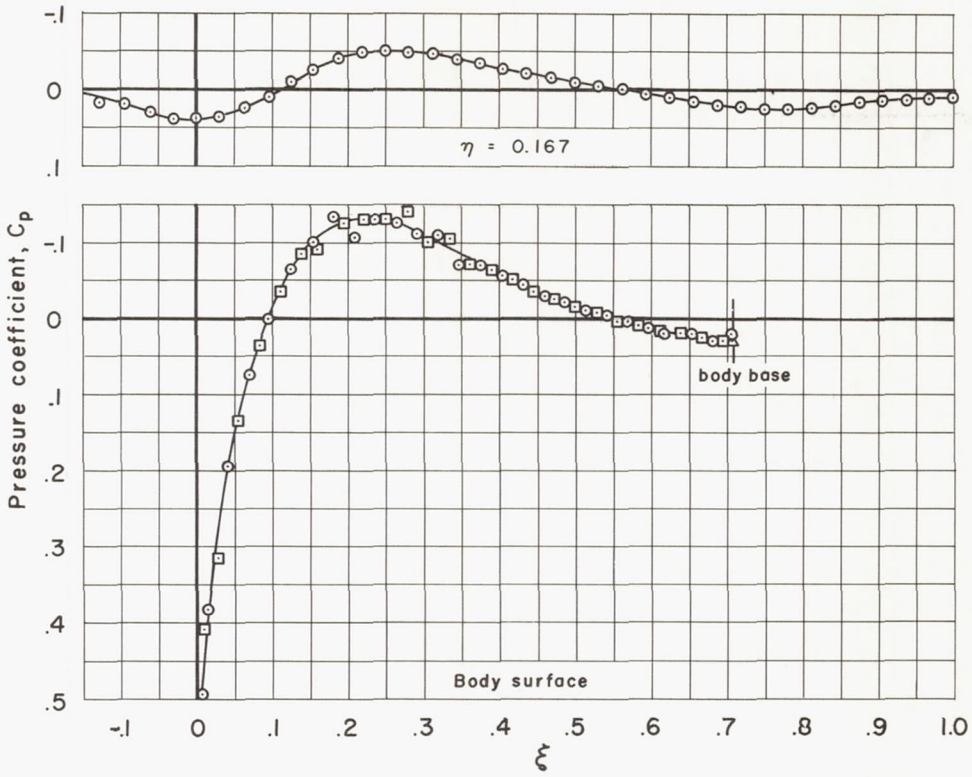

(c) $M_\infty = 0.925$, S_{max} at $\xi = 0.30$

Figure 7.- Continued.

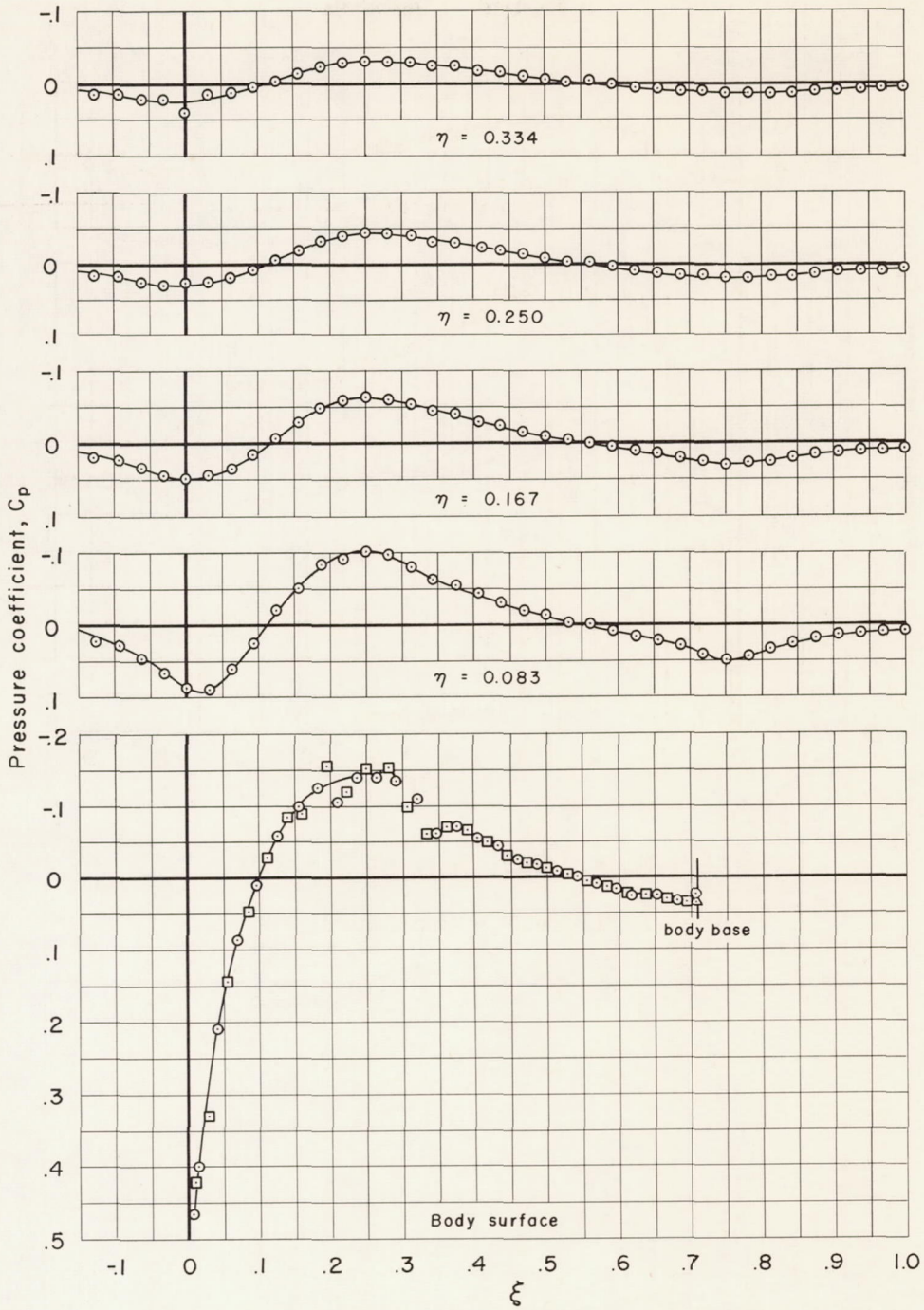

(d) $M_\infty = 0.95$, S_{max} at $\xi = 0.30$

Figure 7.- Continued.

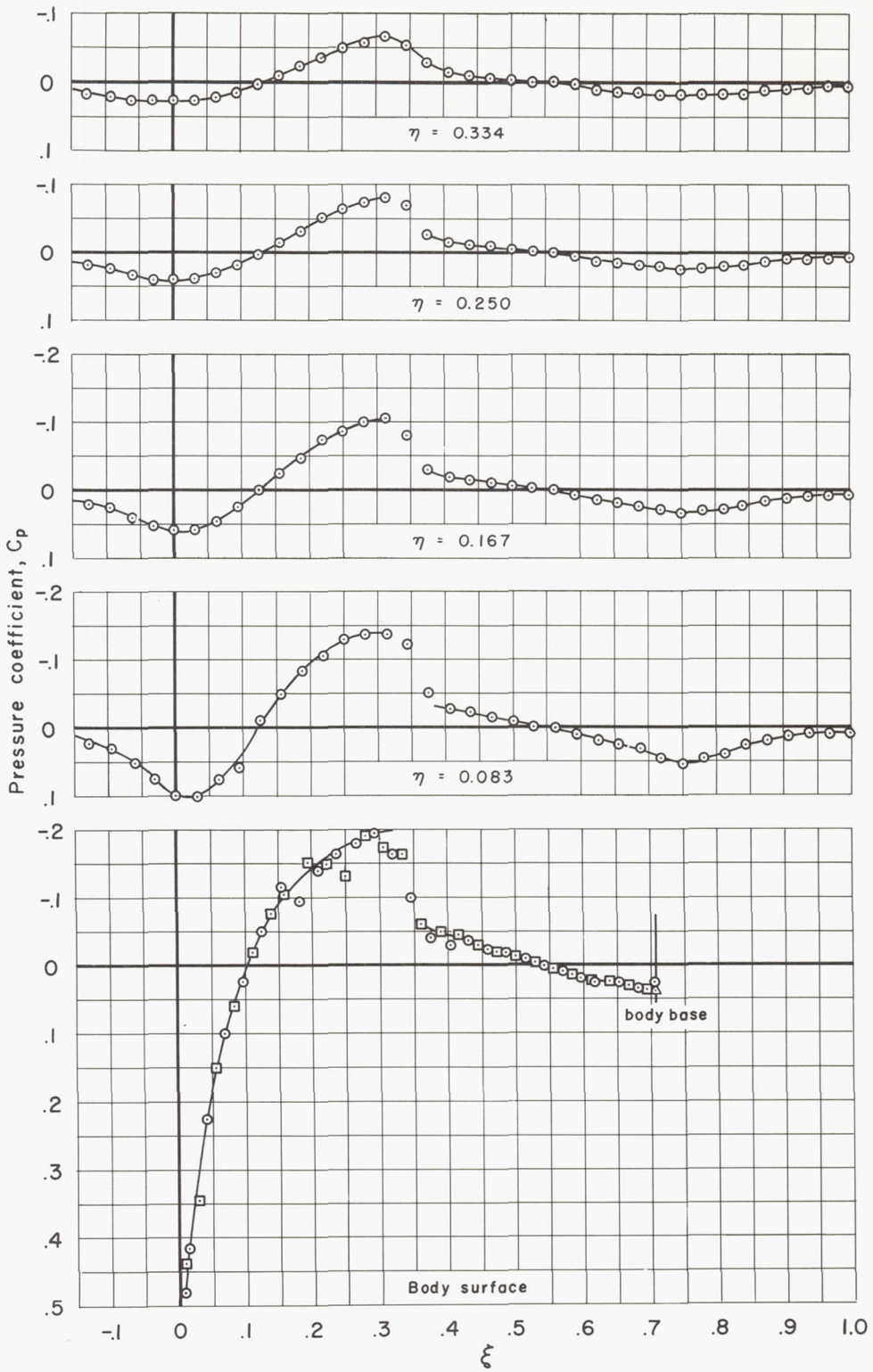

(e) $M_\infty = 0.975$, S_{max} at $\xi = 0.30$

Figure 7.- Continued.

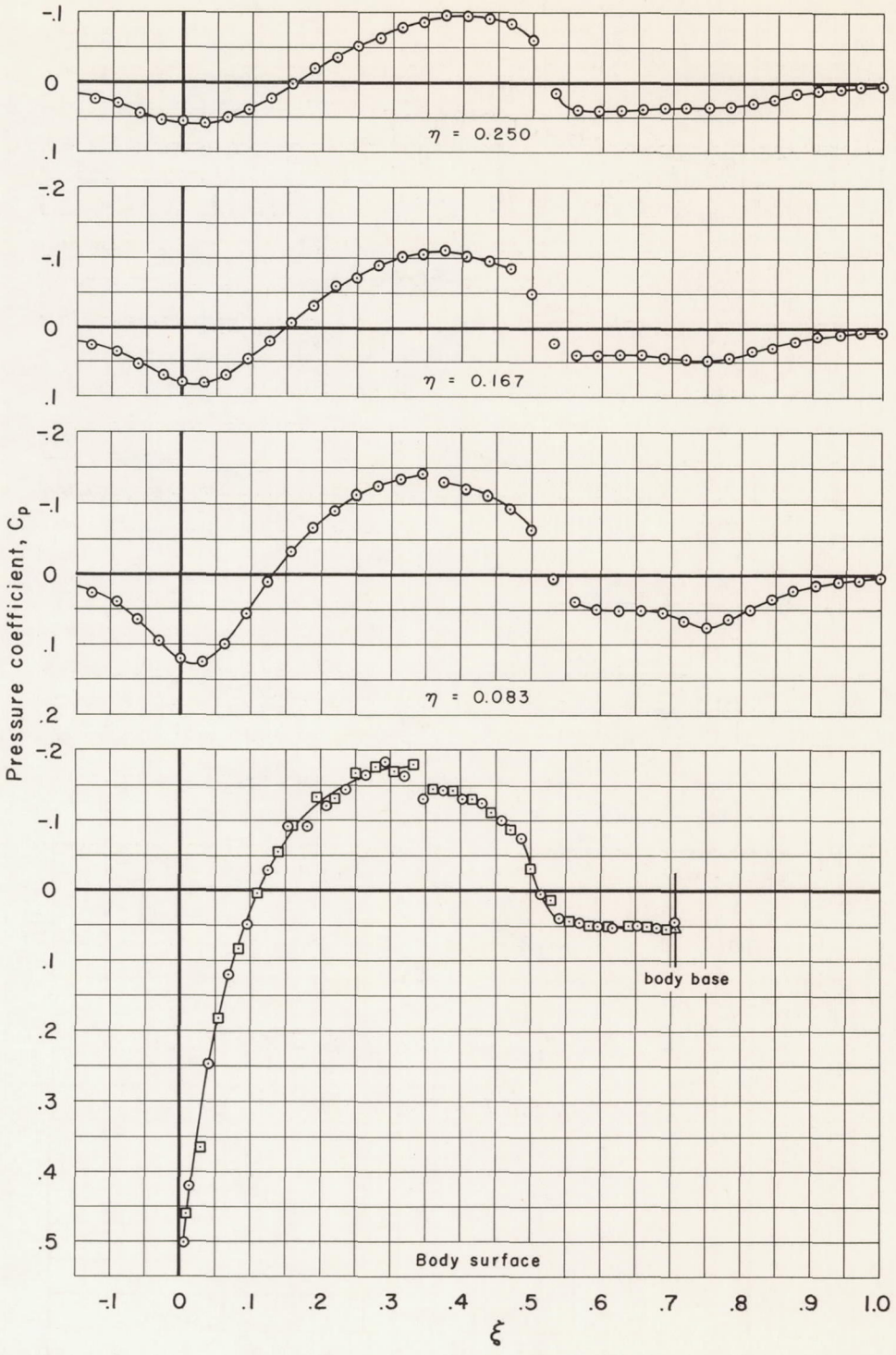

(f) M_∞ = 1.00, S_{max} at ξ = 0.30

Figure 7.- Continued.

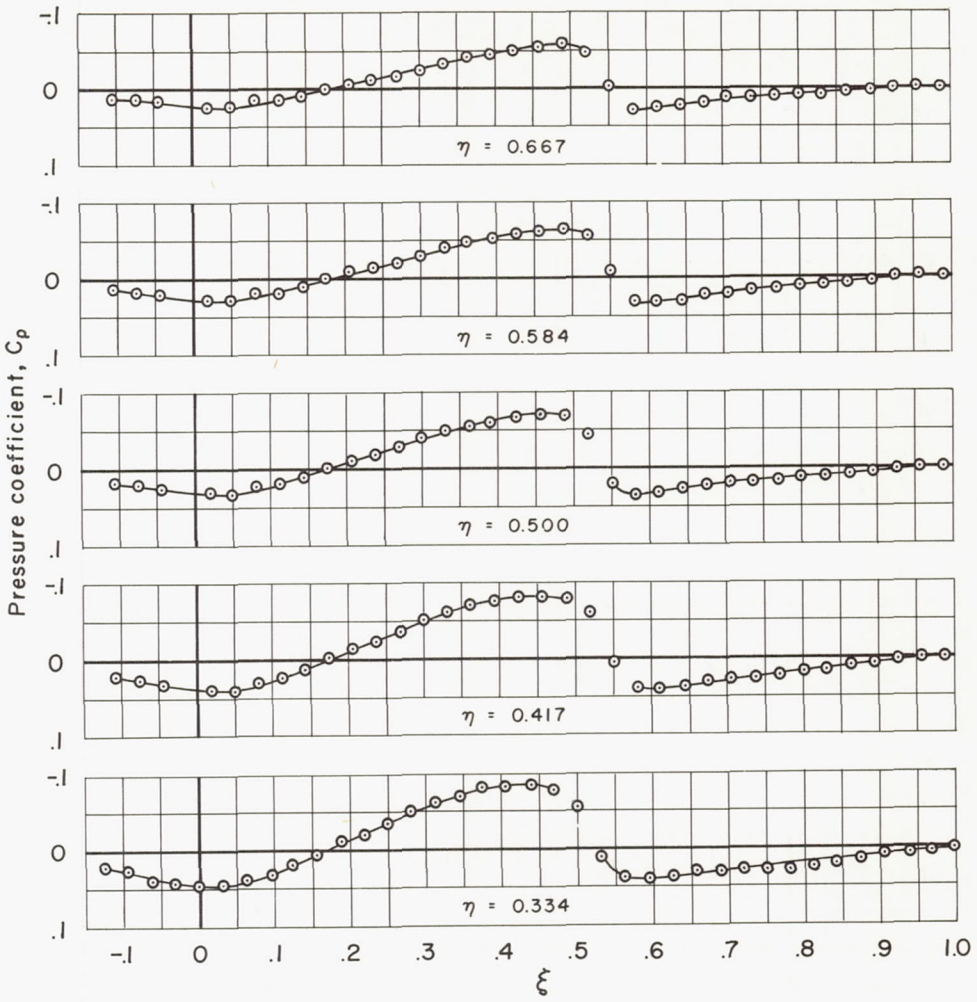

(f) M_∞ = 1.00, S_{max} at ξ = 0.30 - Concluded.

Figure 7.- Continued.

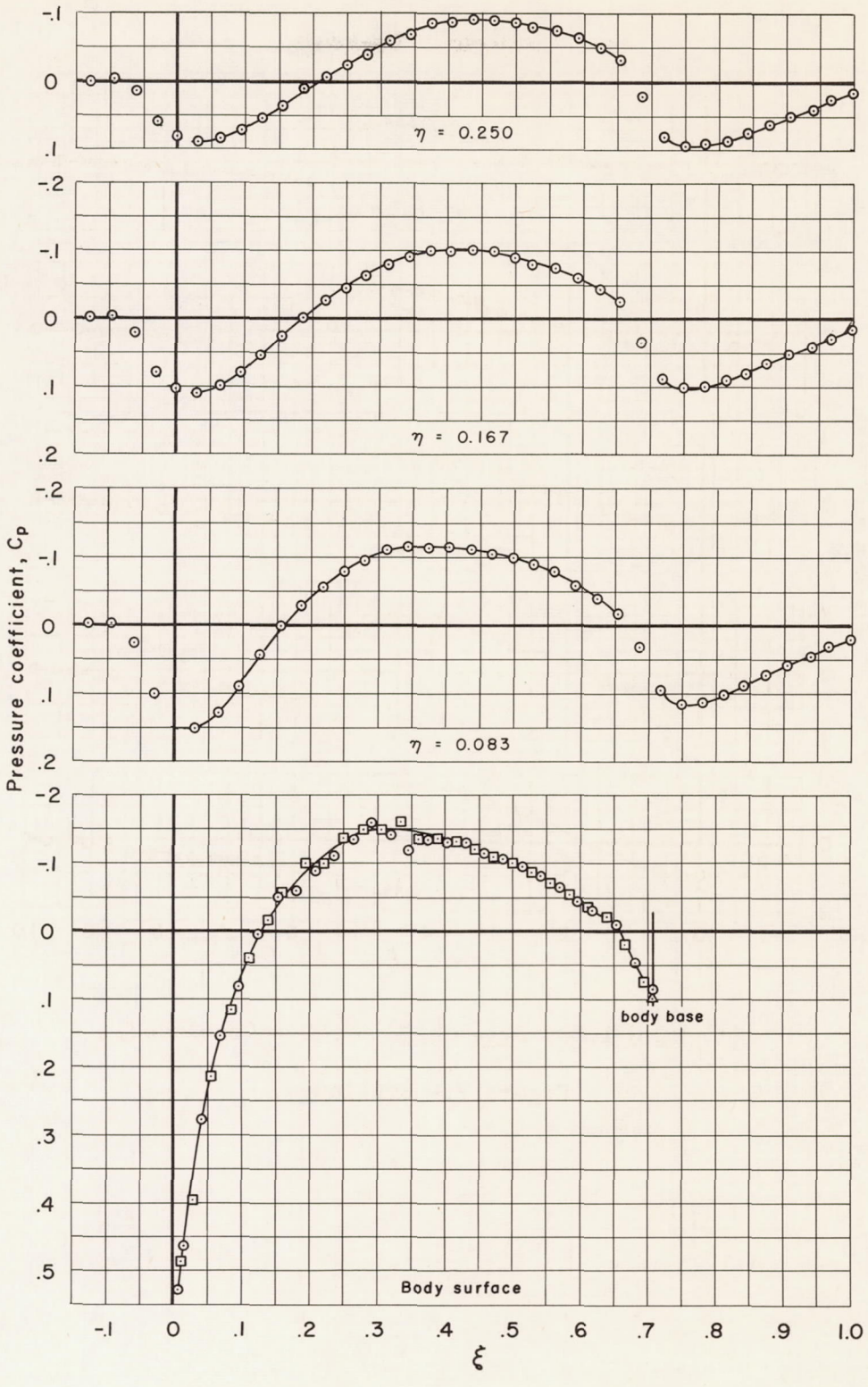

(g) M_∞ = 1.025, S_{max} at ξ = 0.30

Figure 7.- Continued.

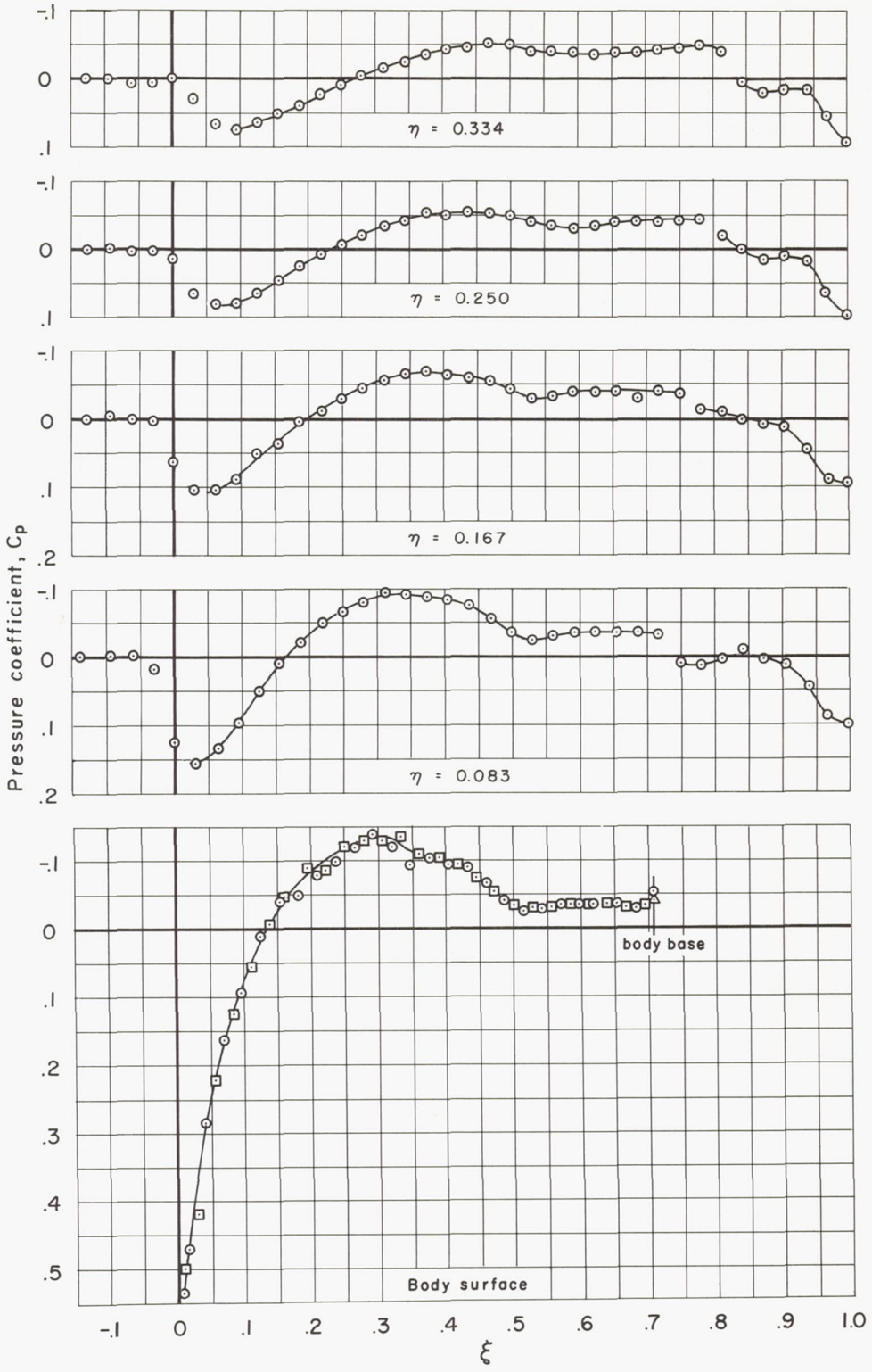

(h) M_∞ = 1.05, S_{max} at ξ = 0.30

Figure 7.- Continued.

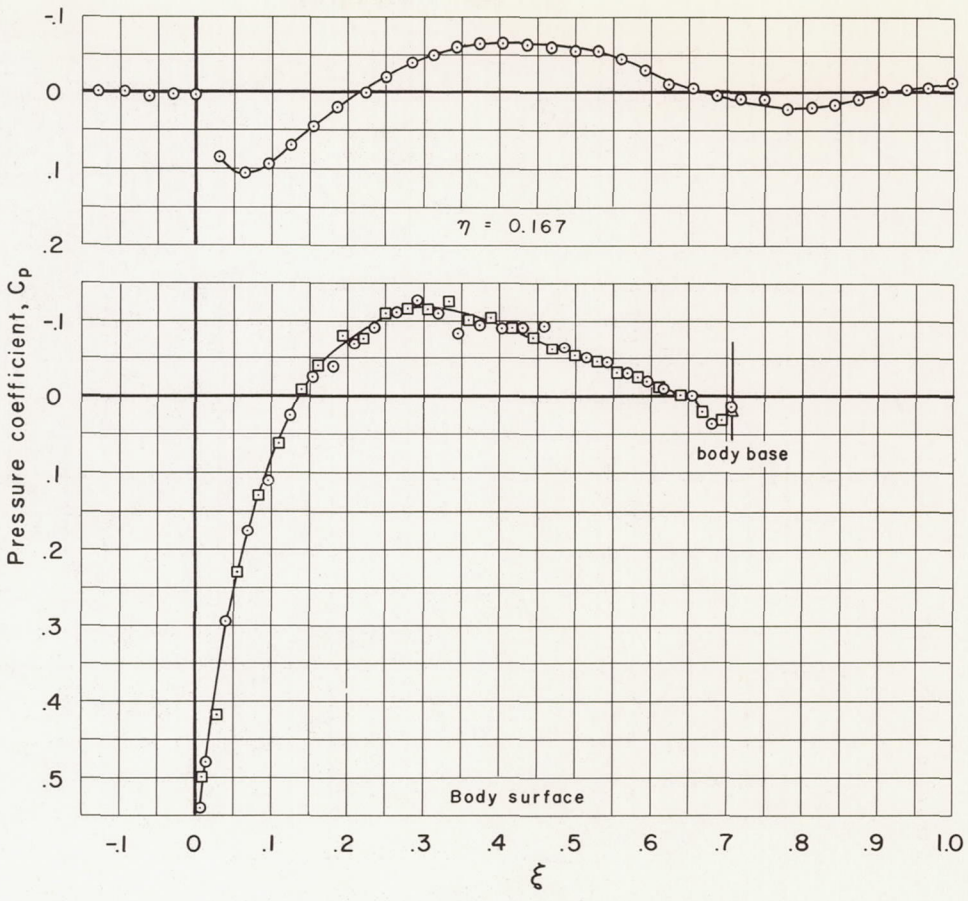

(i) $M_\infty = 1.075$, S_{max} at $\xi = 0.30$

Figure 7.- Continued.

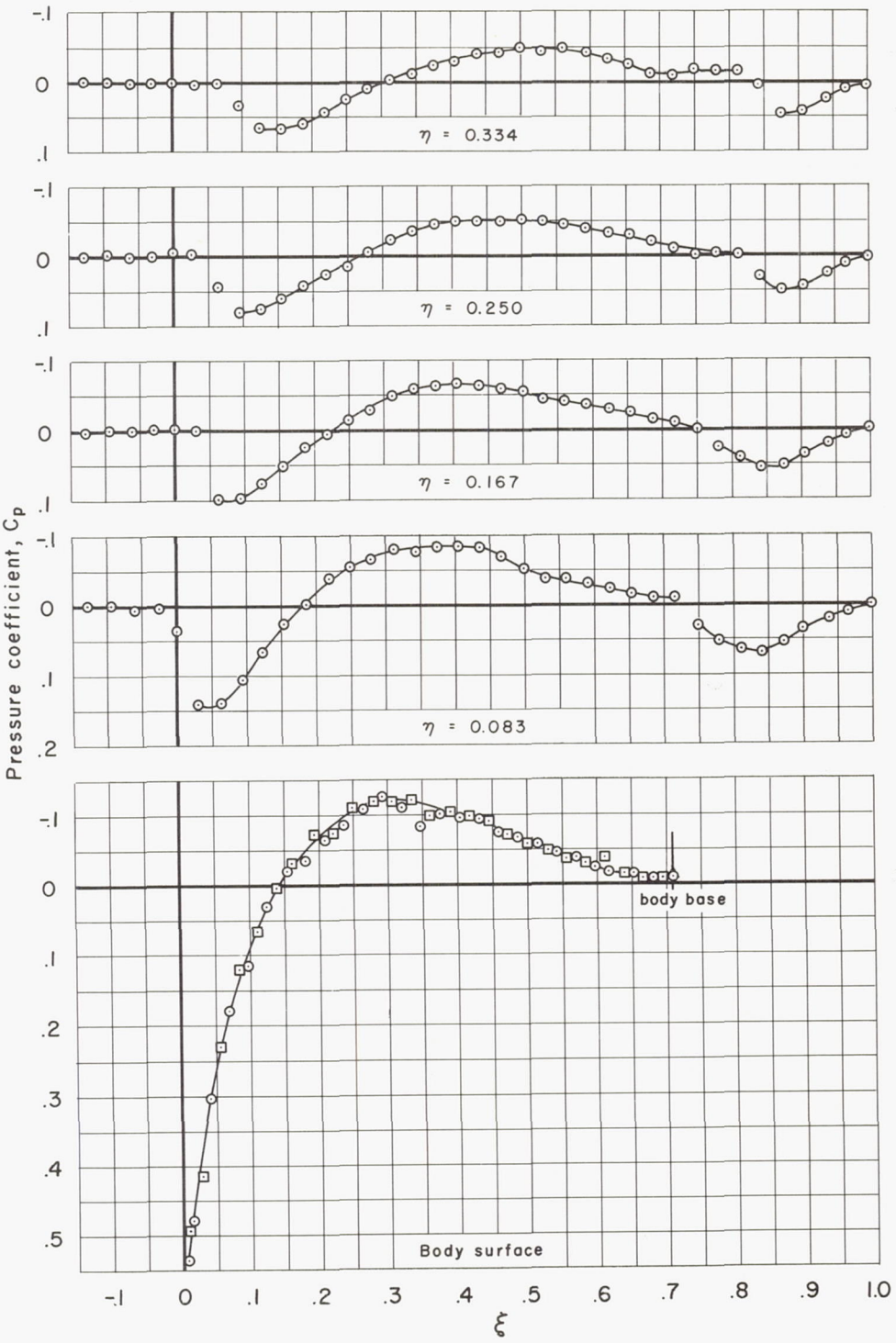

(j) M_∞ = 1.10, S_{max} at ξ = 0.30

Figure 7.- Continued.

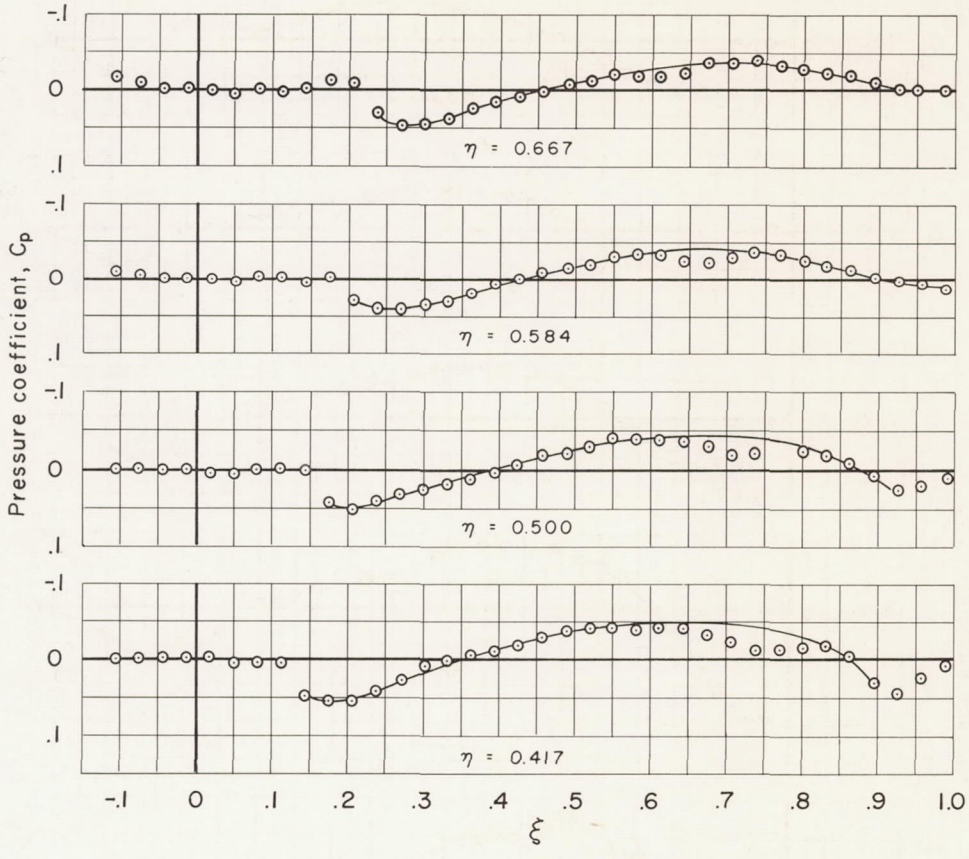

(j) M_∞ = 1.10, S_{max} at ξ = 0.30 - Concluded.

Figure 7.- Continued.

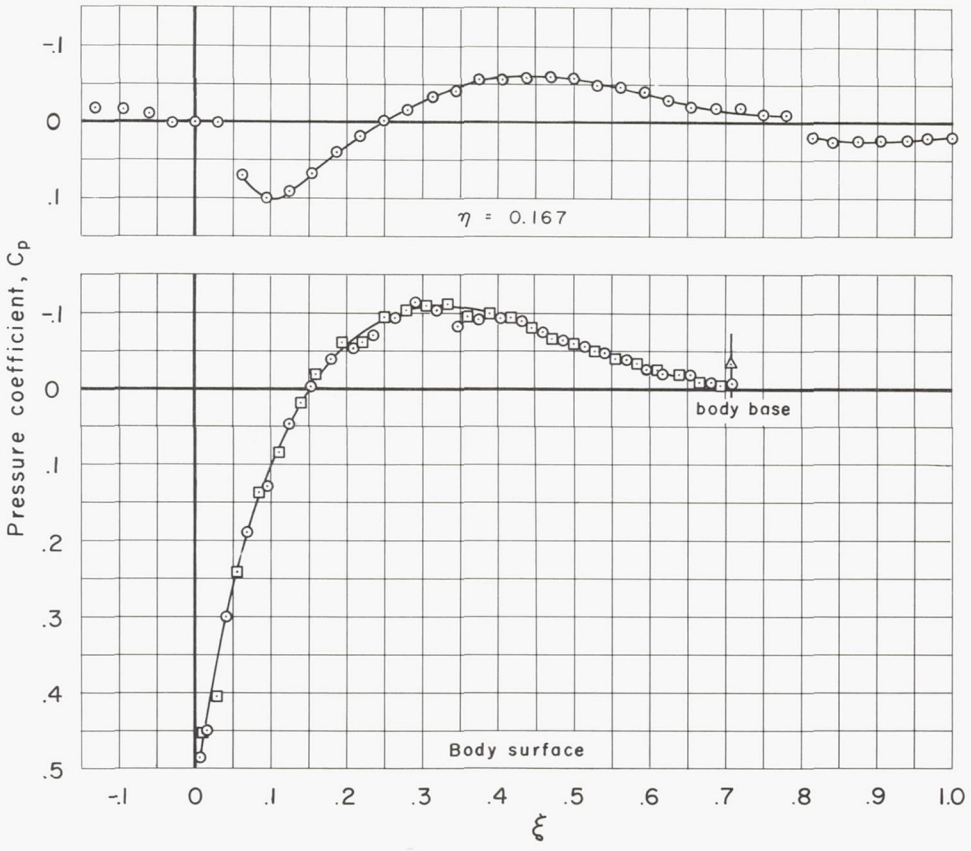

(k) $M_\infty = 1.15$, S_{max} at $\xi = 0.30$

Figure 7.- Continued.

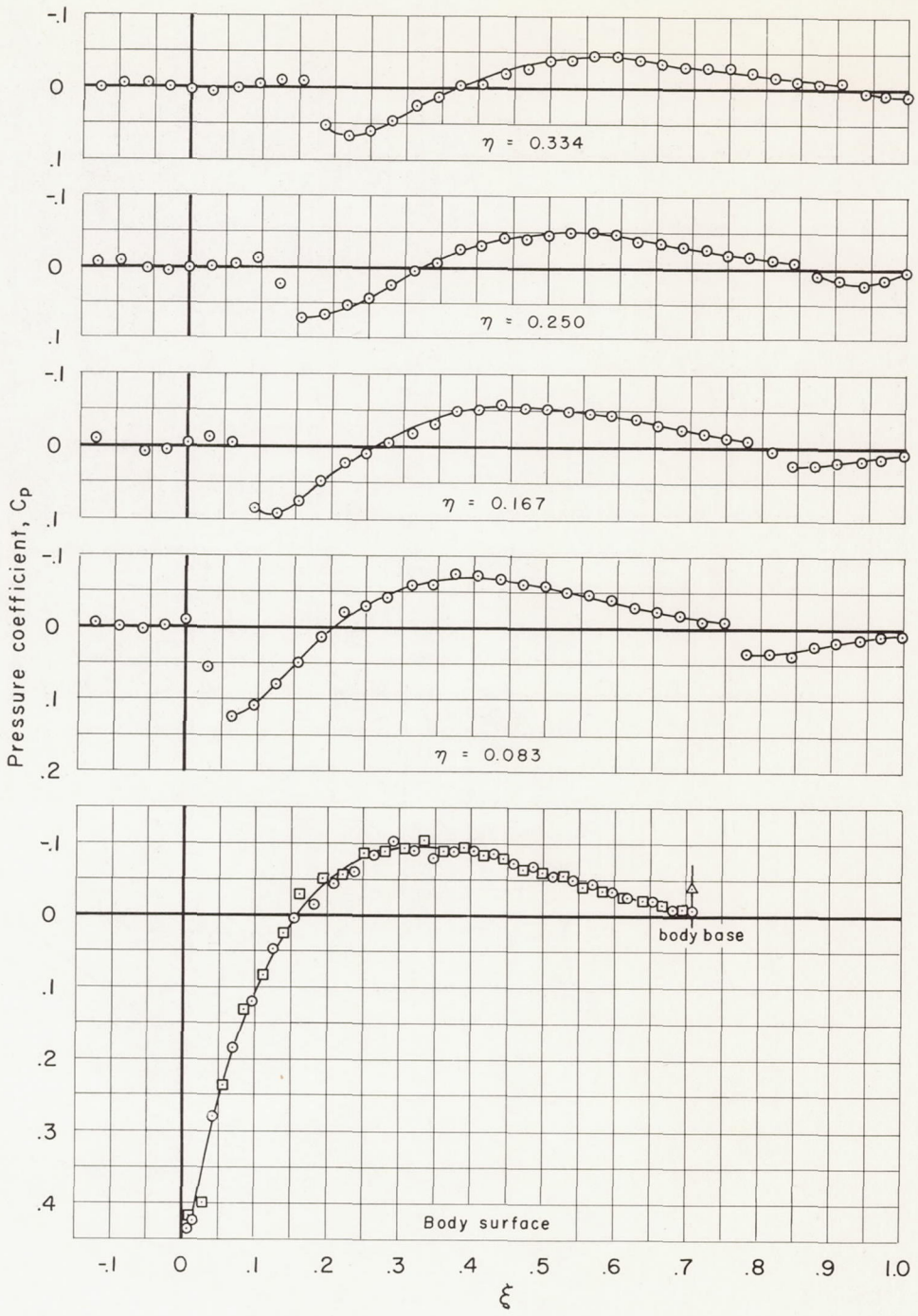

(l) M_∞ = 1.20, S_{max} at ξ = 0.30

Figure 7.- Continued.

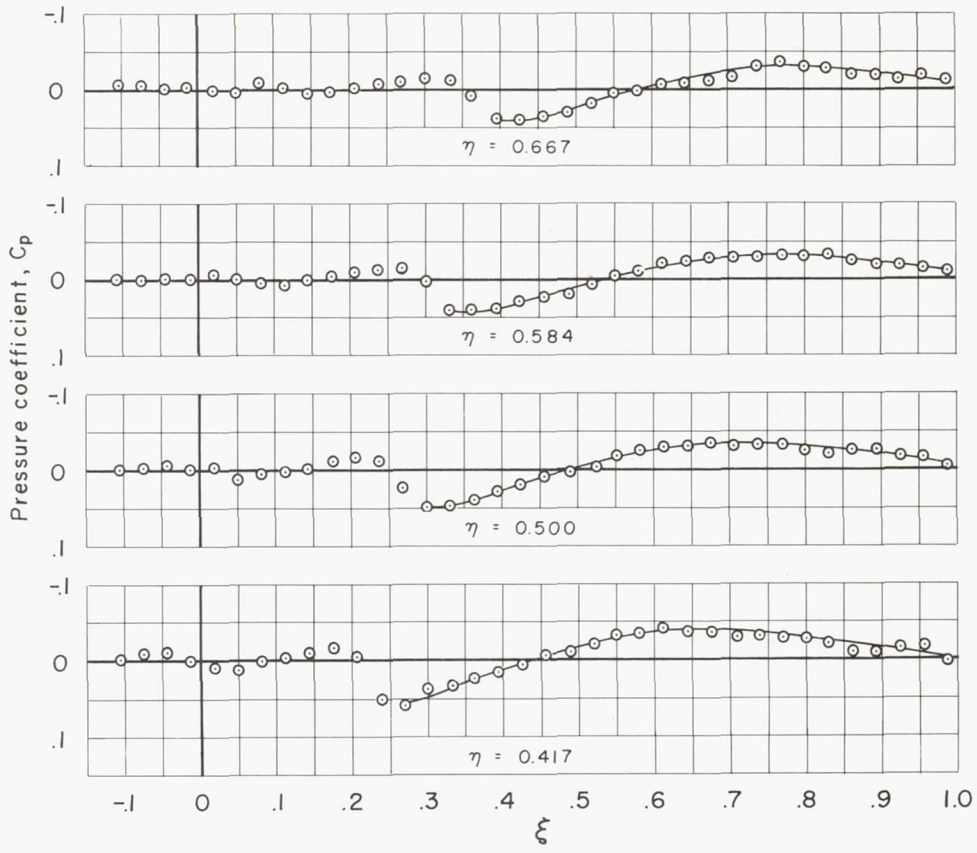

(l) M_∞ = 1.20, S_{max} at ξ = 0.30 - Concluded.

Figure 7.- Concluded.

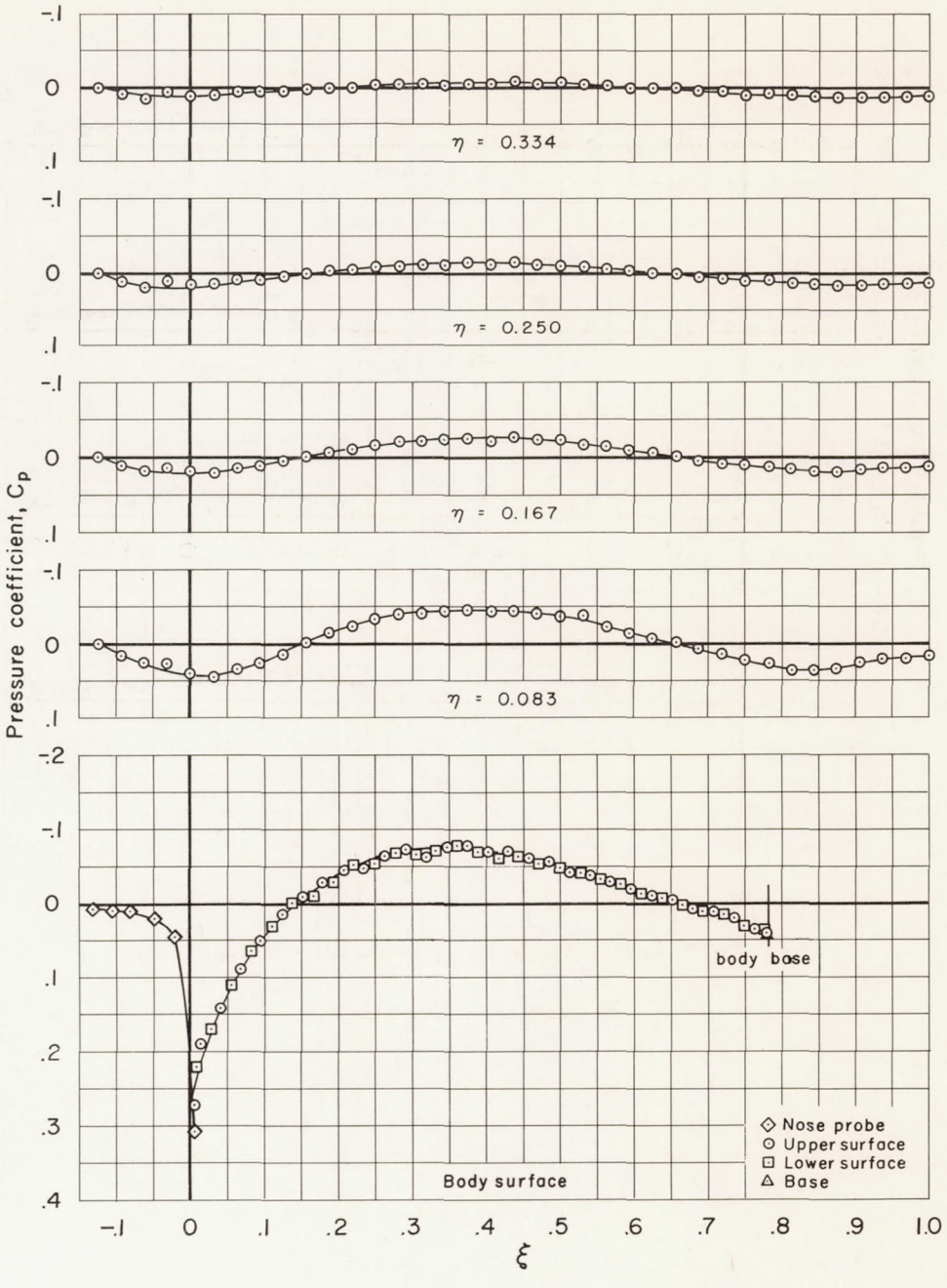

(a) $M_\infty = 0.80$, S_{max} at $\xi = 0.40$

Figure 8.- Experimental pressure distributions for the body with maximum cross-sectional area located at $\xi = 0.40$.

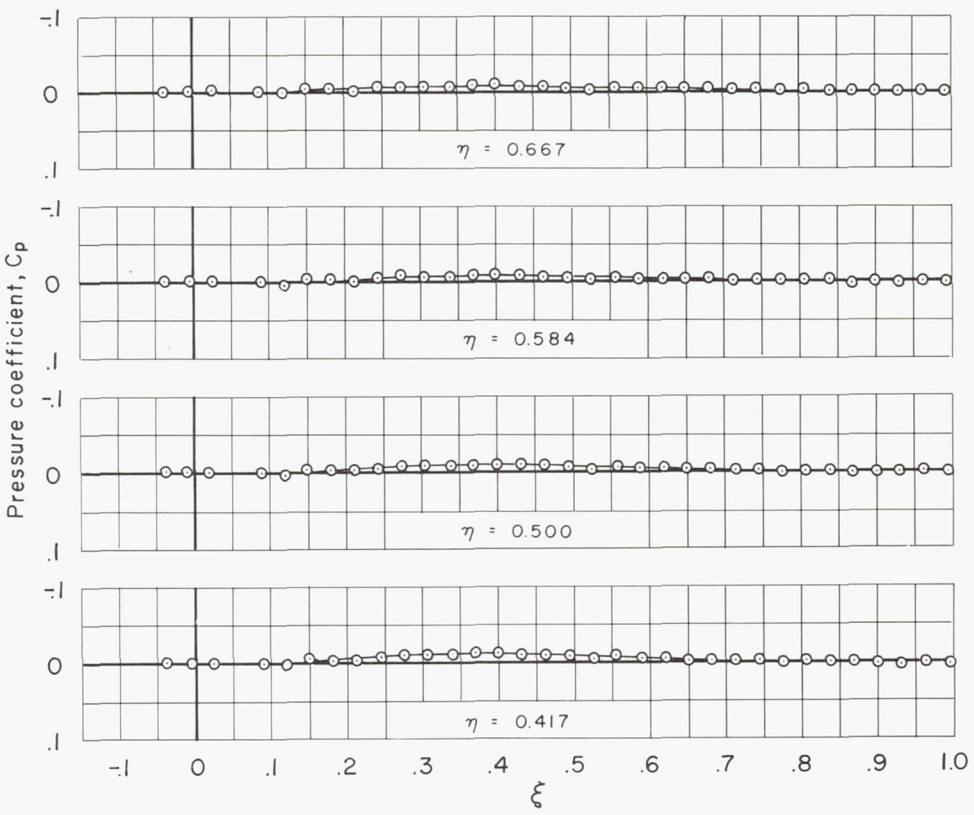

(a) $M_\infty = 0.80$, S_{max} at $\xi = 0.40$ - Concluded.

Figure 8.- Continued.

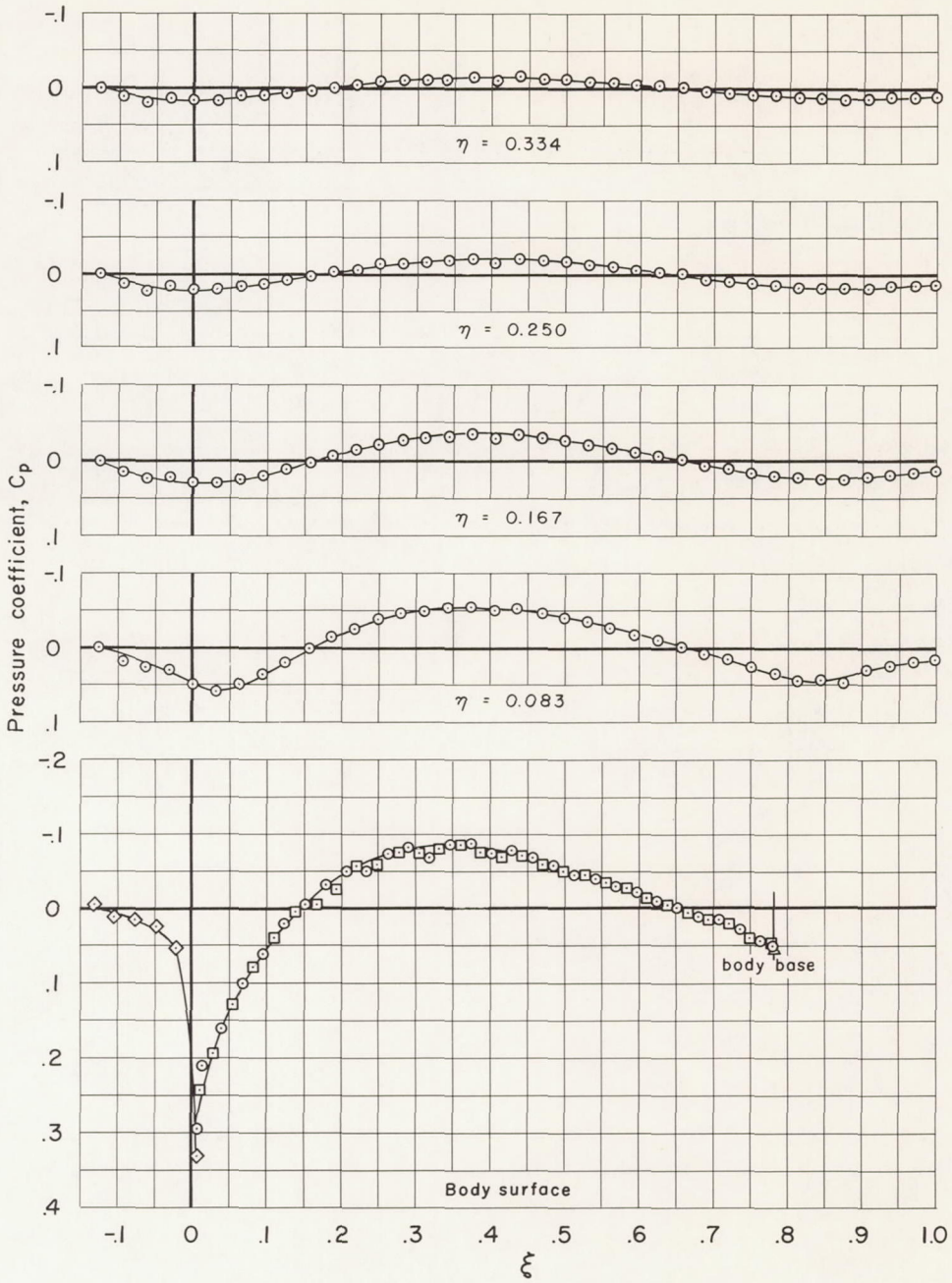

(b) $M_\infty = 0.90$, S_{max} at $\xi = 0.40$

Figure 8.- Continued.

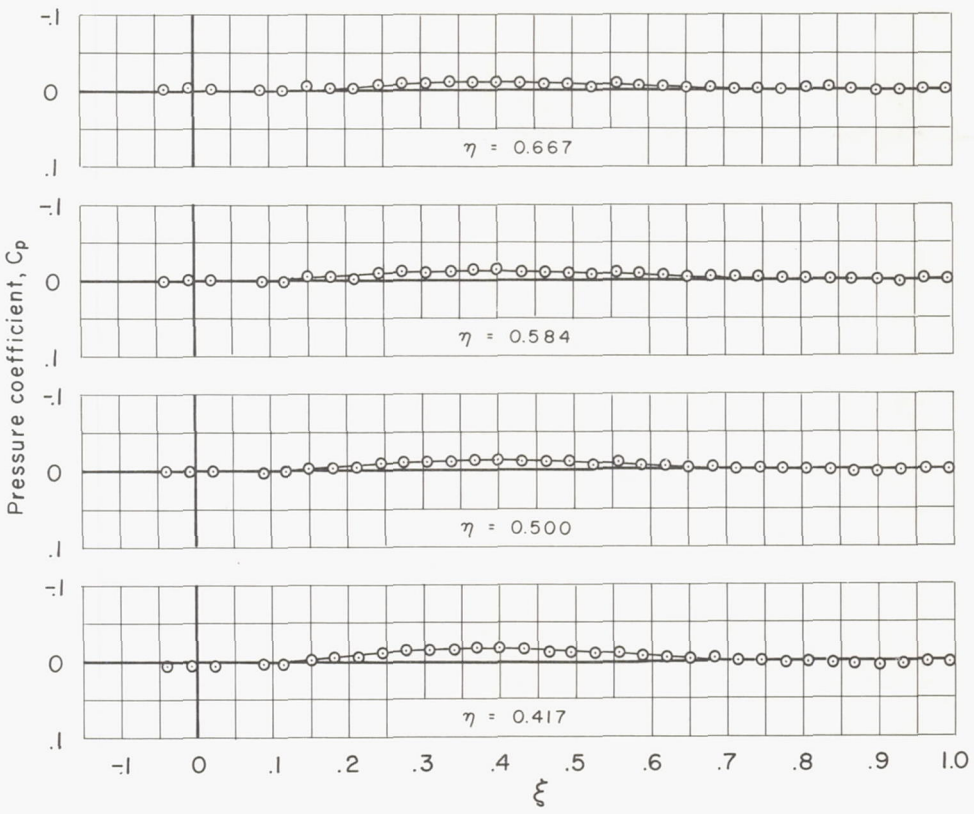

(b) M_∞ = 0.90, S_{max} at ξ = 0.40 - Concluded.

Figure 8.- Continued.

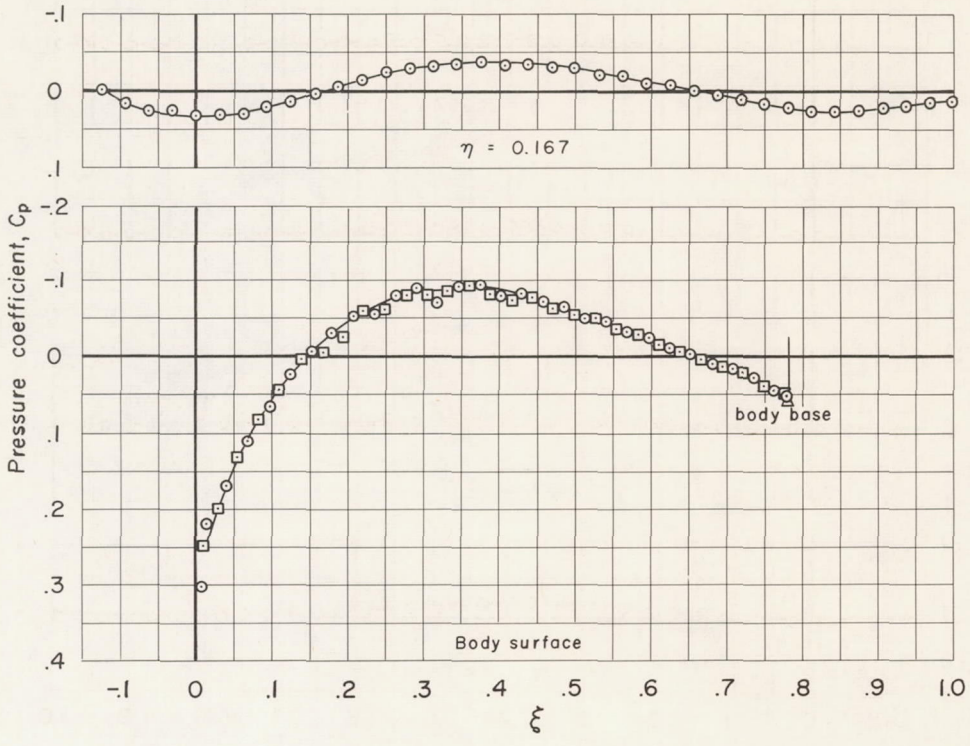

(c) $M_\infty = 0.925$, S_{max} at $\xi = 0.40$

Figure 8.- Continued.

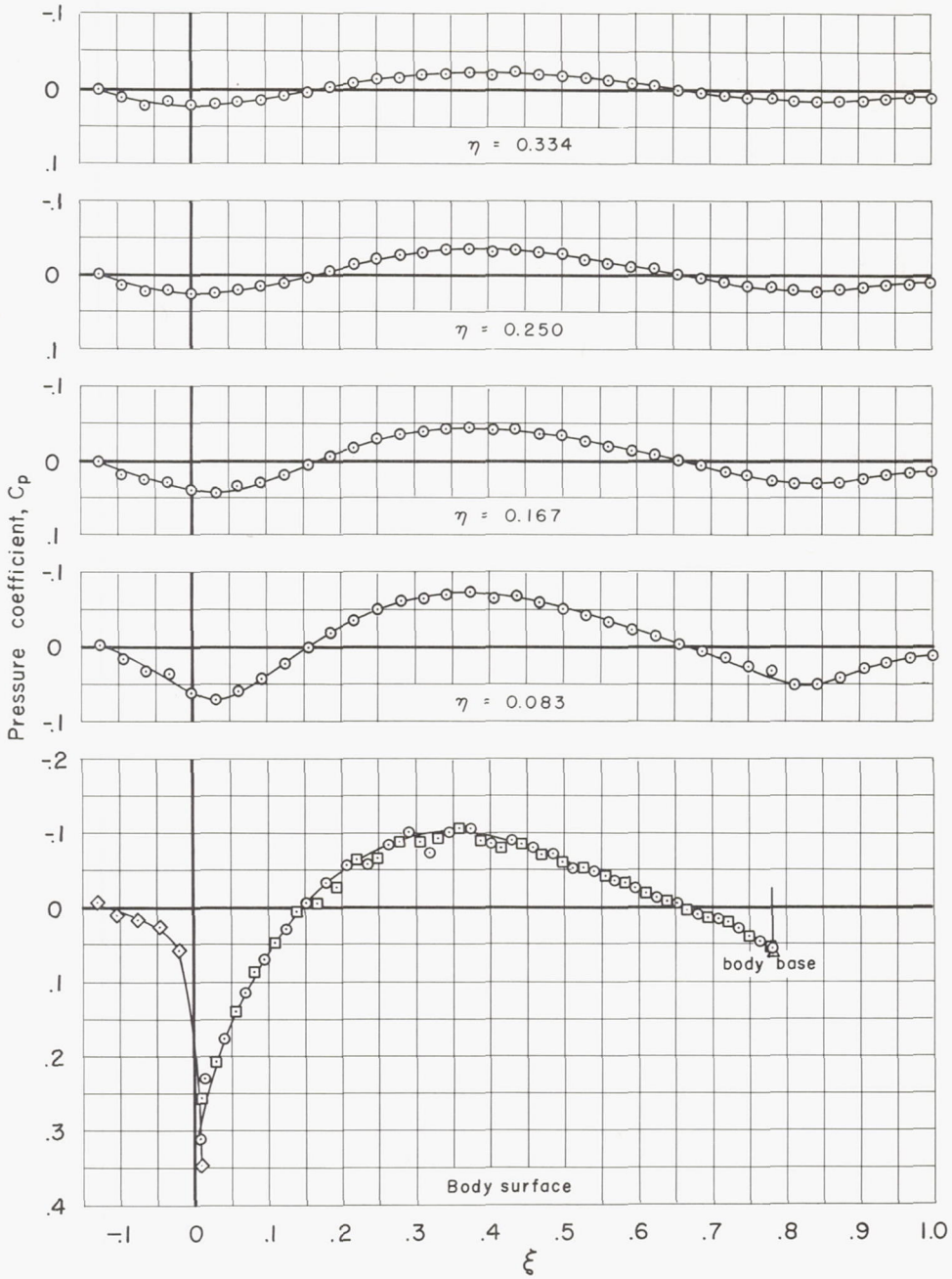

(d) $M_\infty = 0.95$, S_{max} at $\xi = 0.40$

Figure 8.- Continued.

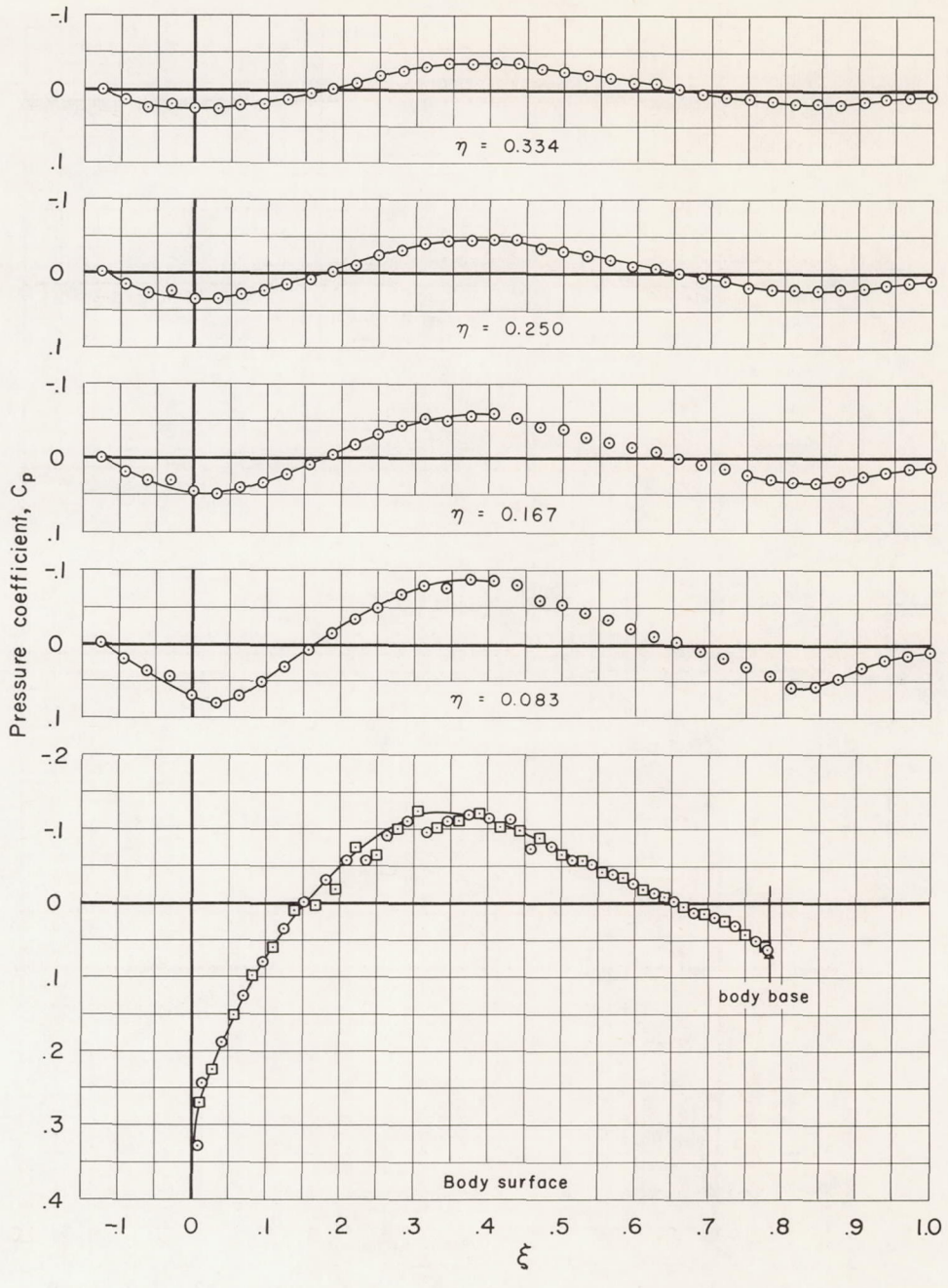

(e) $M_\infty = 0.975$, S_{max} at $\xi = 0.40$

Figure 8.- Continued.

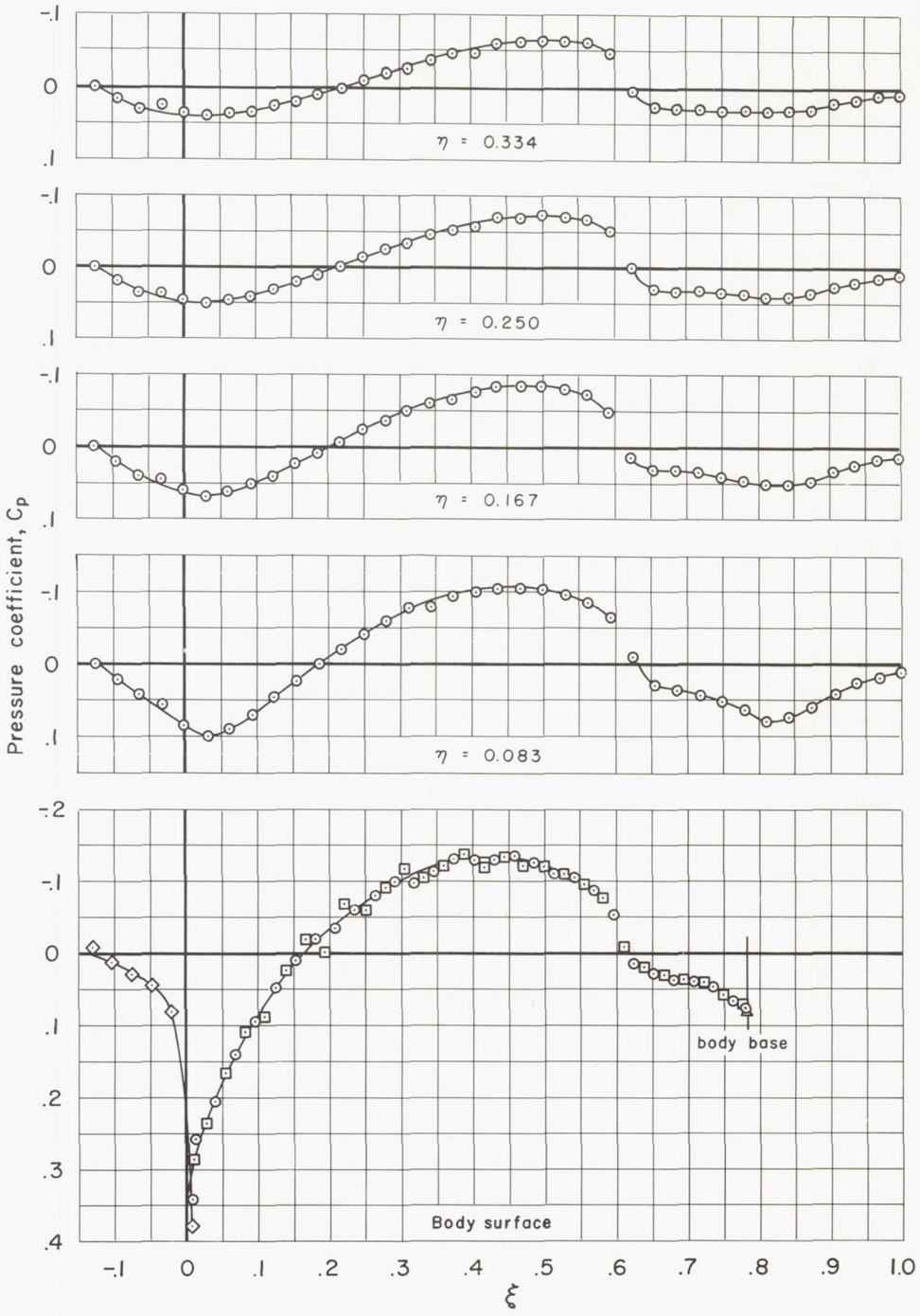

(f) M_∞ = 1.00, S_{max} at ξ = 0.40

Figure 8.- Continued.

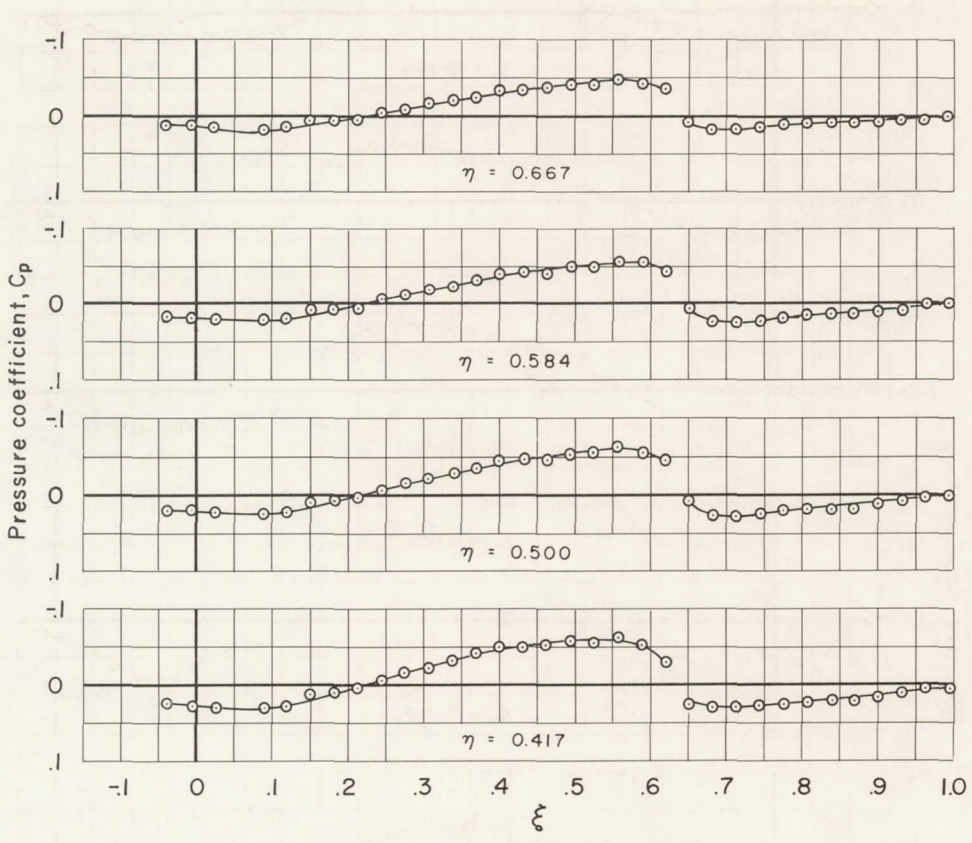

(f) M_∞ = 1.00, S_{max} at ξ = 0.40 - Concluded.

Figure 8.- Continued.

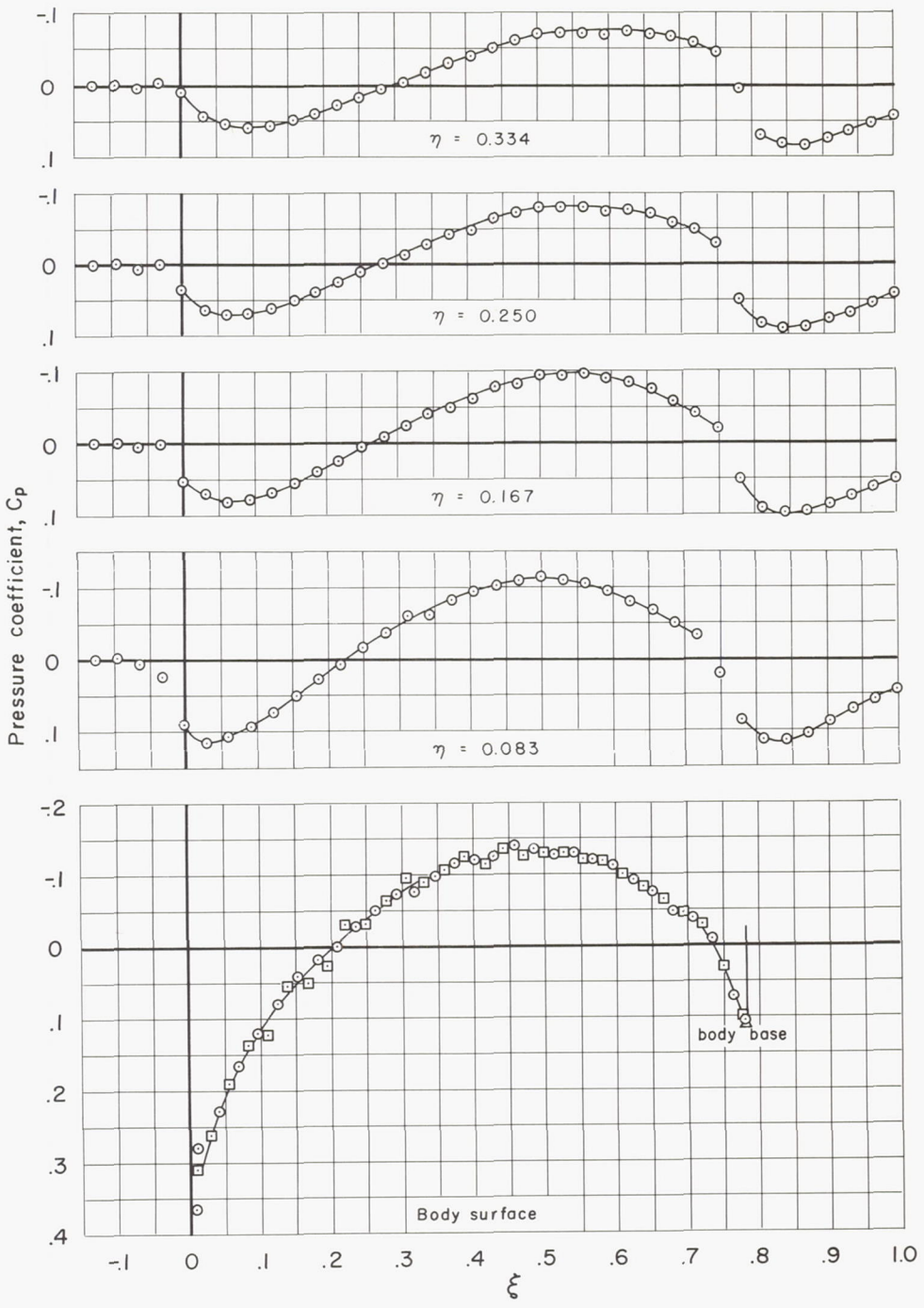

(g) M_∞ = 1.025, S_{max} at ξ = 0.40

Figure 8.- Continued.

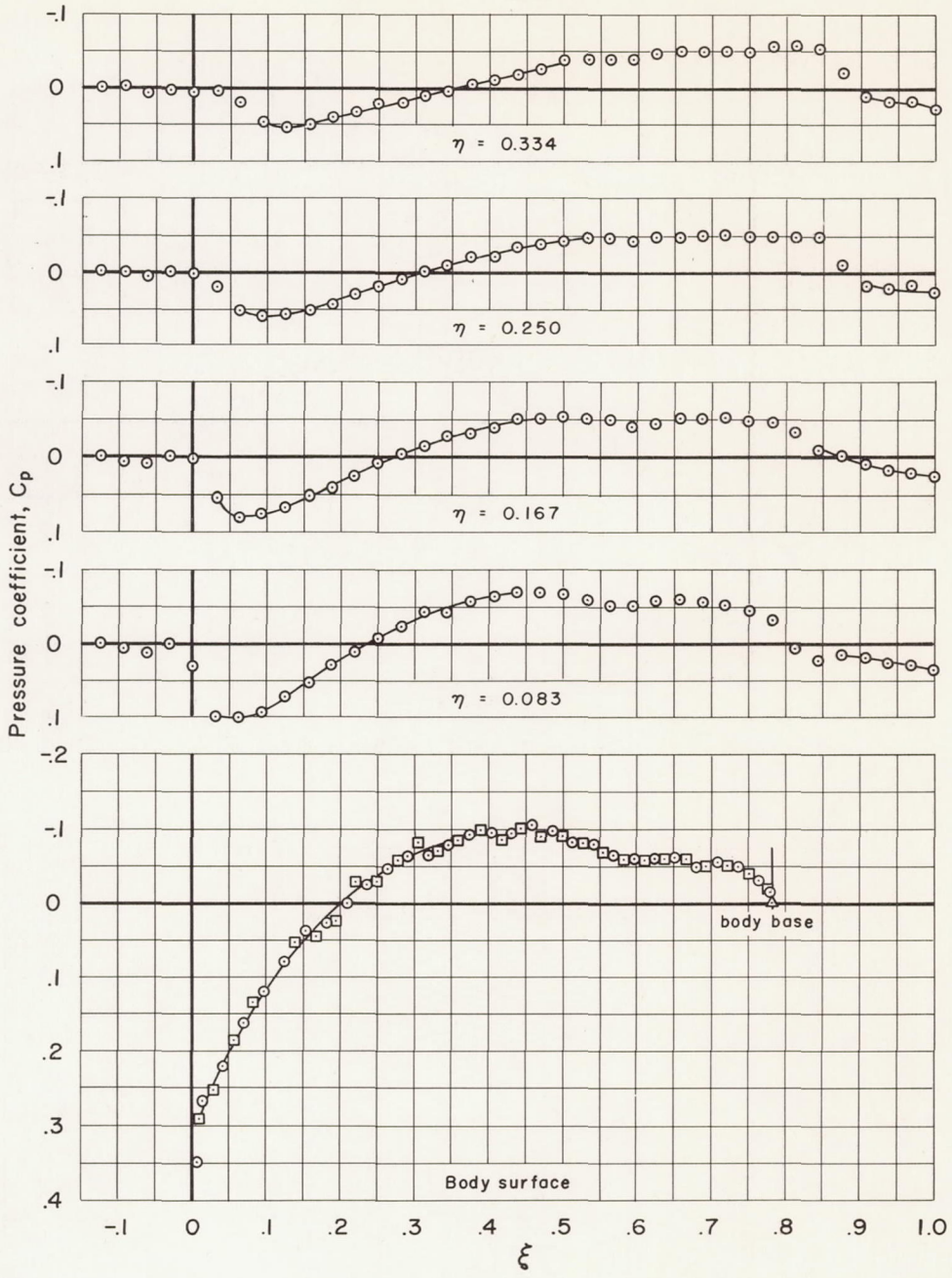

(h) M_∞ = 1.05, S_{max} at ξ = 0.40

Figure 8.- Continued.

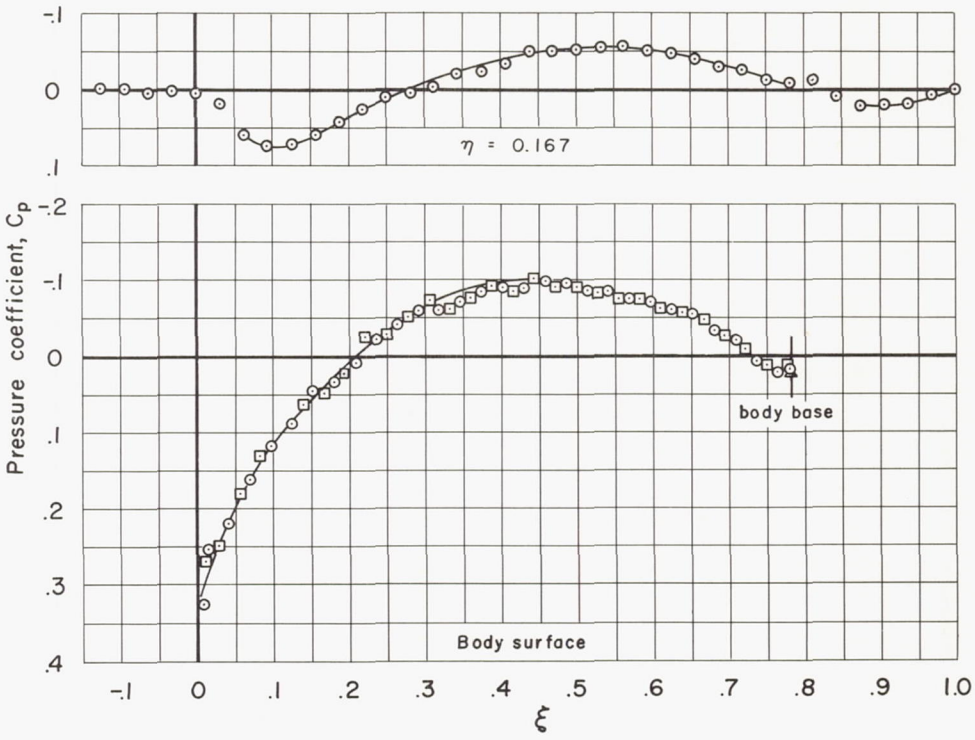

(i) $M_\infty = 1.075$, S_{max} at $\xi = 0.40$

Figure 8.- Continued.

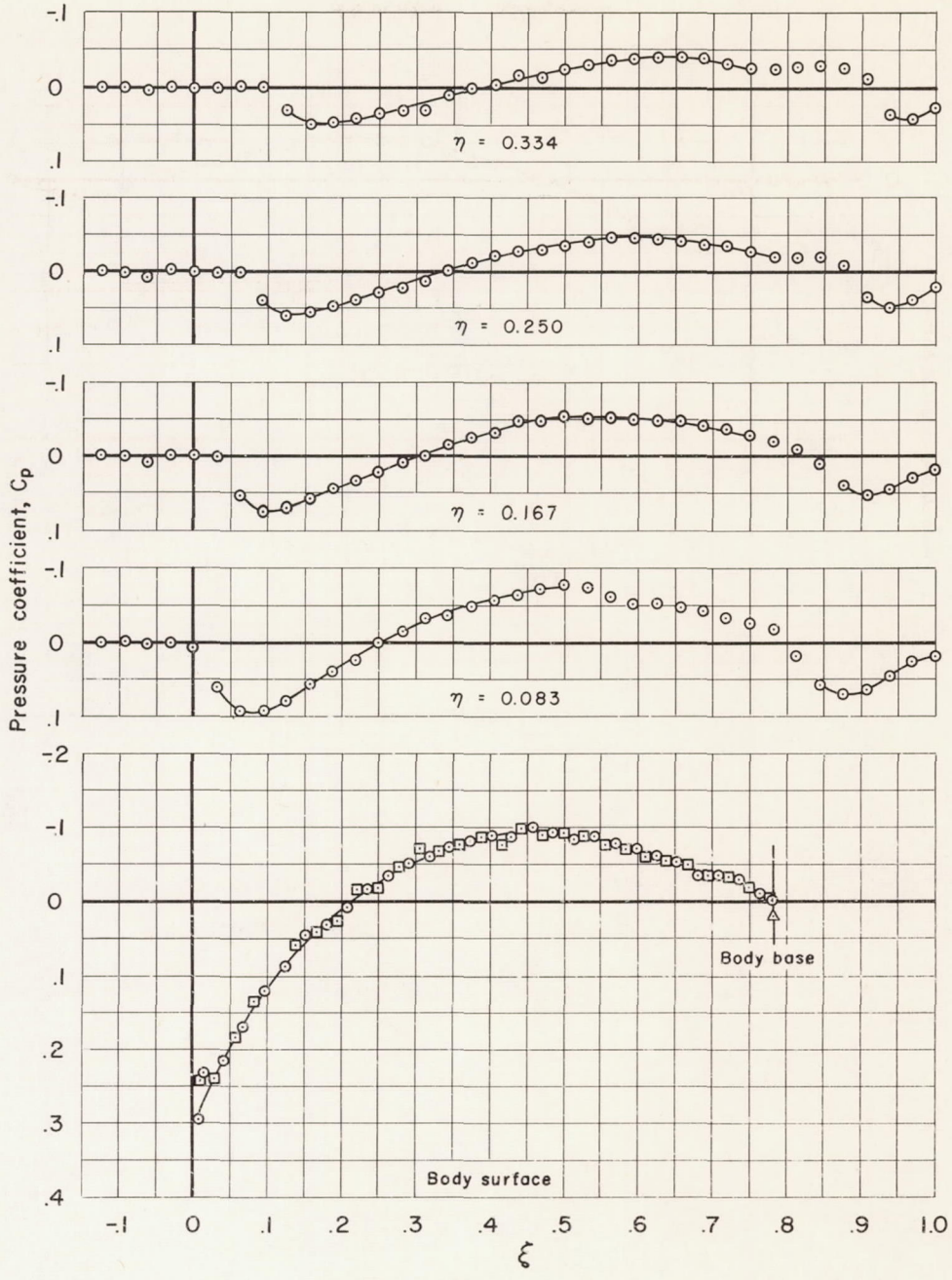

(j) M_∞ = 1.10, S_{max} at ξ = 0.40

Figure 8.- Continued.

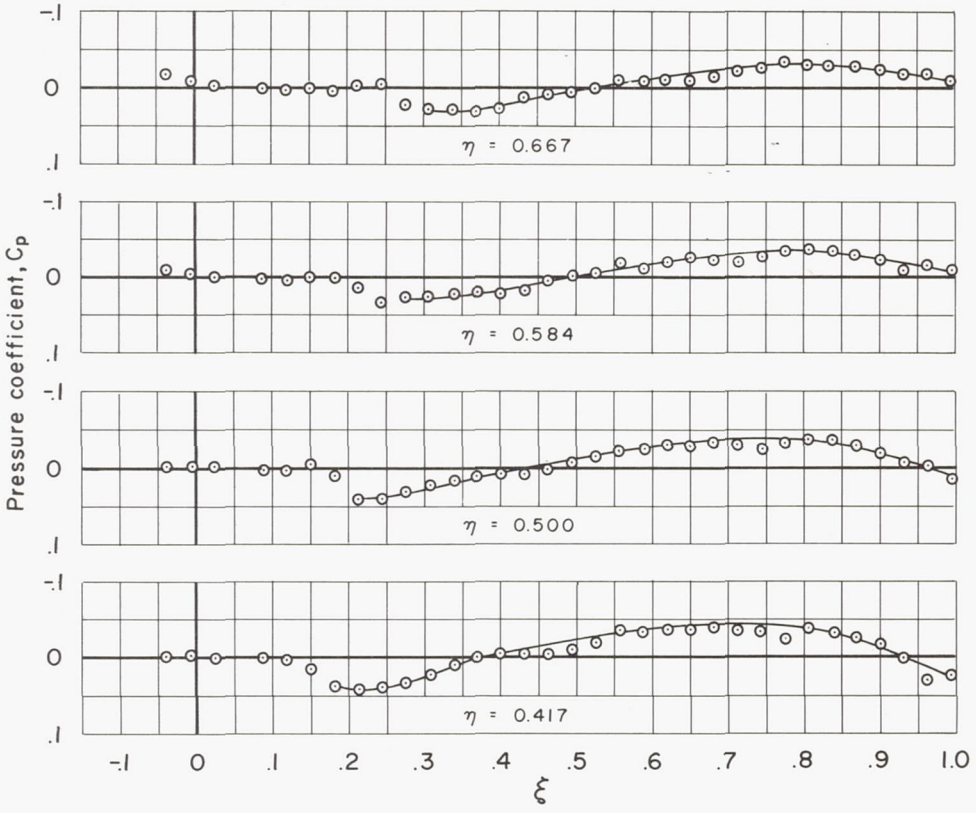

(j) M_∞ = 1.10, S_{max} at ξ = 0.40 - Concluded.

Figure 8.- Continued.

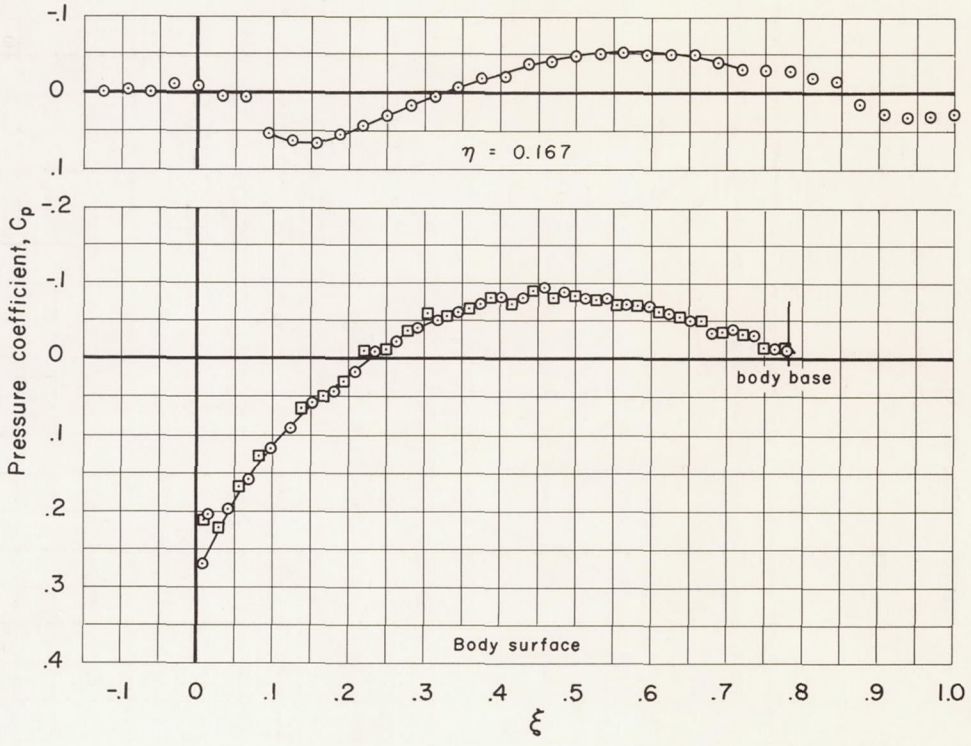

(k) $M_\infty = 1.15$, S_{max} at $\xi = 0.40$

Figure 8.- Continued.

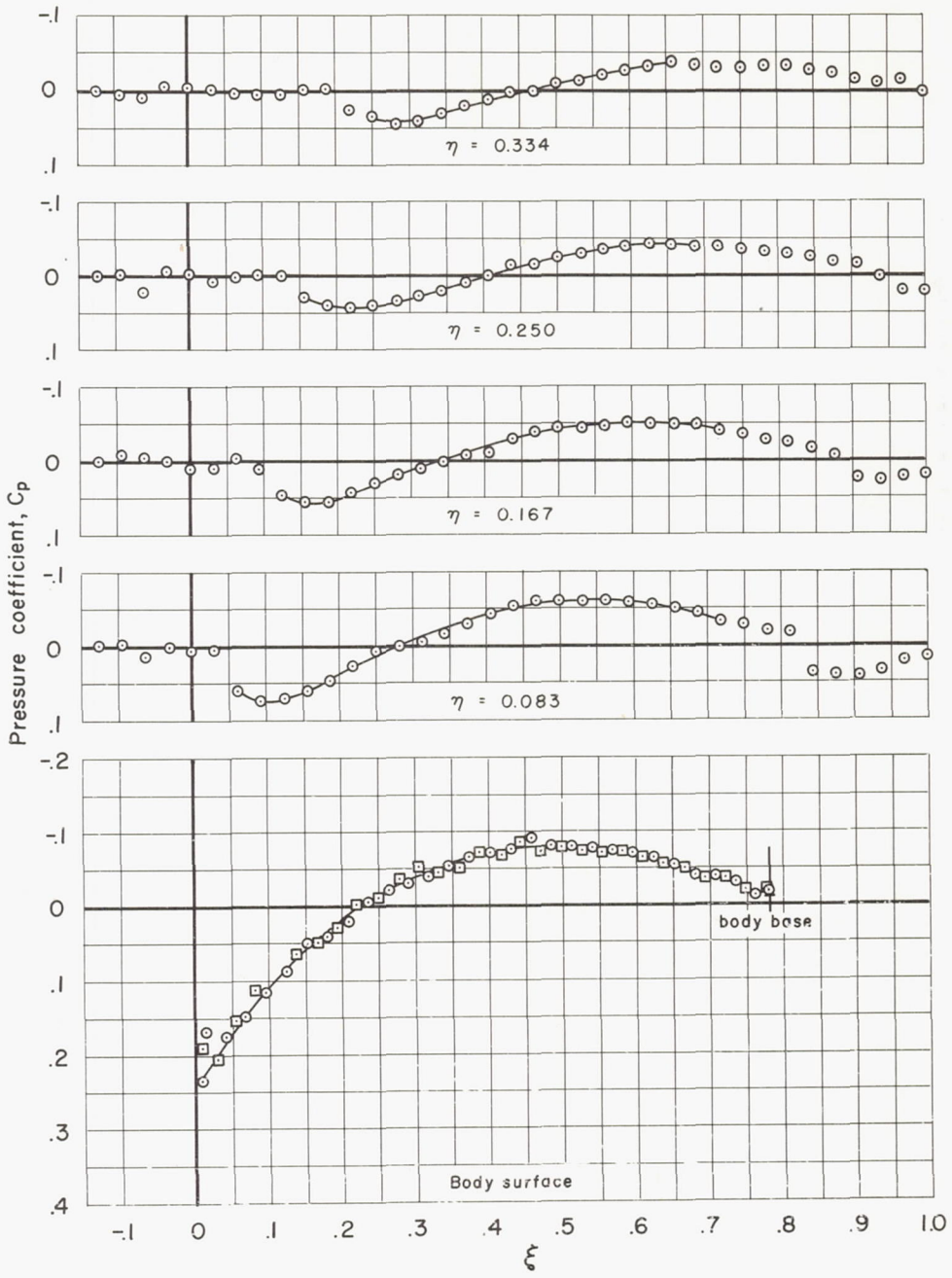

(l) M_∞ = 1.20, S_{max} at ξ = 0.40

Figure 8.- Continued.

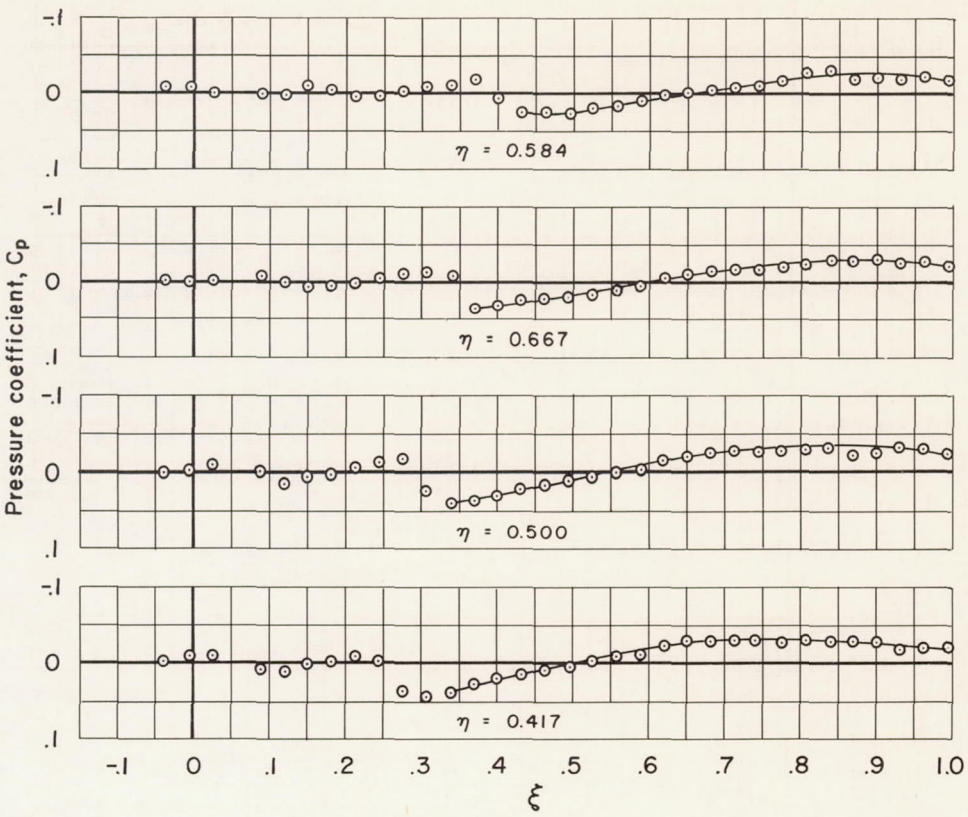

(l) M_∞ = 1.20, S_{max} at ξ = 0.40 - Concluded.

Figure 8.- Concluded.

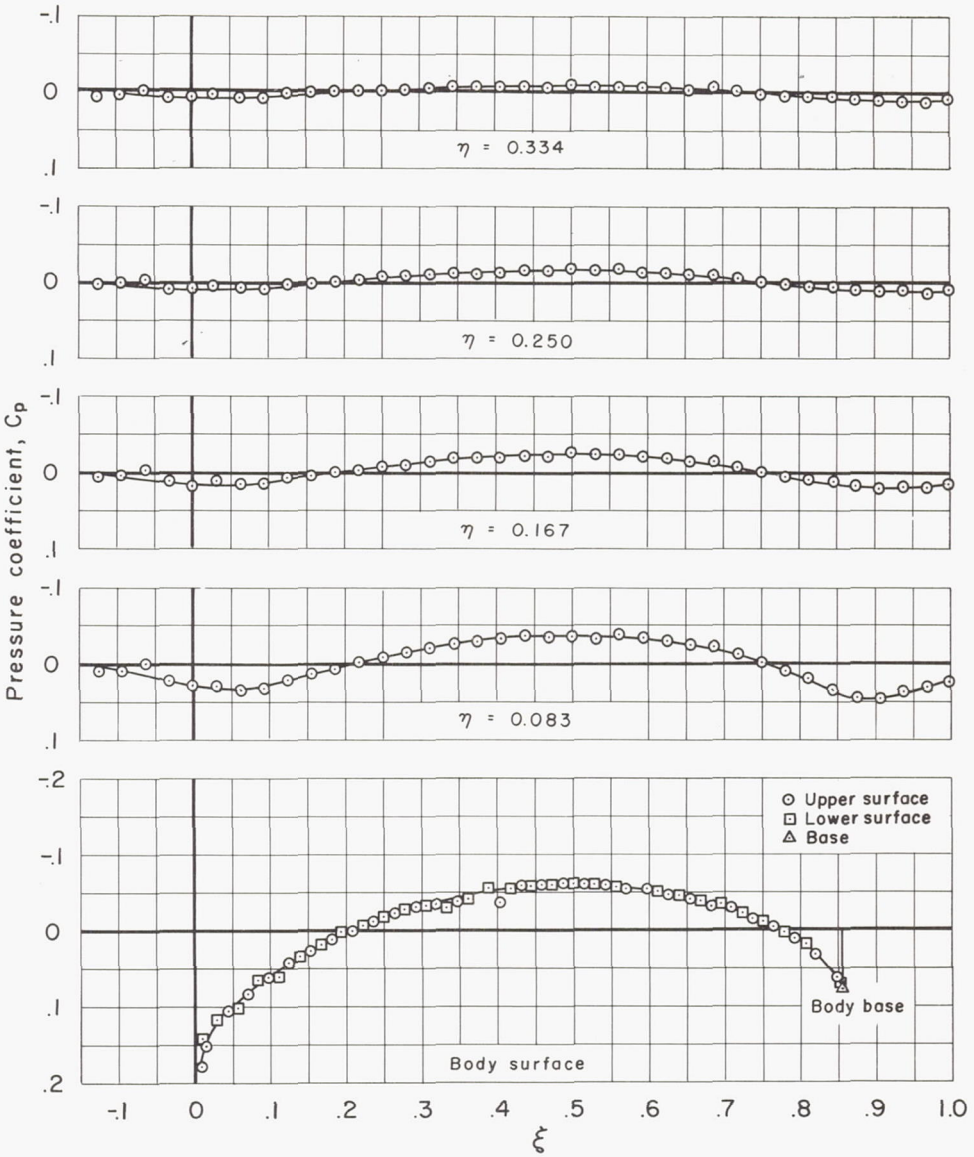

(a) $M_\infty = 0.80$, S_{max} at $\xi = 0.50$

Figure 9.- Experimental pressure distributions for the body with maximum cross-sectional area at $\xi = 0.50$.

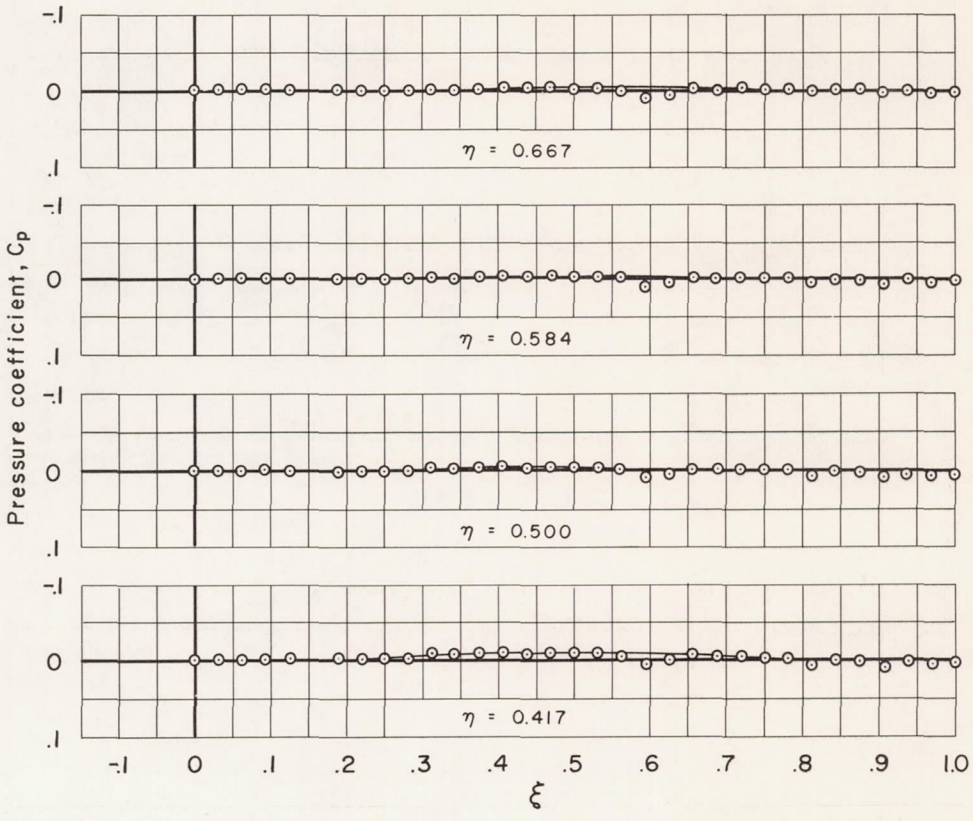

(a) $M_\infty = 0.80$, S_{max} at $\xi = 0.50$ - Concluded.

Figure 9.- Continued.

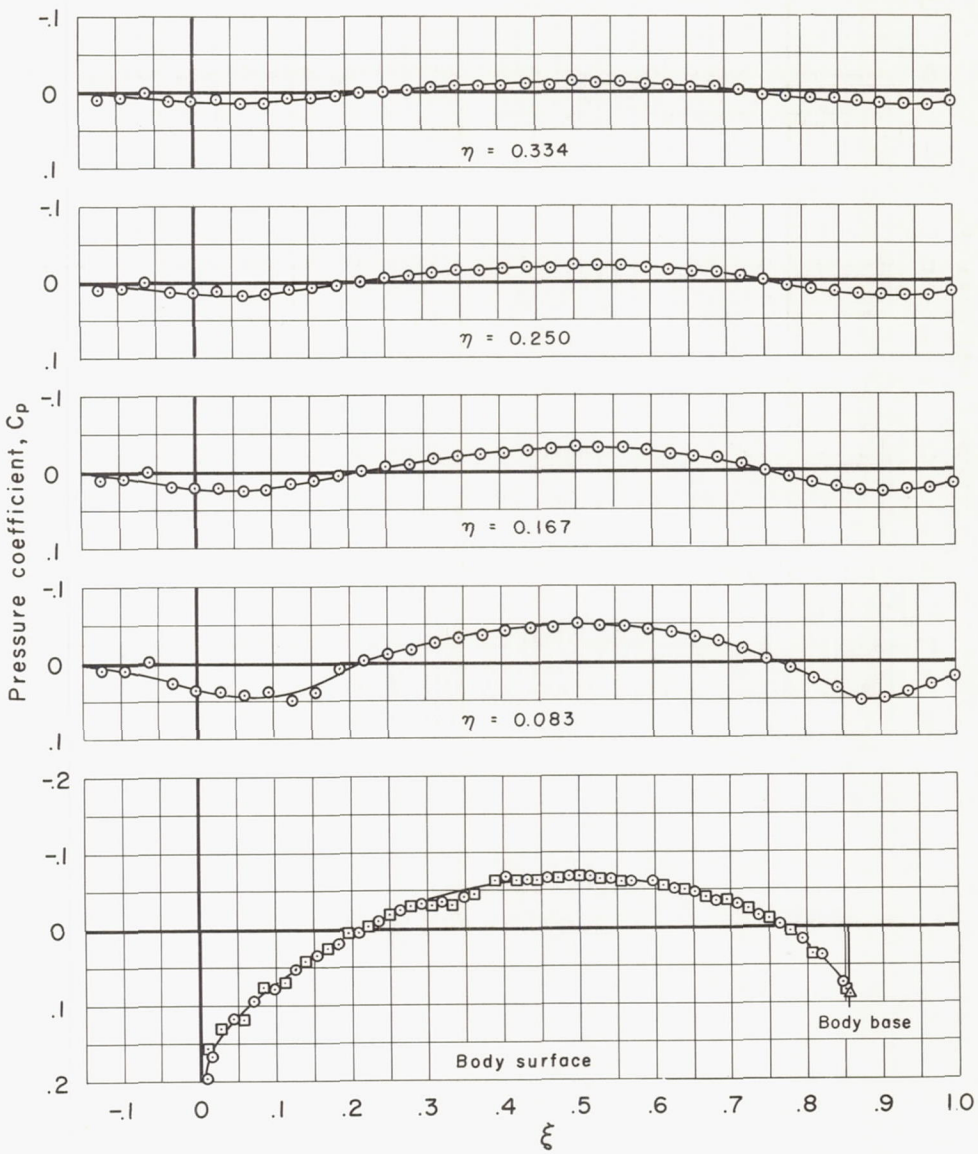

(b) $M_\infty = 0.90$, S_{max} at $\xi = 0.50$

Figure 9.- Continued.

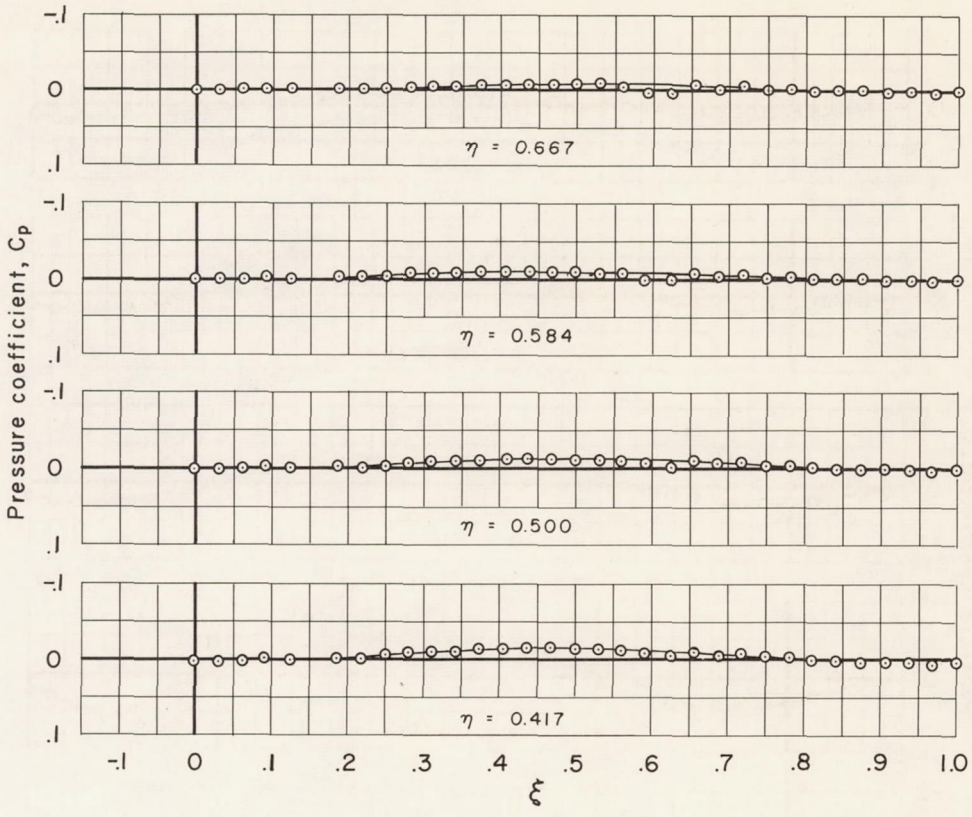

(b) $M_\infty = 0.90$, S_{max} at $\xi = 0.50$ - Concluded.

Figure 9.- Continued.

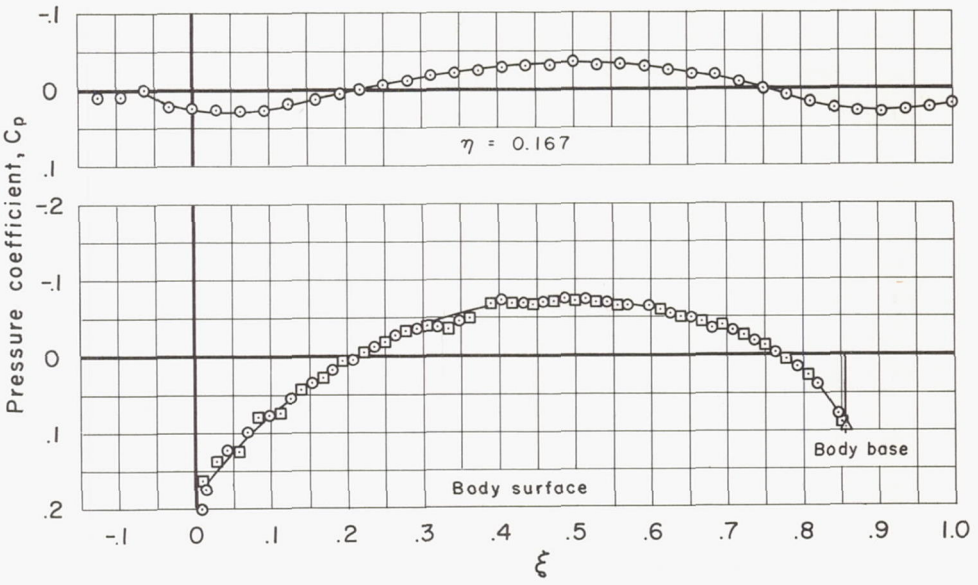

(c) $M_\infty = 0.925$, S_{max} at $\xi = 0.50$

Figure 9.- Continued.

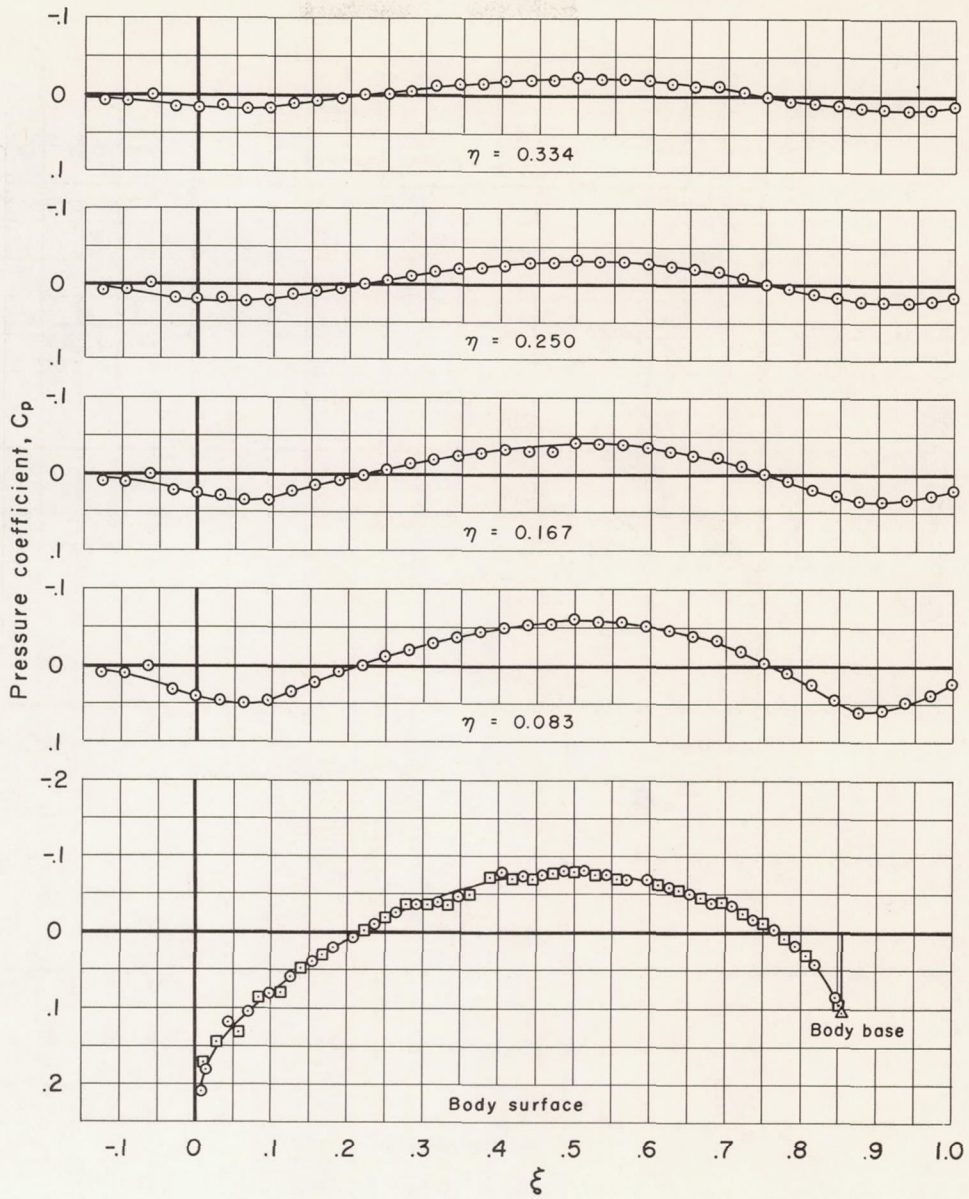

(d) $M_\infty = 0.95$, S_{max} at $\xi = 0.50$

Figure 9.- Continued.

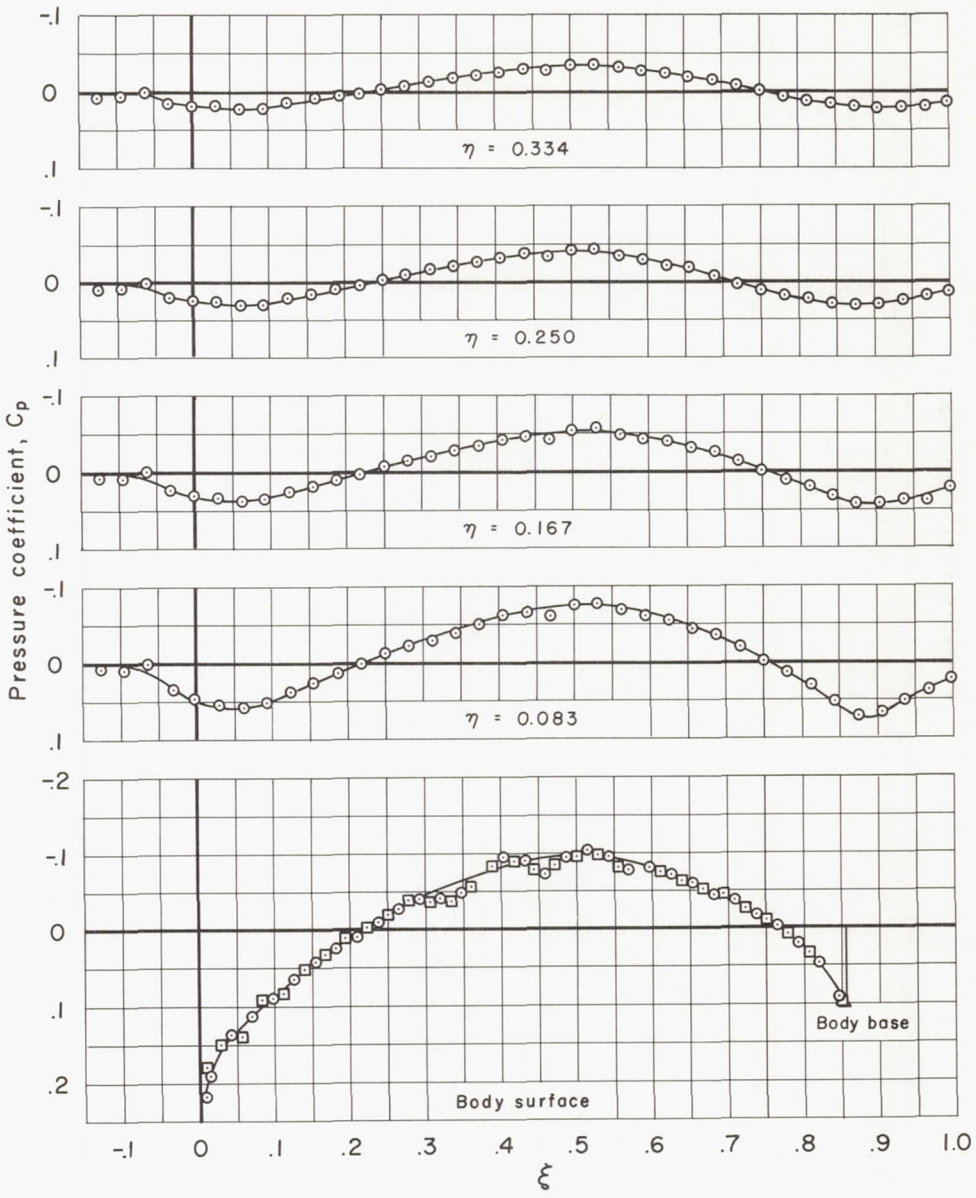

(e) M_∞ = 0.975, S_{max} at ξ = 0.50

Figure 9.- Continued.

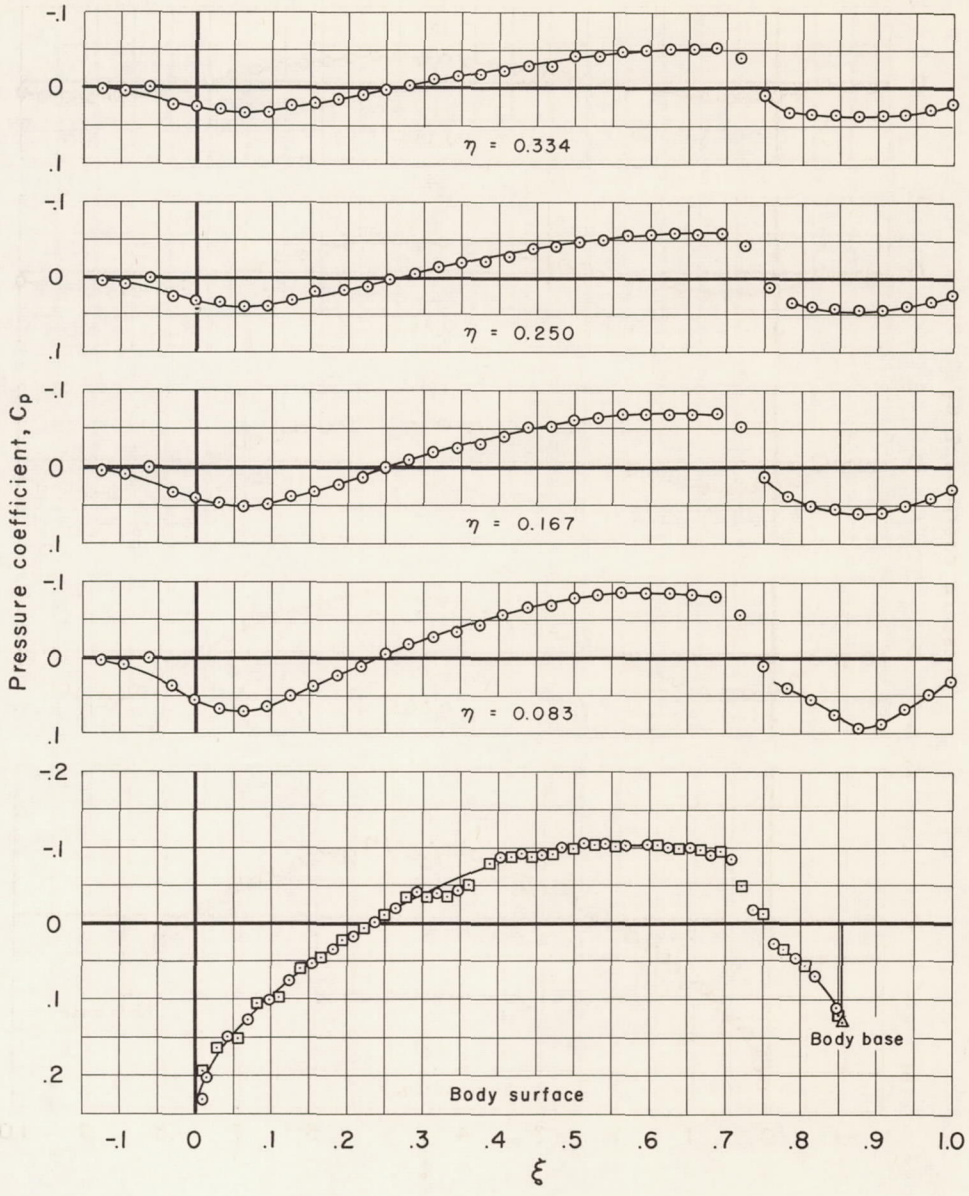

(f) $M_\infty = 1.00$, S_{max} at $\xi = 0.50$

Figure 9.- Continued.

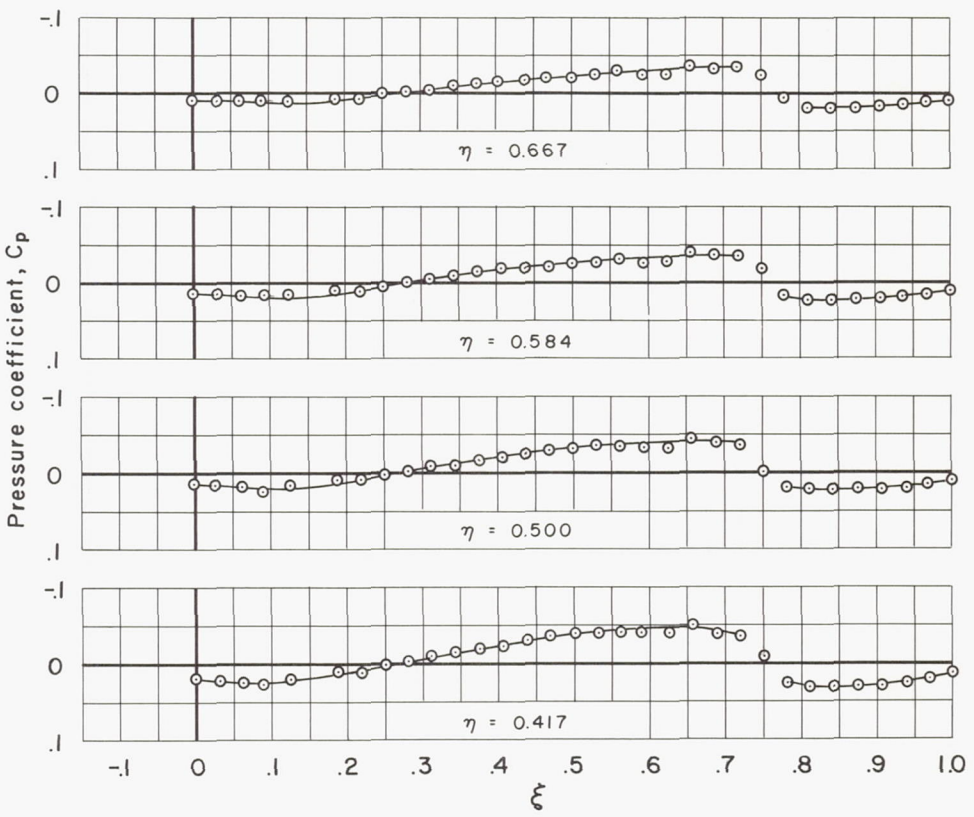

(f) M_∞ = 1.00, S_{max} at ξ = 0.50 - Concluded.

Figure 9.- Continued.

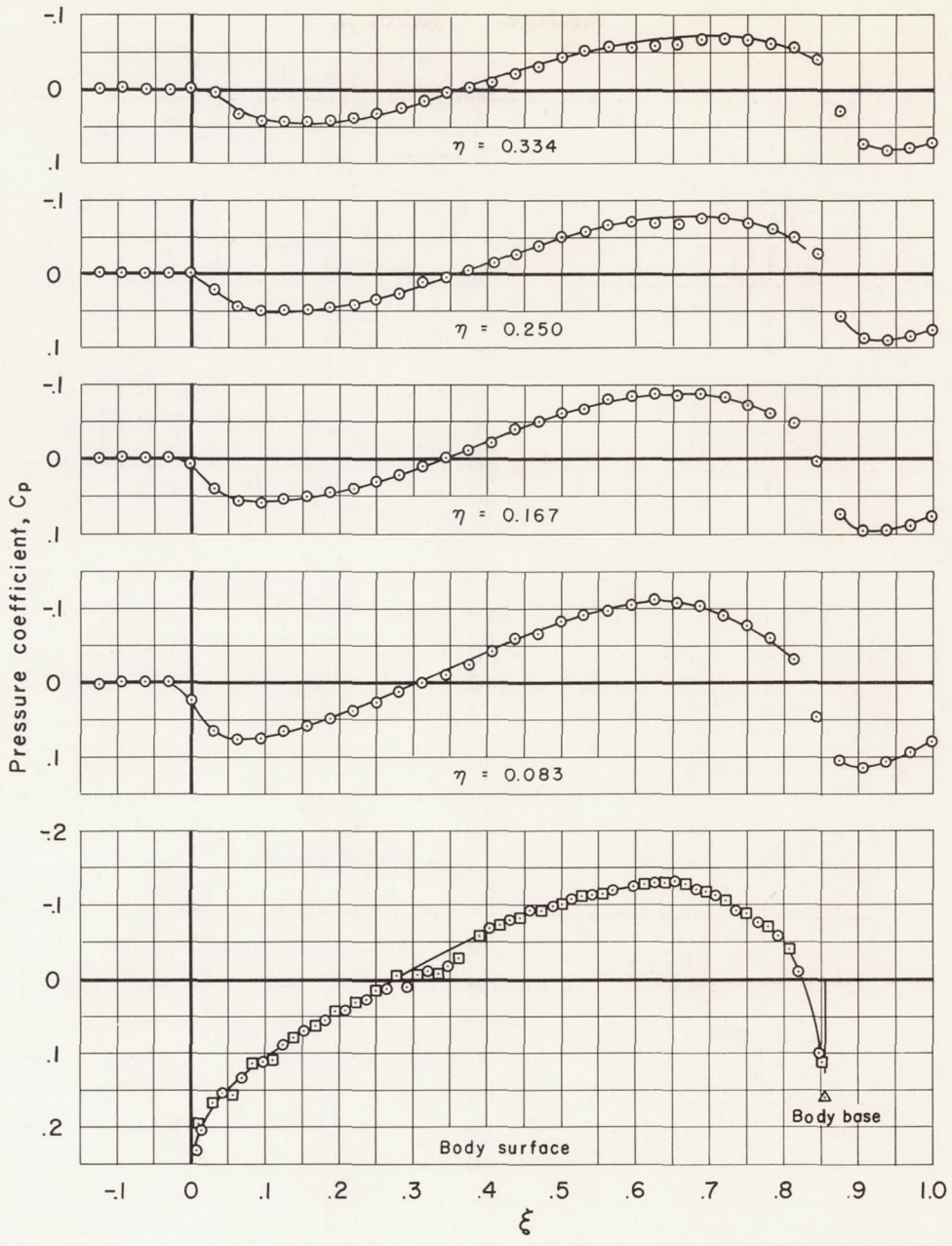

(g) $M_\infty = 1.025$, S_{max} at $\xi = 0.50$

Figure 9.- Continued.

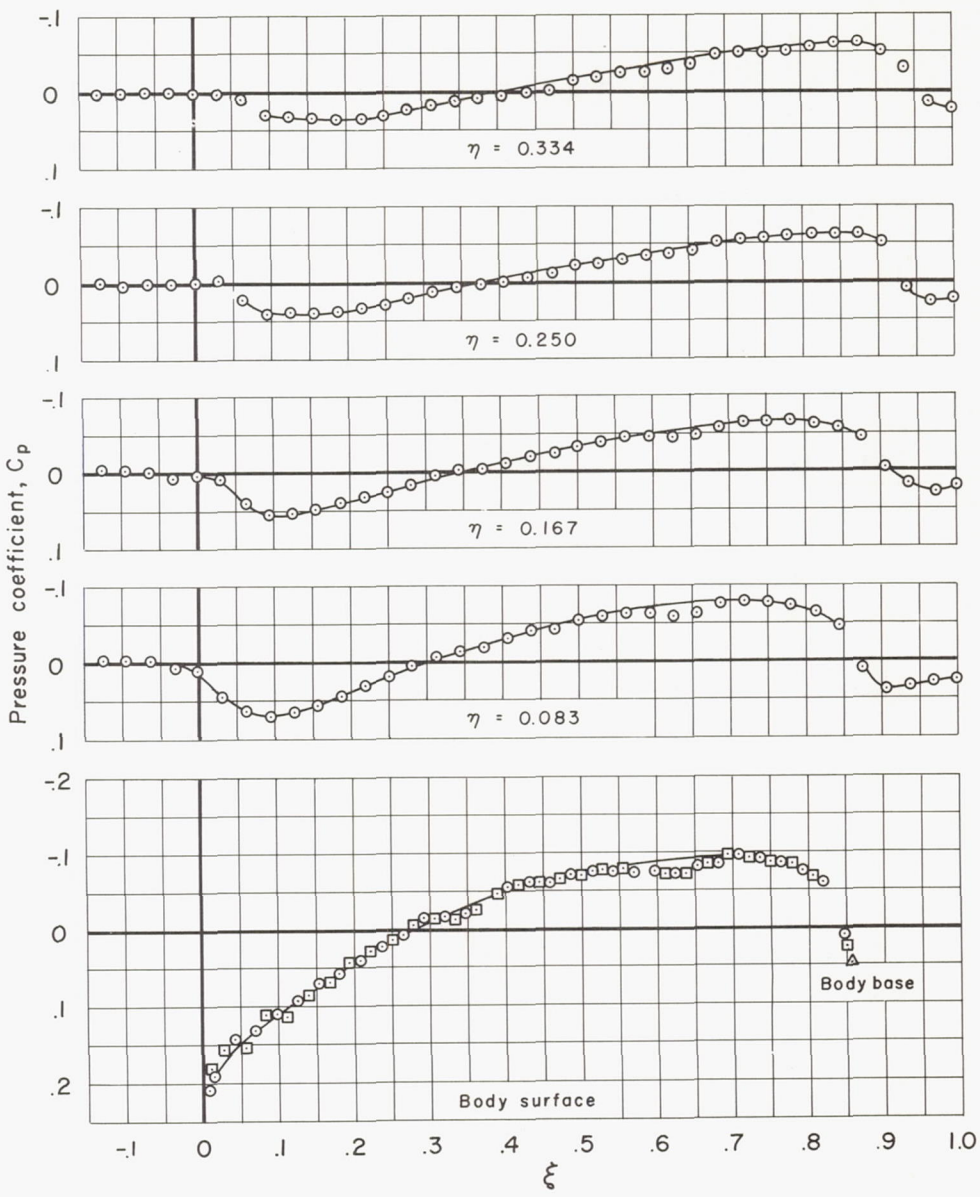

(h) M_∞ = 1.05, S_{max} at ξ = 0.50

Figure 9.- Continued.

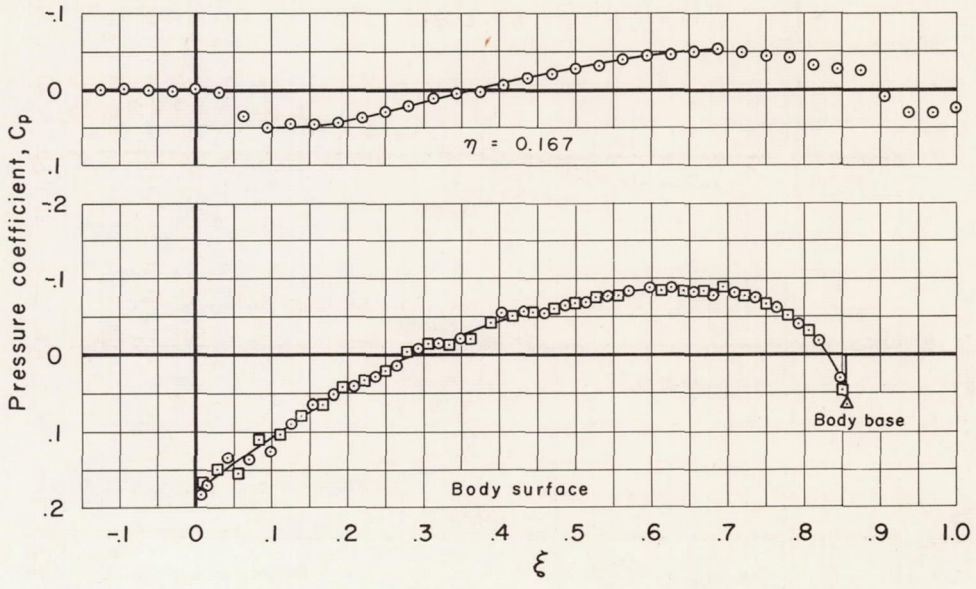

(i) $M_\infty = 1.075$, S_{max} at $\xi = 0.50$

Figure 9.- Continued.

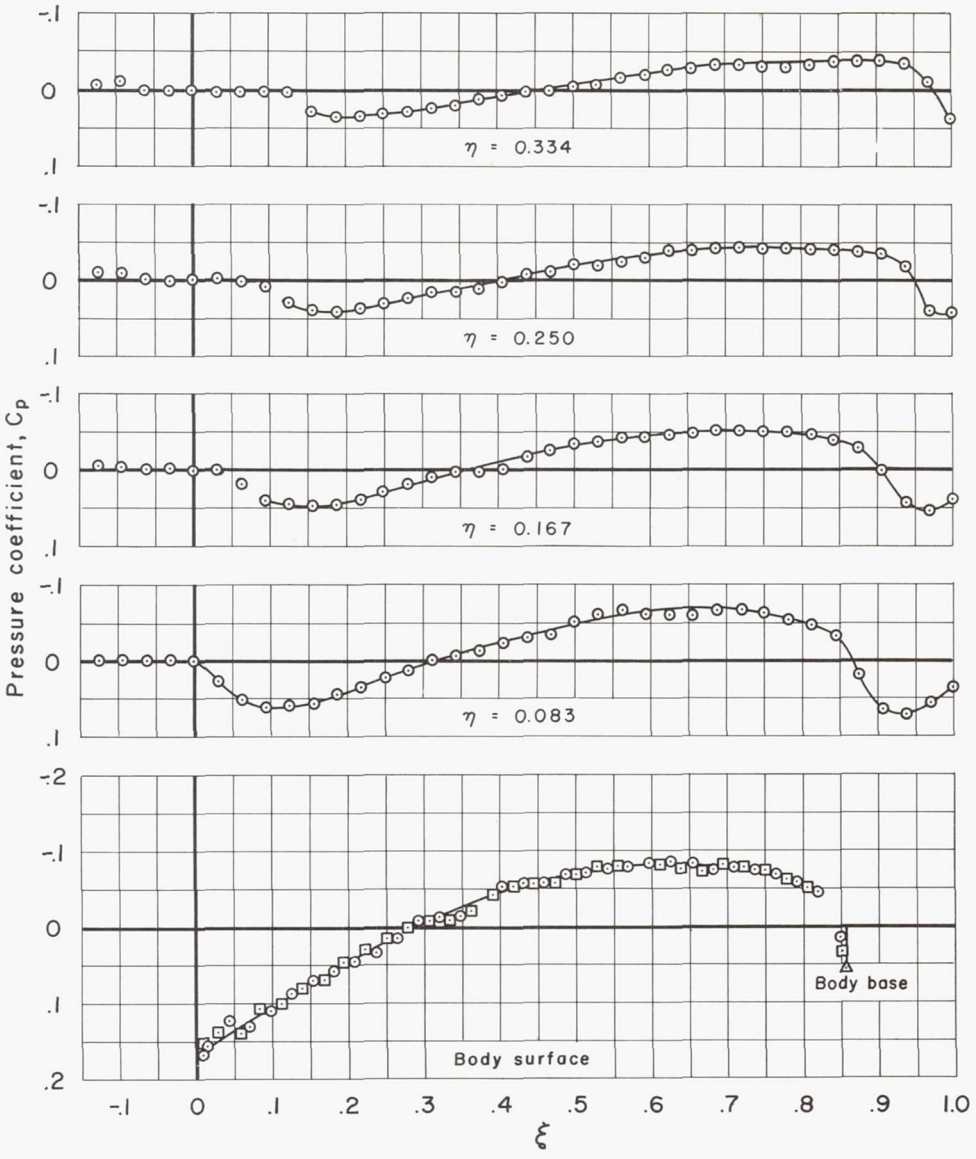

(j) M_∞ = 1.10, S_{max} at ξ = 0.50

Figure 9.- Continued.

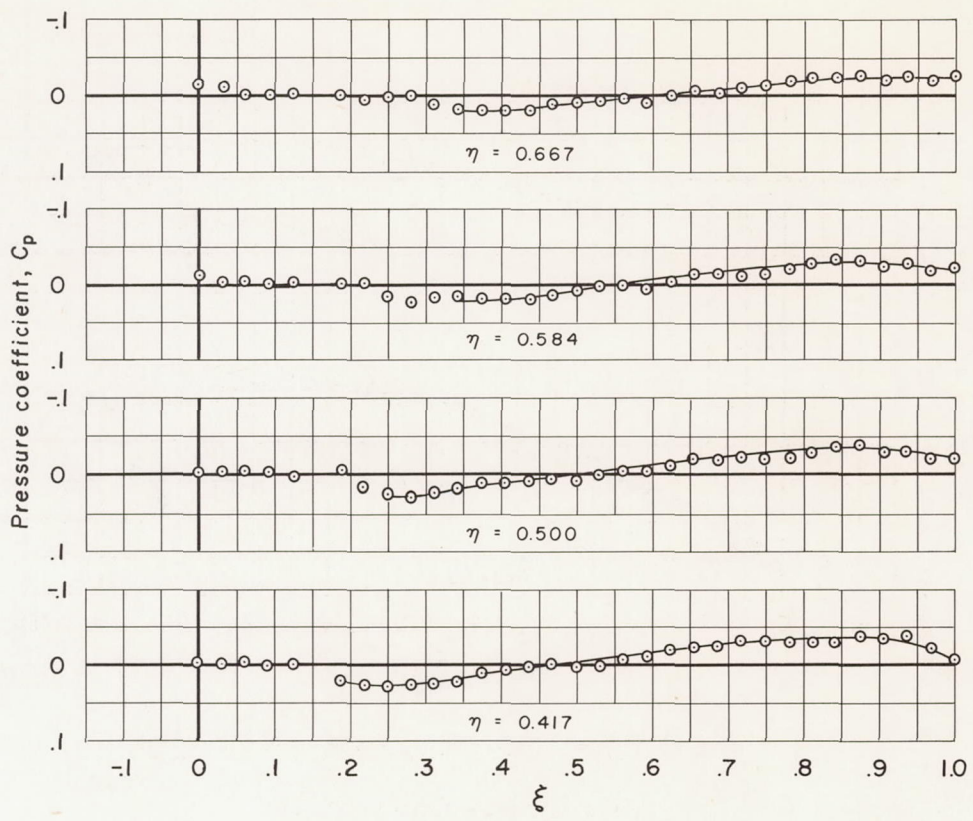

(j) M_∞ = 1.10, S_{max} at ξ = 0.50 - Concluded.

Figure 9.- Continued.

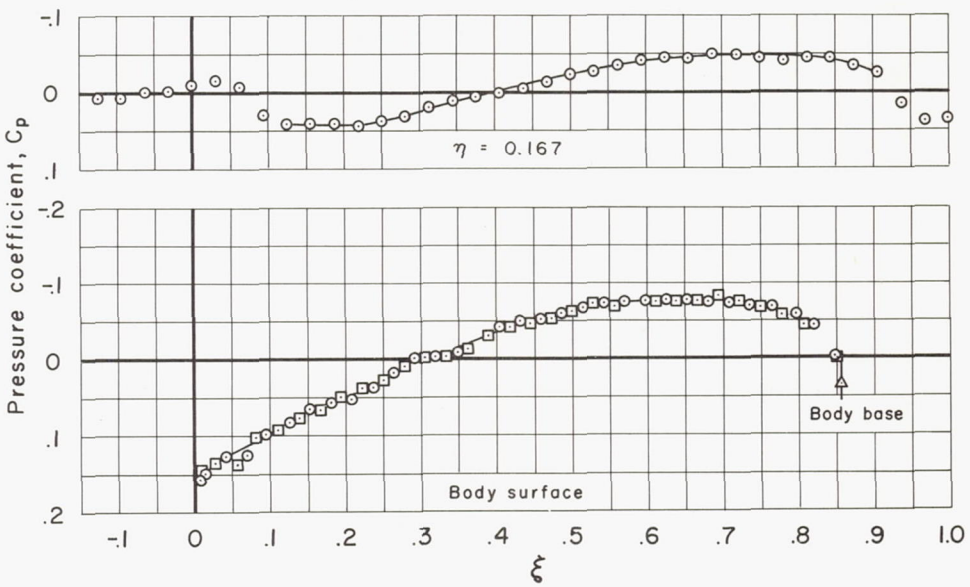

(k) $M_\infty = 1.15$, S_{max} at $\xi = 0.50$

Figure 9.- Continued.

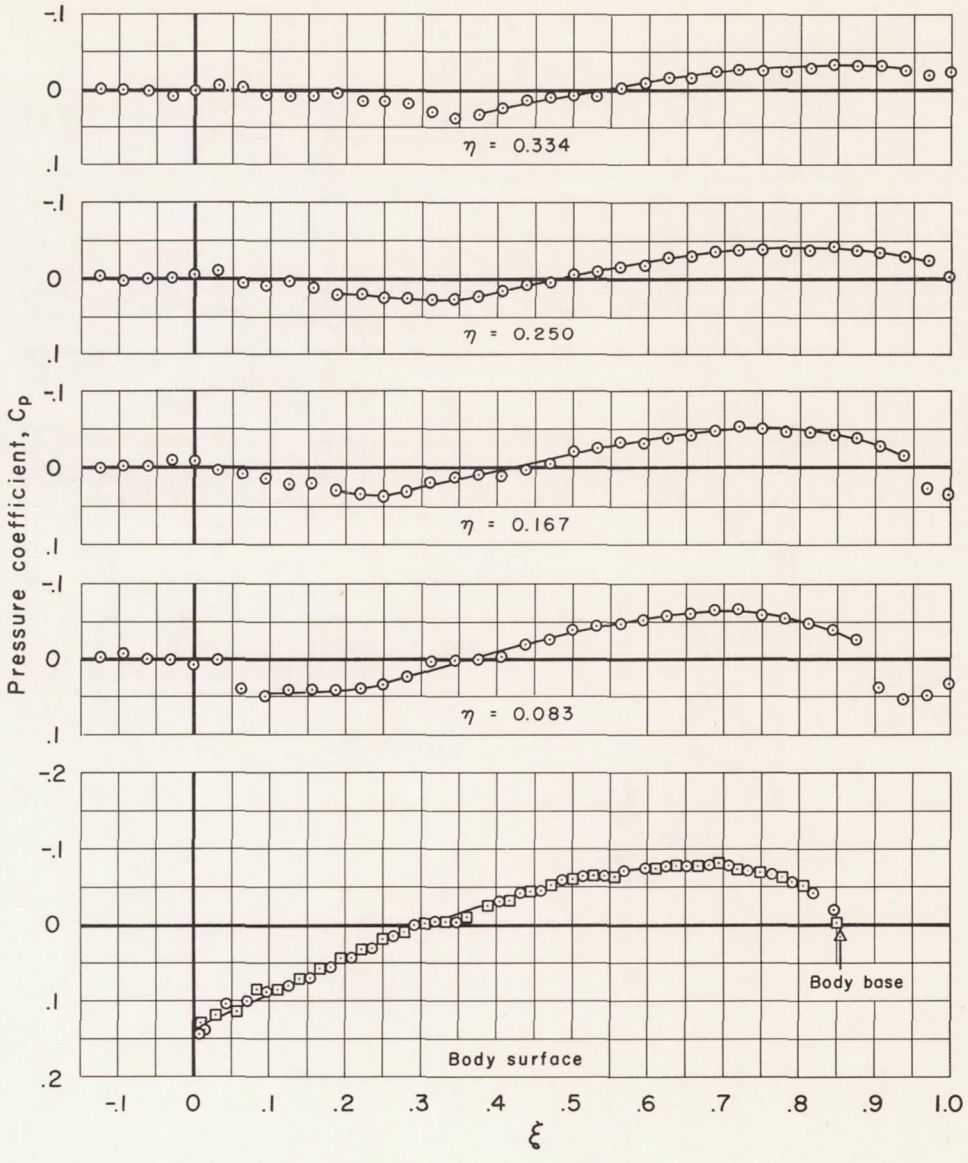

(l) M_∞ = 1.20, S_{max} at ξ = 0.50

Figure 9.- Continued.

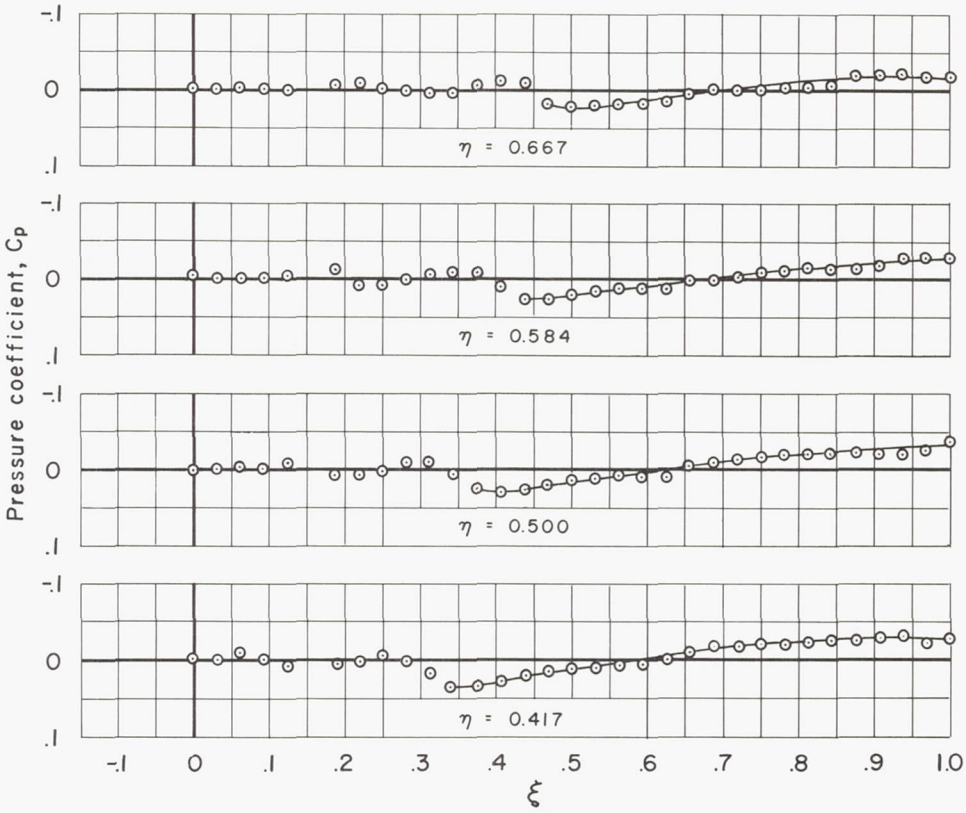

(l) M_∞ = 1.20, S_{max} at ξ = 0.50 - Concluded.

Figure 9.- Concluded.

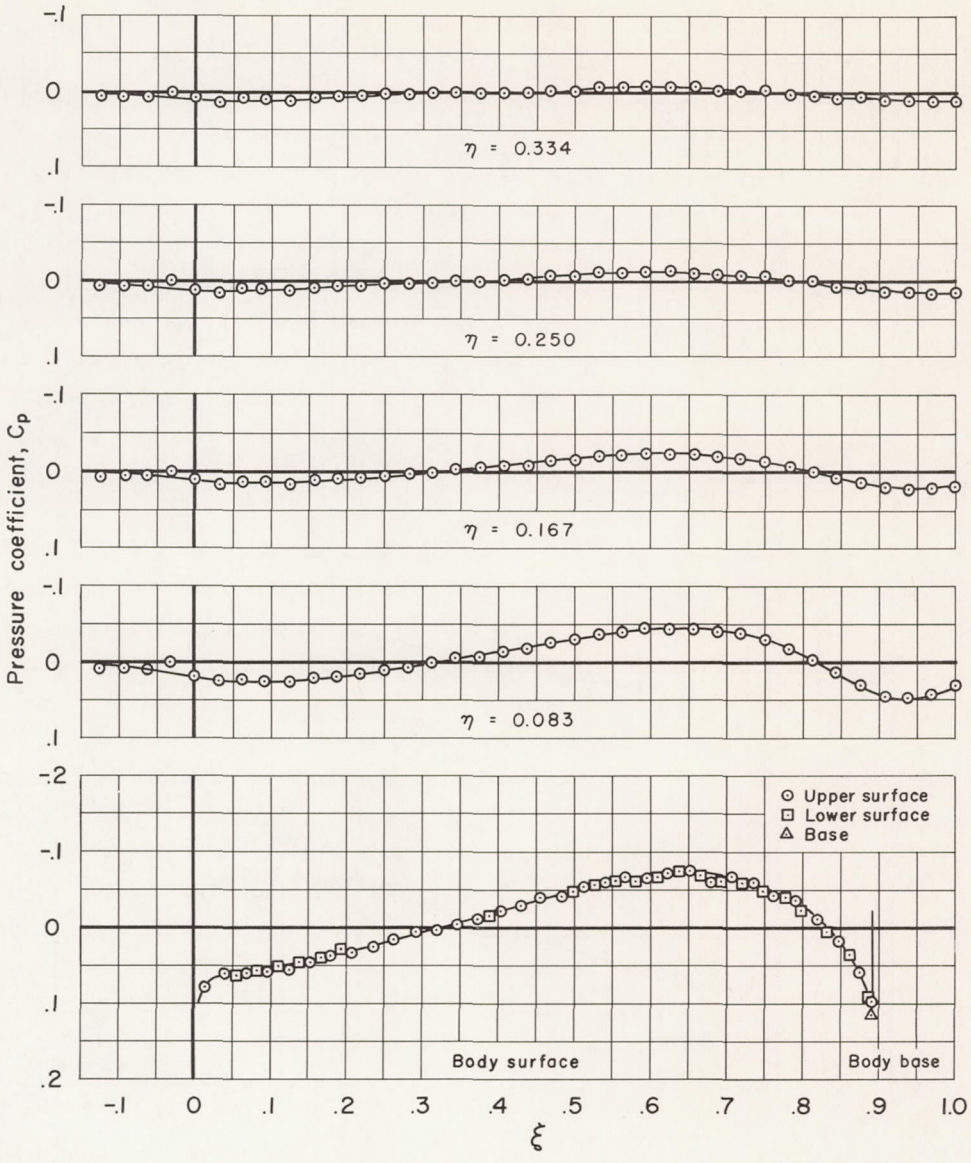

(a) $M_\infty = 0.80$, S_{max} at $\xi = 0.60$

Figure 10.- Experimental pressure distributions for the body with maximum cross-sectional area at $\xi = 0.60$.

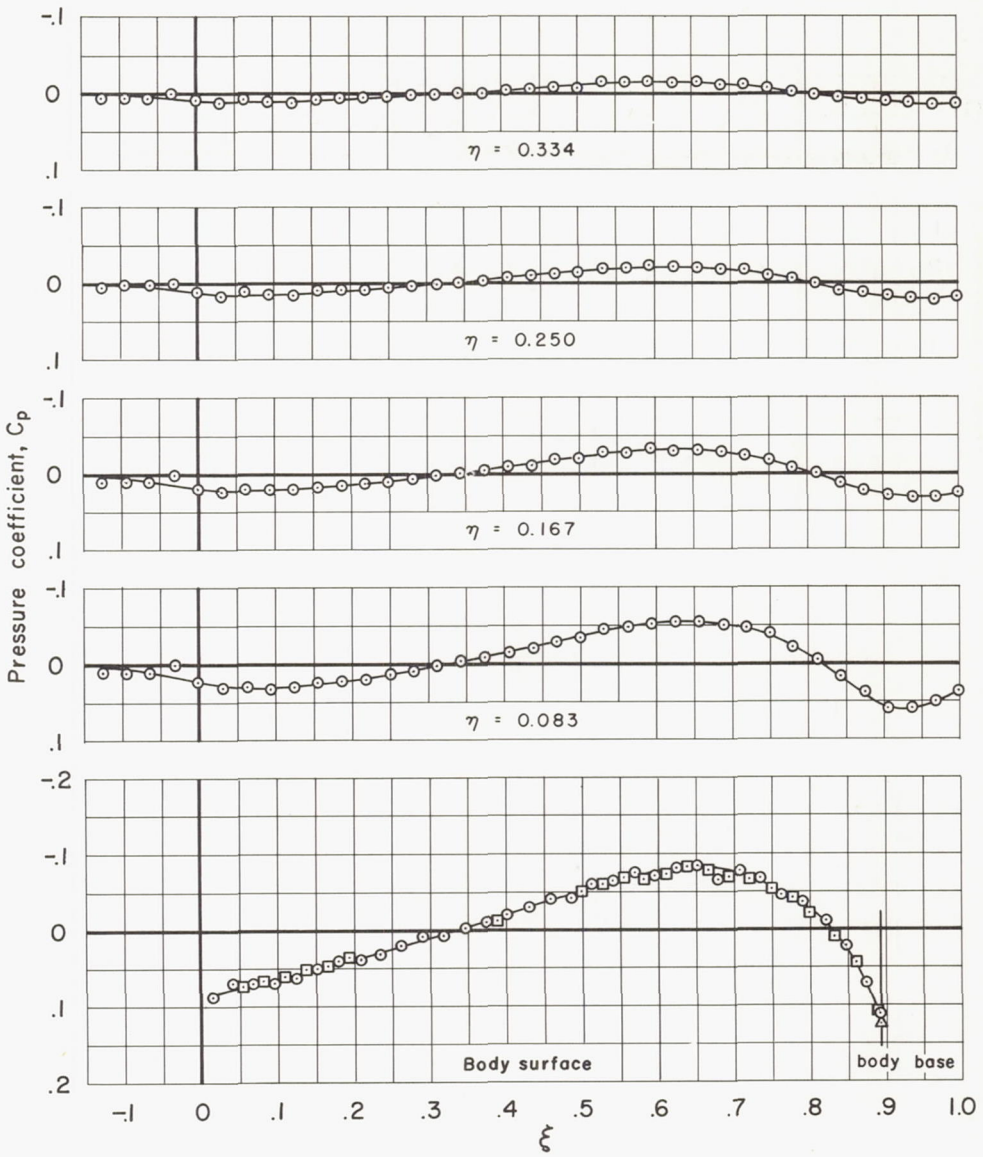

(b) $M_\infty = 0.90$, S_{max} at $\xi = 0.60$

Figure 10.- Continued.

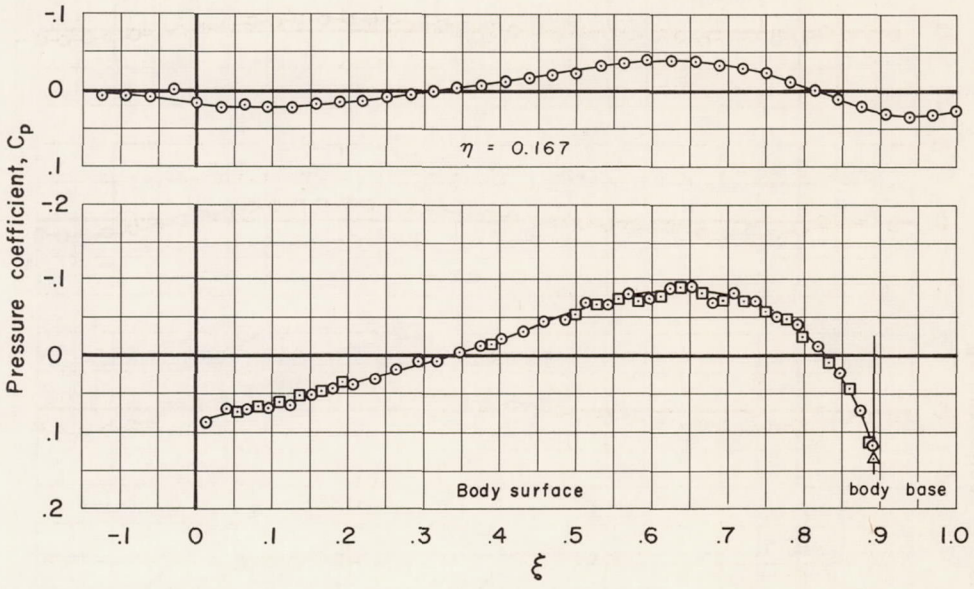

(c) $M_\infty = 0.925$, S_{max} at $\xi = 0.60$

Figure 10.- Continued.

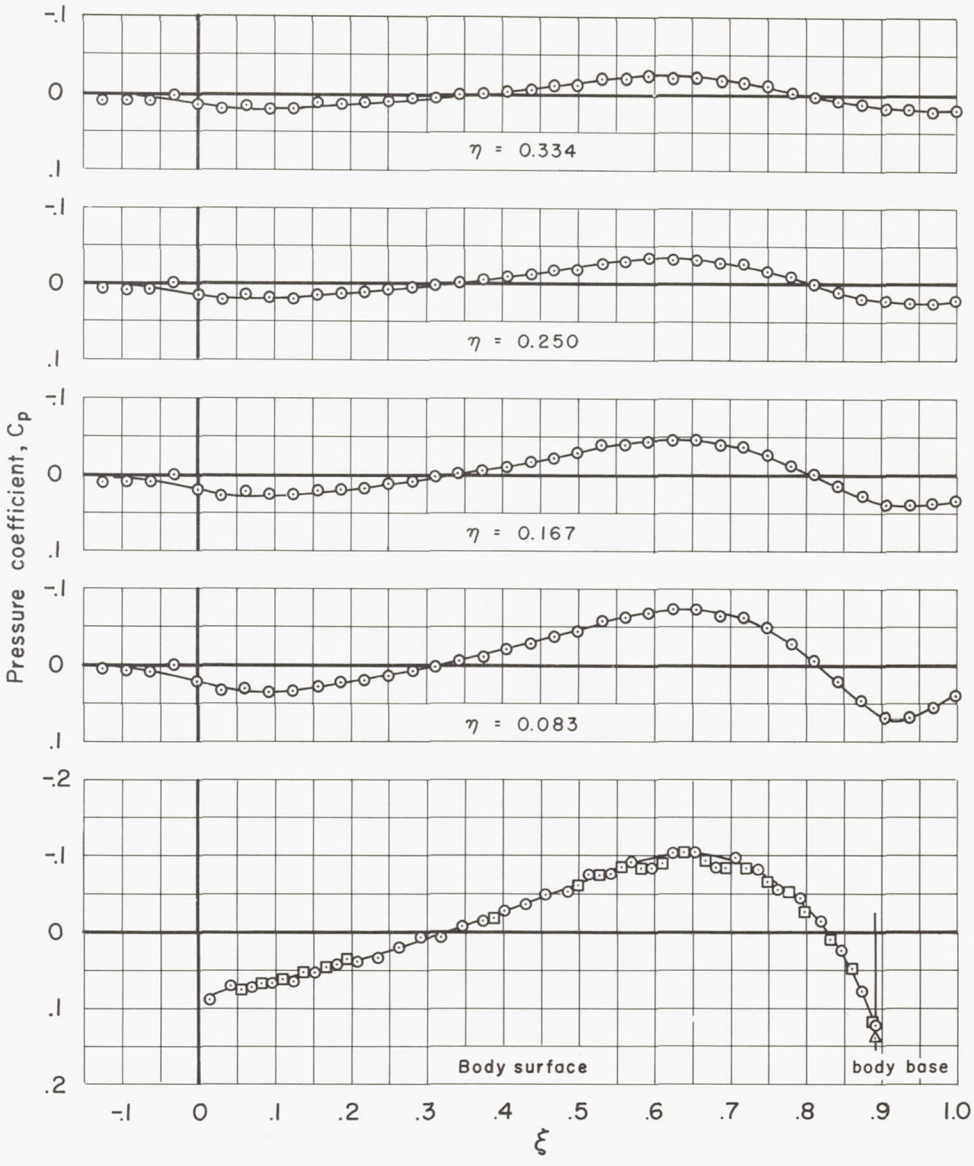

(d) $M_\infty = 0.95$, S_{max} at $\xi = 0.60$

Figure 10.- Continued.

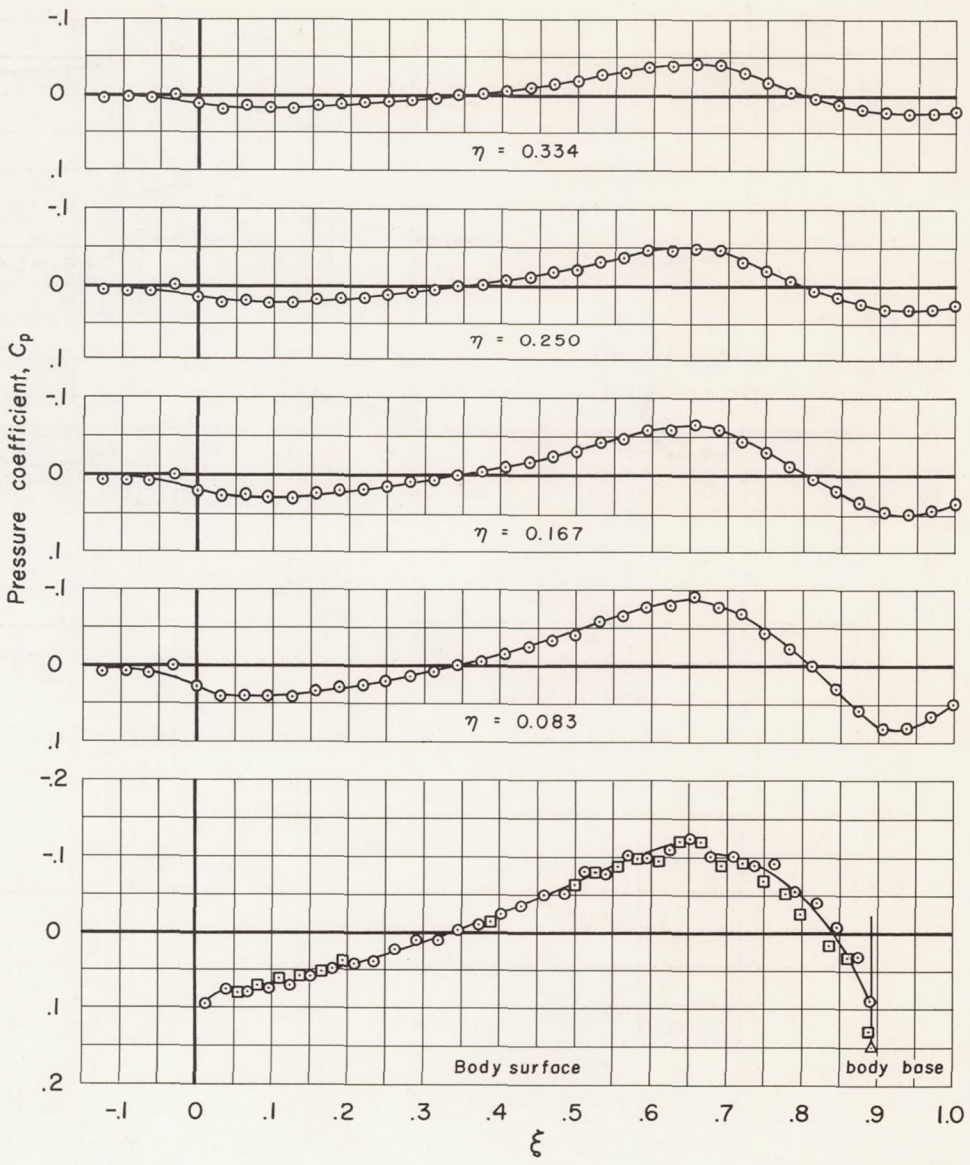

(e) $M_\infty = 0.975$, S_{max} at $\xi = 0.60$

Figure 10.- Continued.

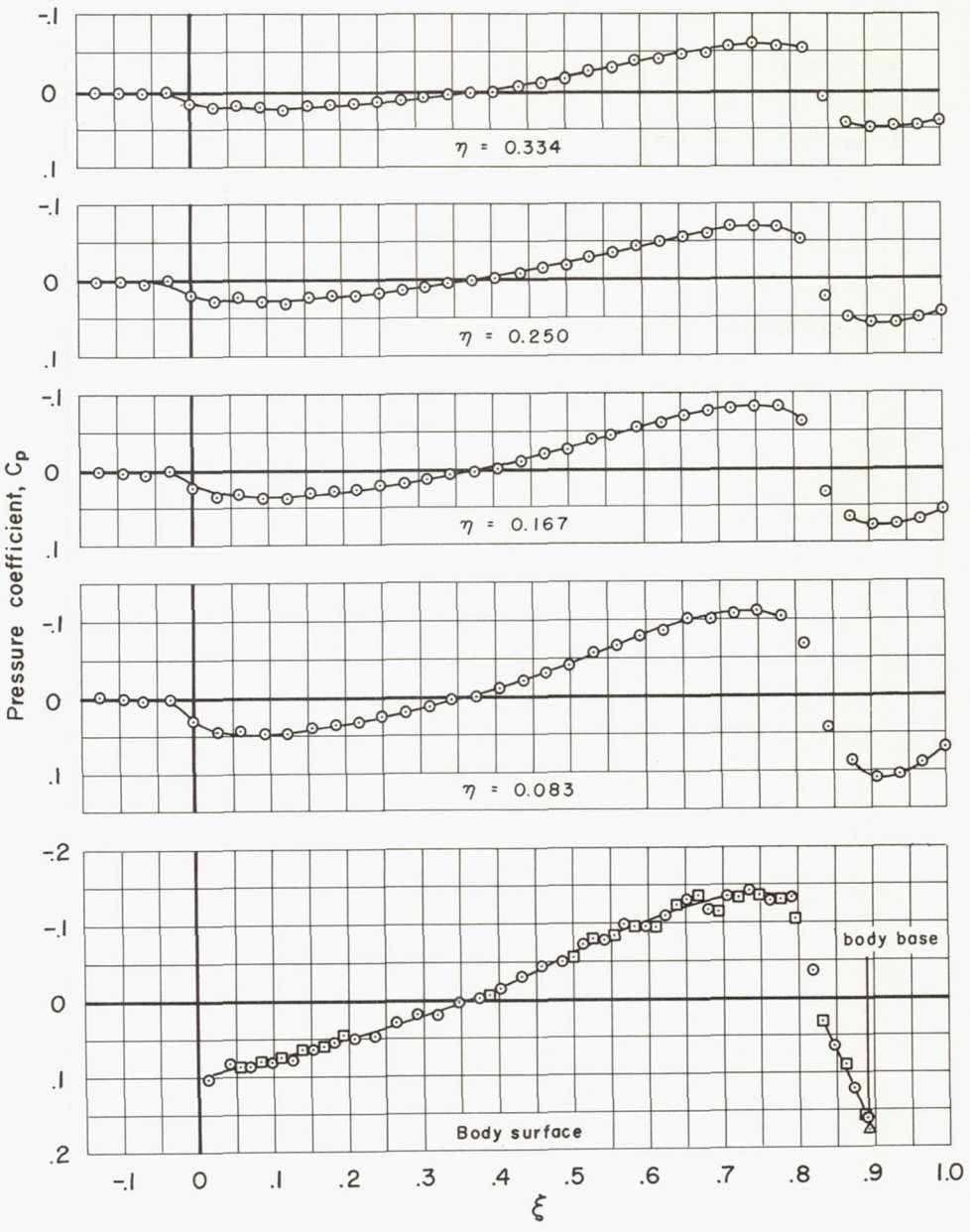

(f) M_∞ = 1.00, S_{max} at ξ = 0.60

Figure 10.- Continued.

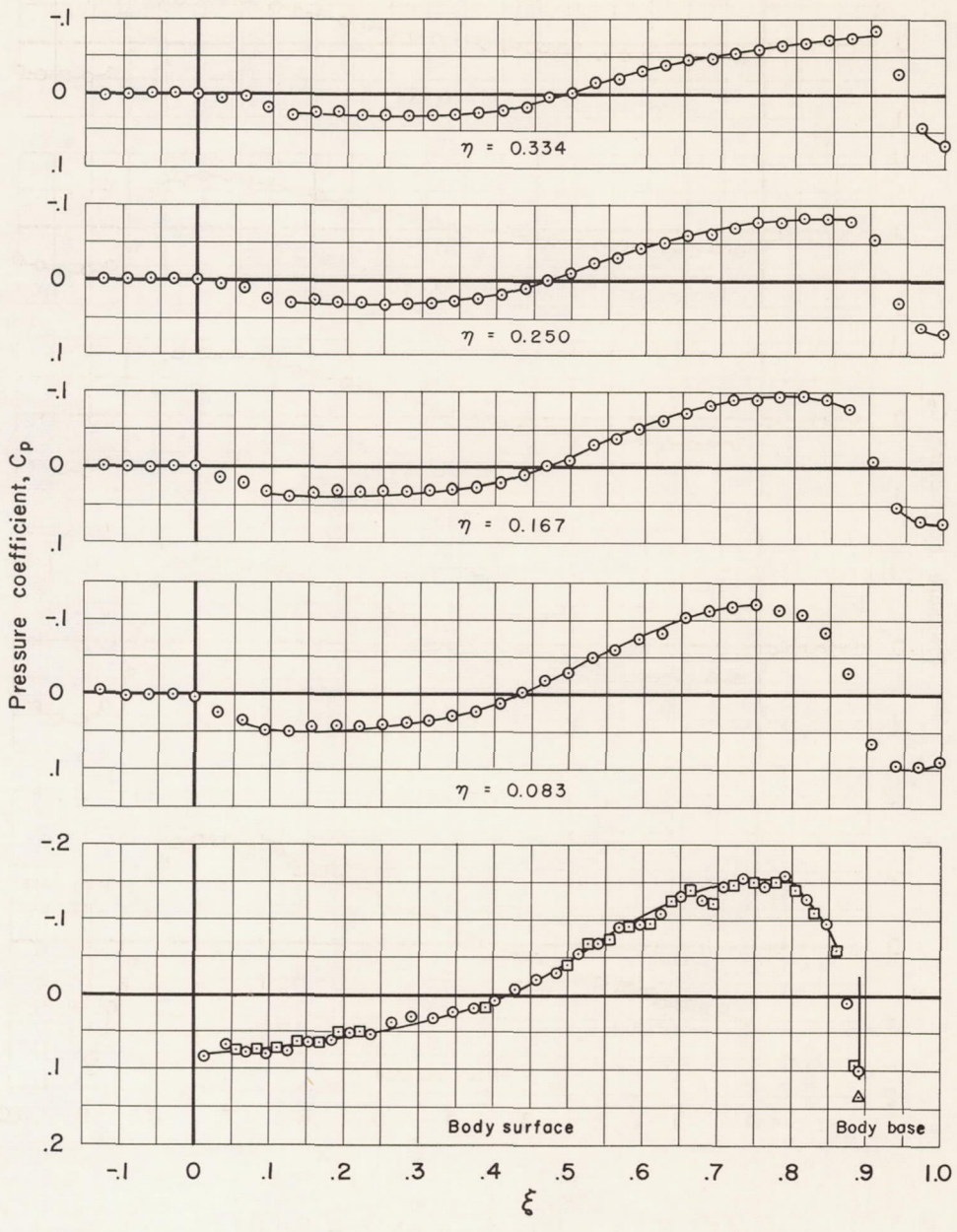

(g) M_∞ = 1.025, S_{max} at ξ = 0.60

Figure 10.- Continued.

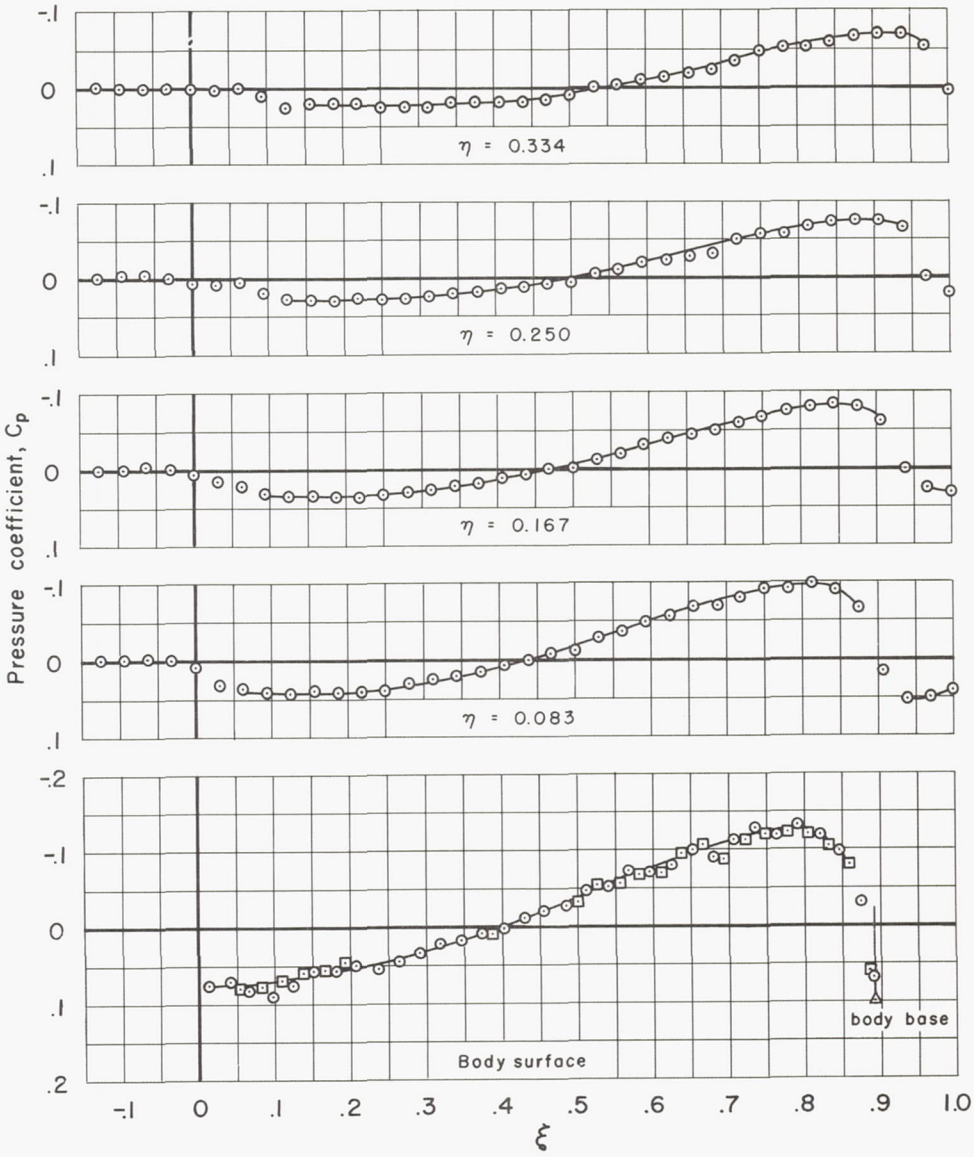

(h) $M_\infty = 1.05$, S_{max} at $\xi = 0.60$

Figure 10.- Continued.

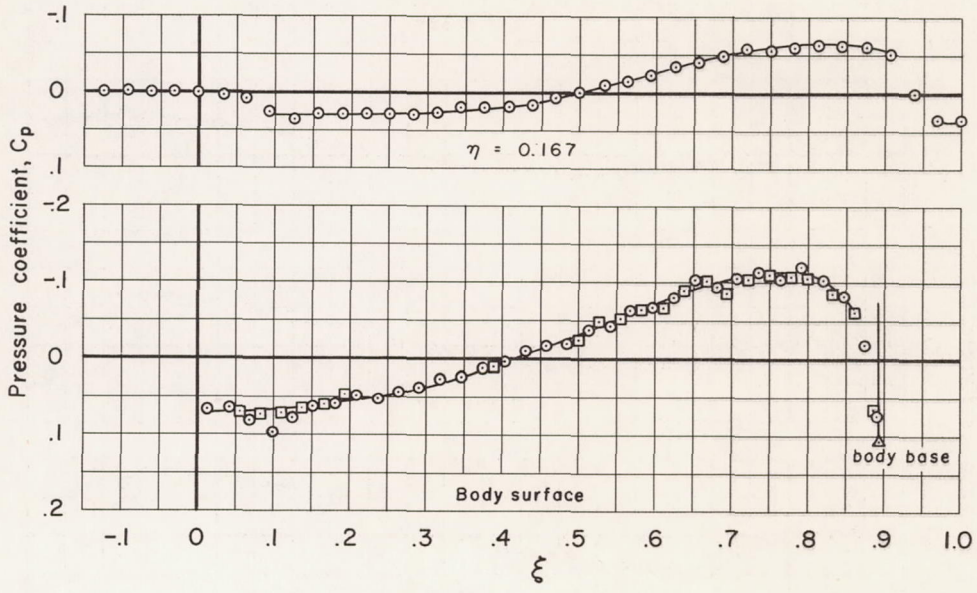

(i) M_∞ = 1.075, S_{max} at ξ = 0.60

Figure 10.- Continued.

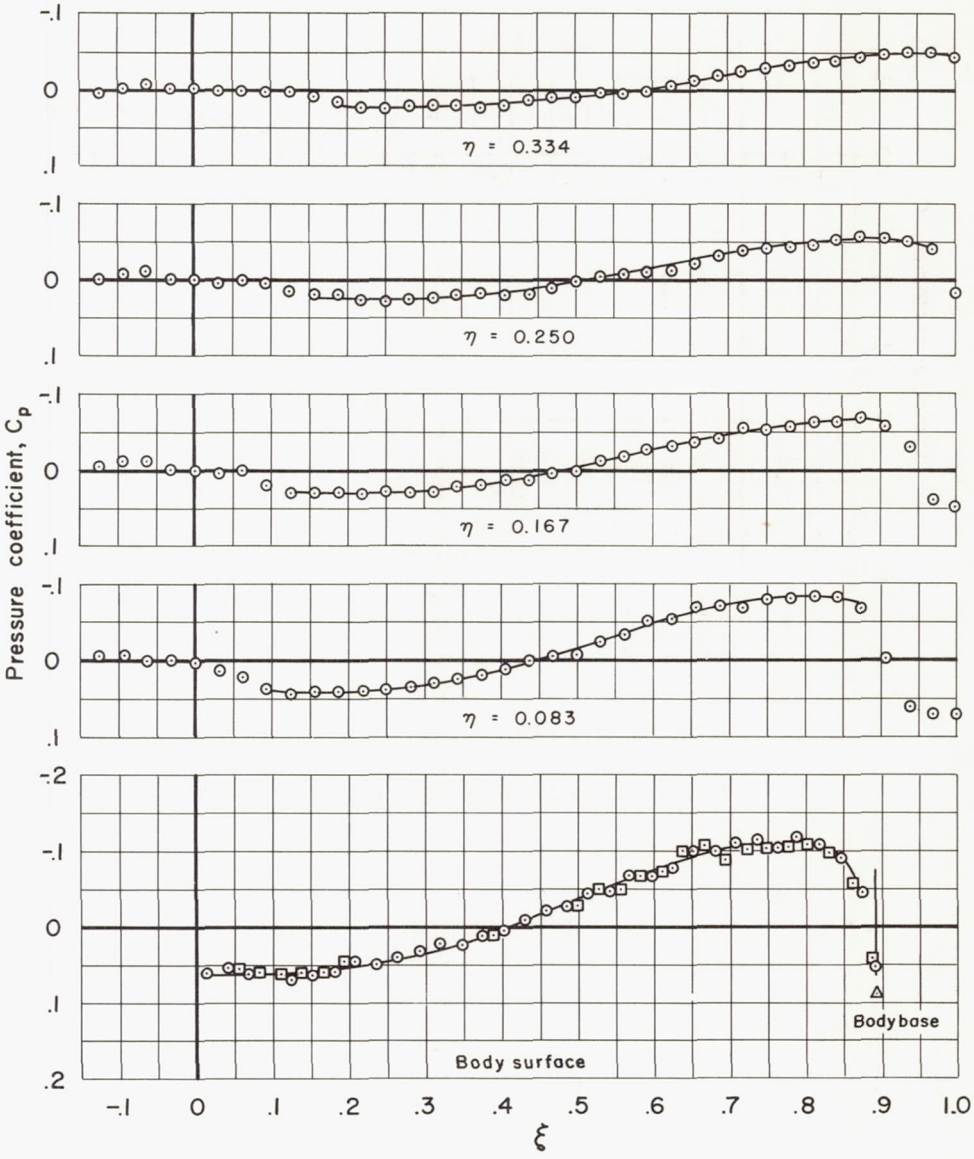

(j) M_∞ = 1.10, S_{max} at ξ = 0.60

Figure 10.- Continued.

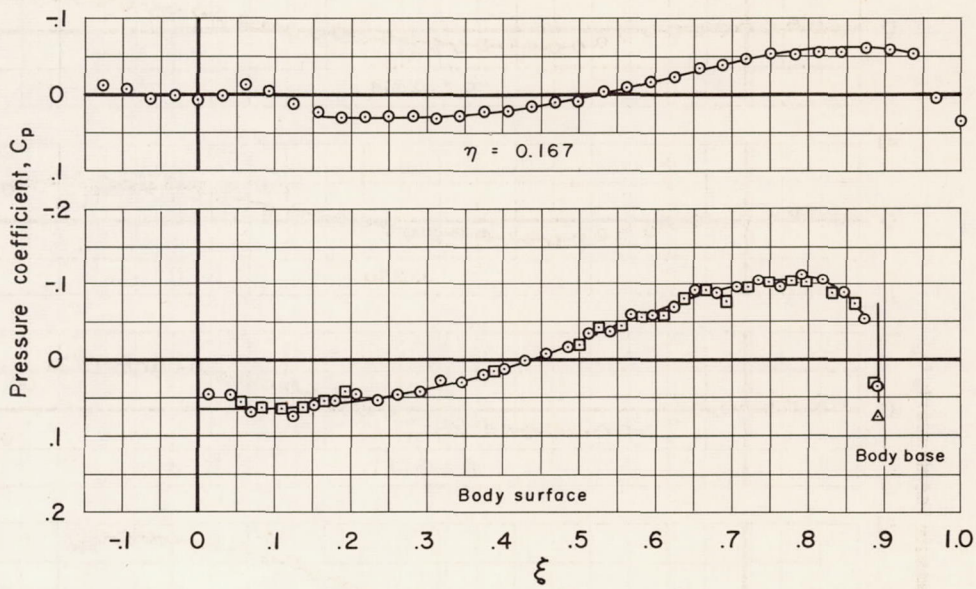

(k) M_∞ = 1.15, S_{max} at ξ = 0.60

Figure 10.- Continued.

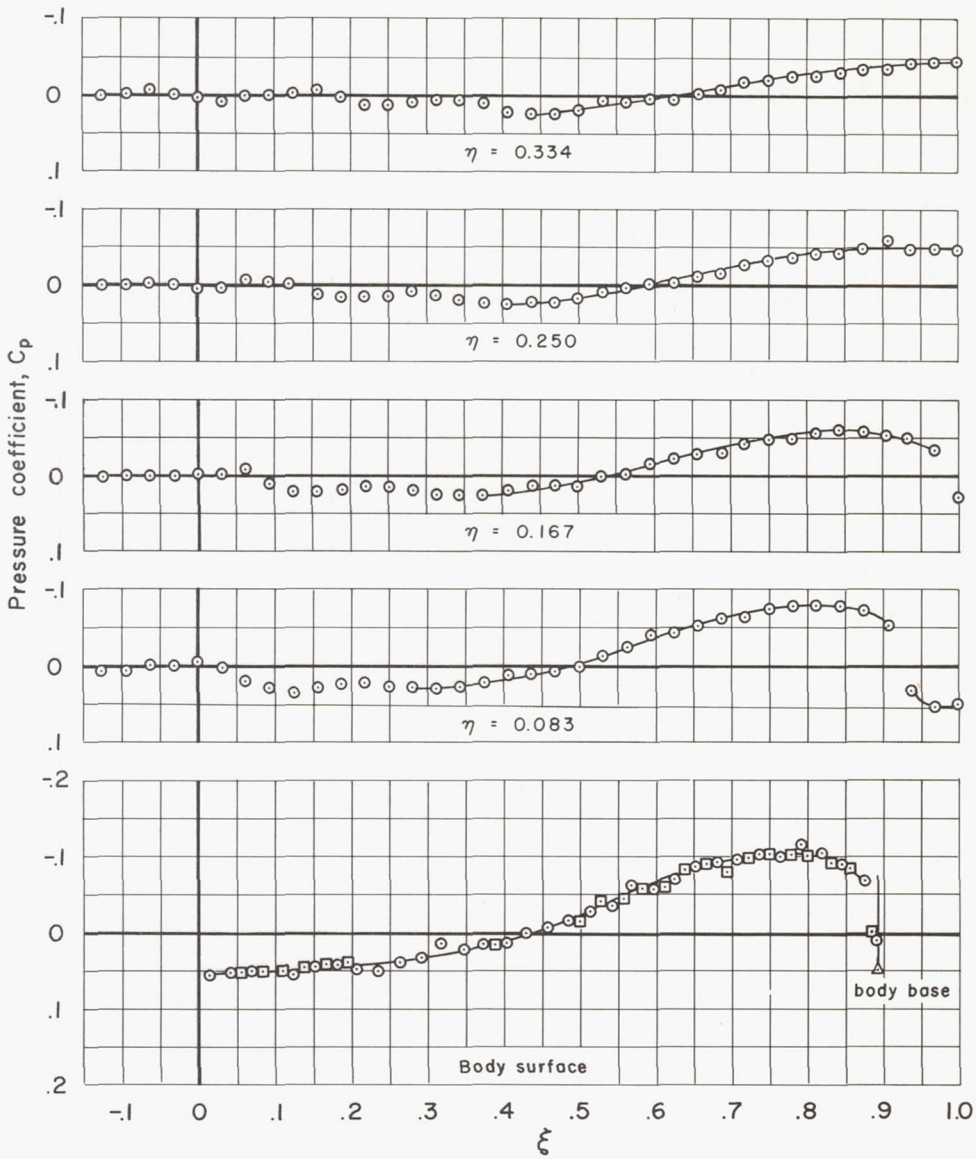

(l) M_∞ = 1.20, S_{max} at ξ = 0.60

Figure 10.- Concluded.

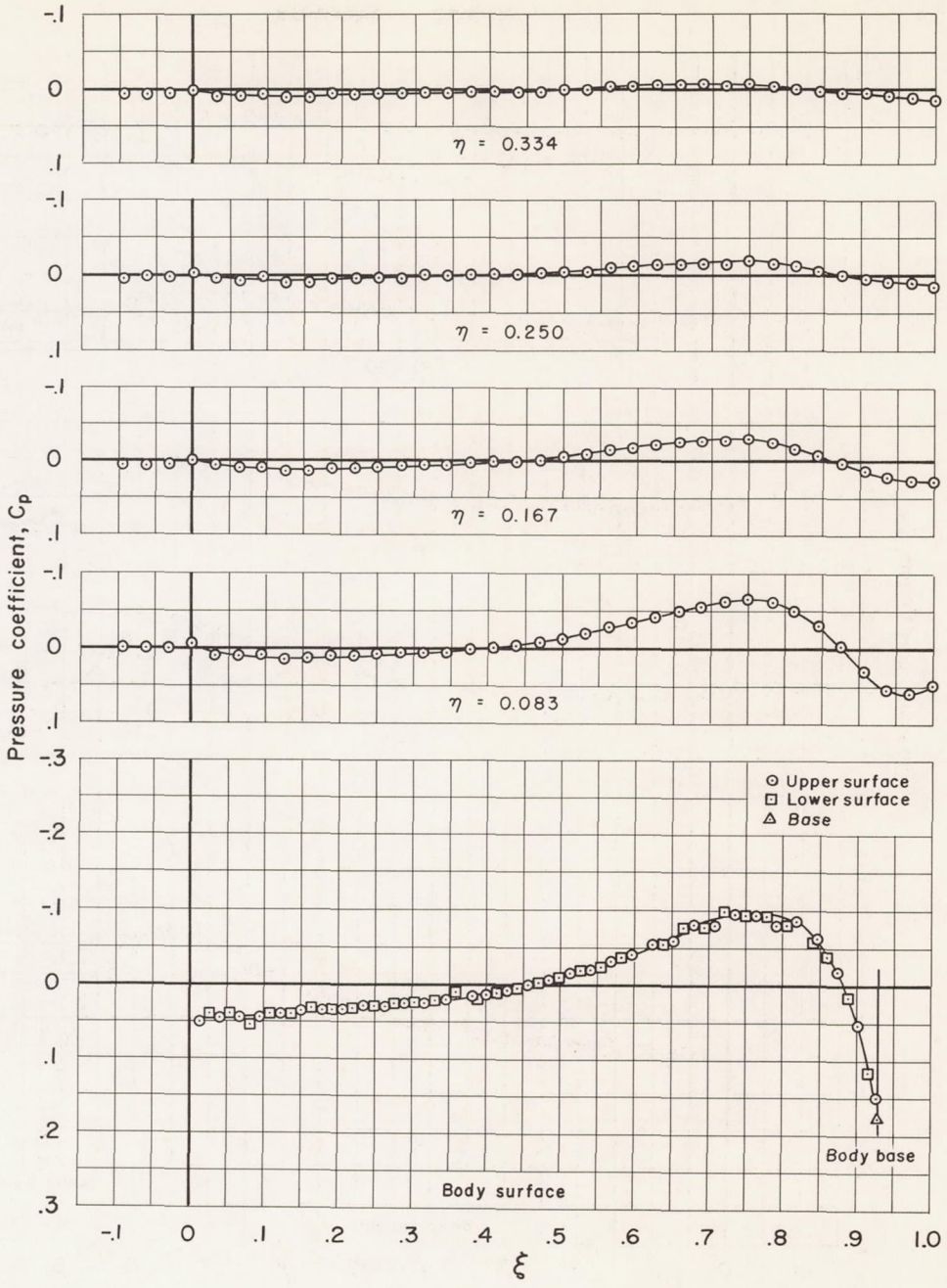

(a) $M_\infty = 0.80$, S_{max} at $\xi = 0.70$

Figure 11.- Experimental pressure distributions for the body with maximum cross-sectional area at $\xi = 0.70$.

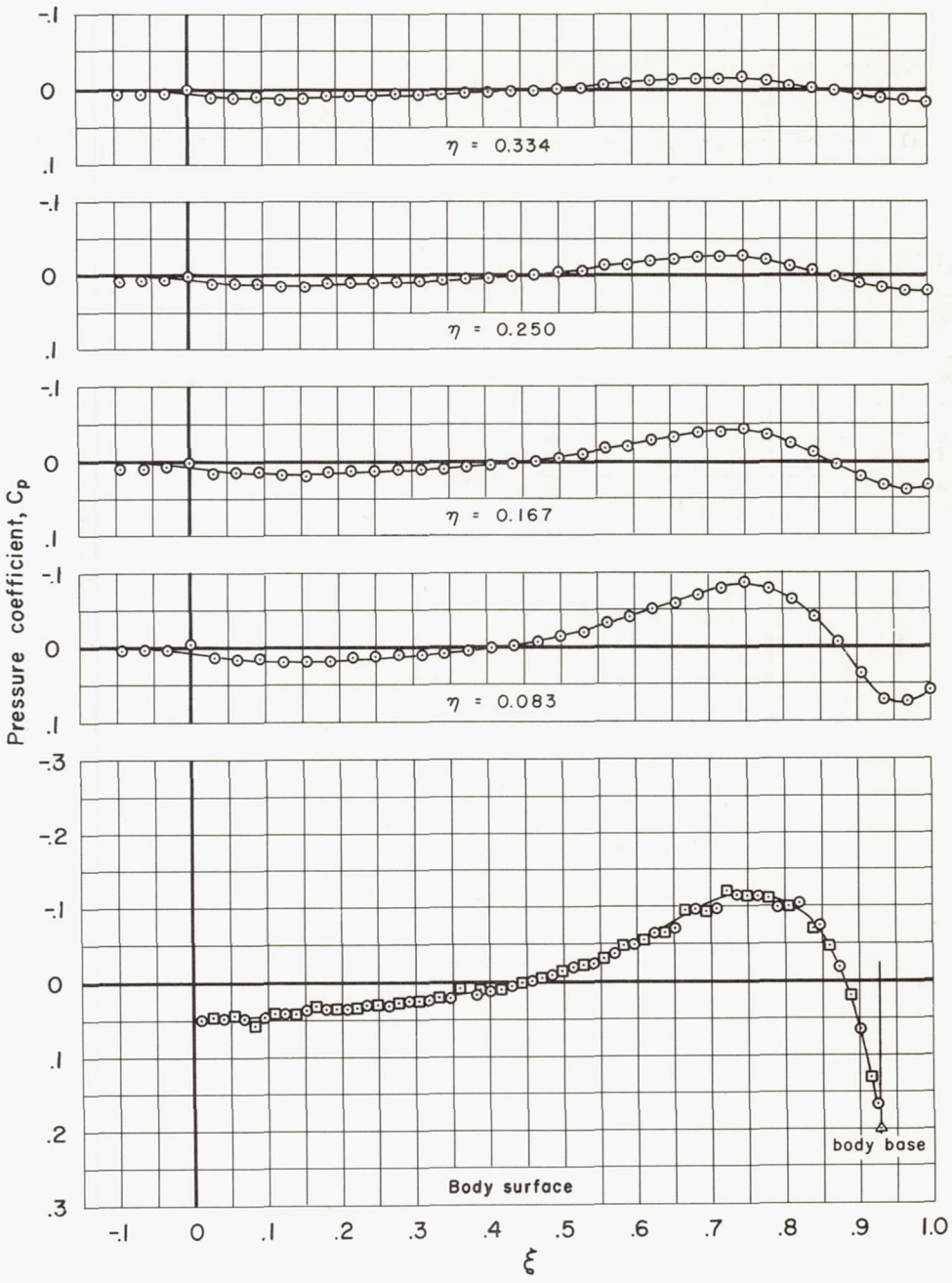

(b) $M_\infty = 0.90$, S_{max} at $\xi = 0.70$

Figure 11.- Continued.

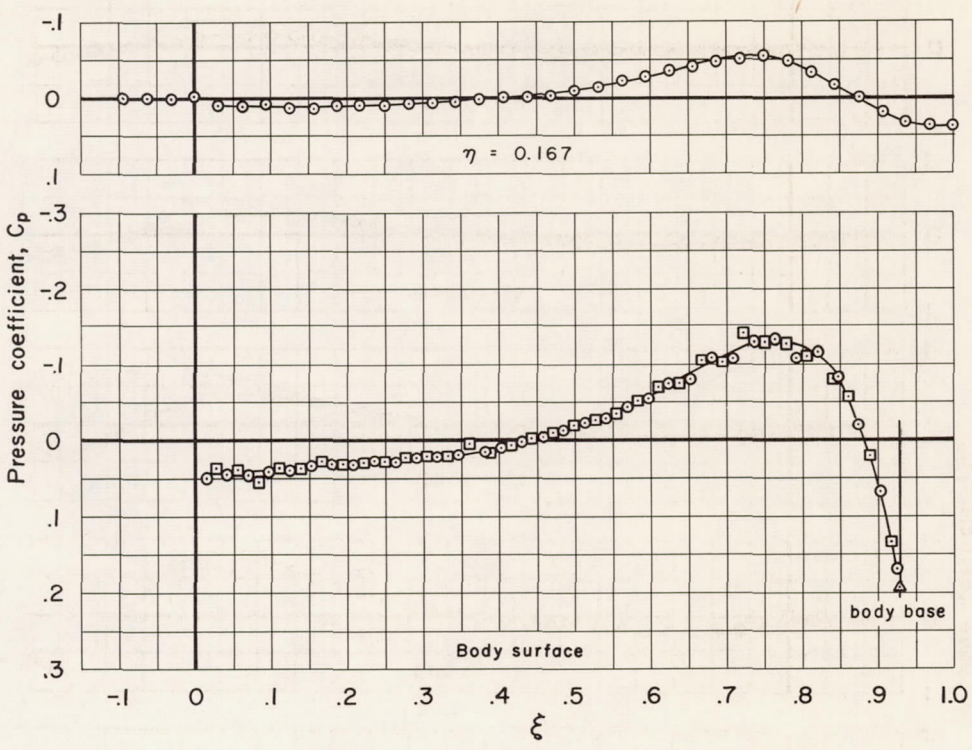

(c) $M_\infty = 0.925$, S_{max} at $\xi = 0.70$

Figure 11.- Continued.

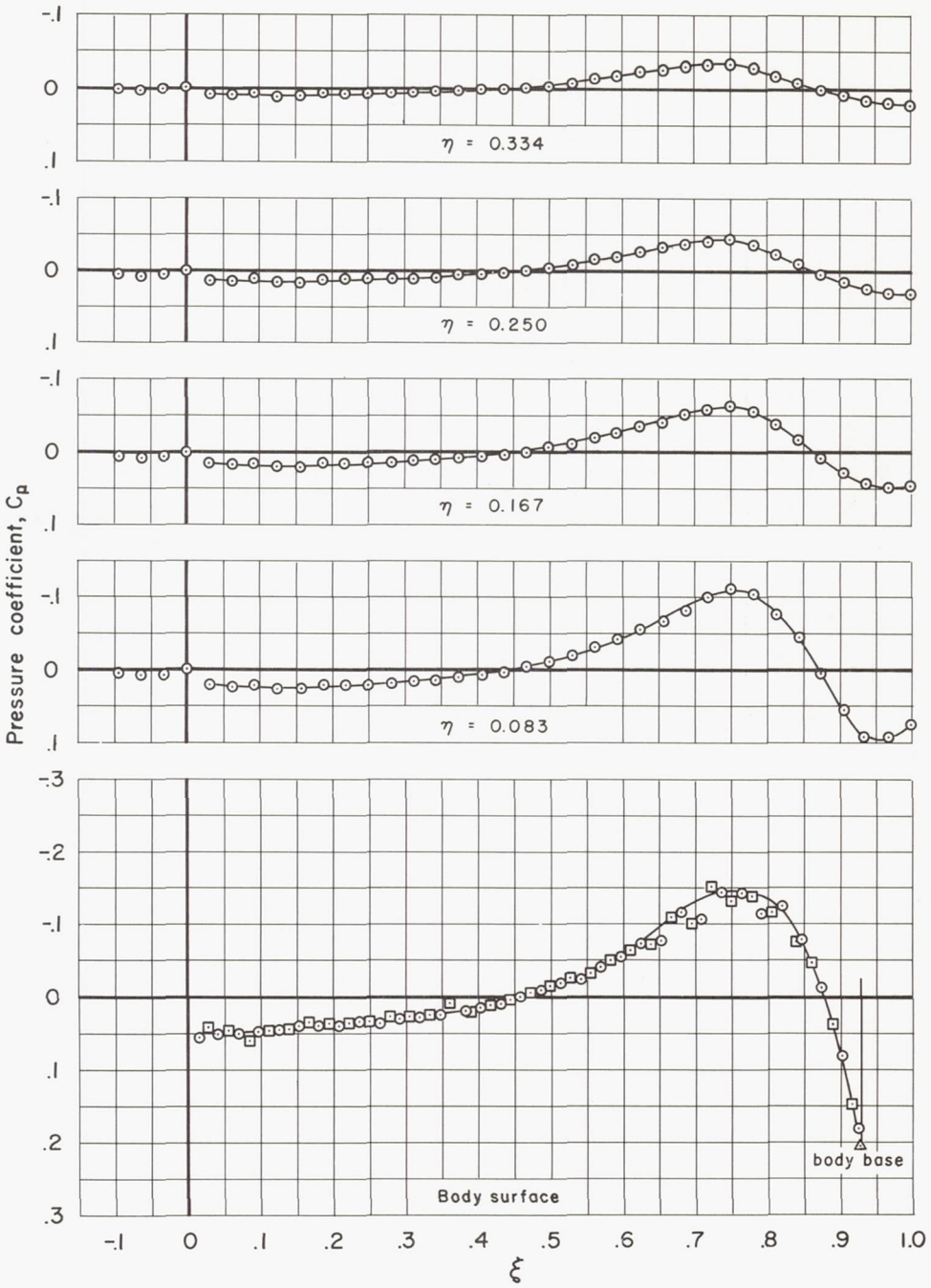

(d) $M_\infty = 0.95$, S_{max} at $\xi = 0.70$

Figure 11.- Continued.

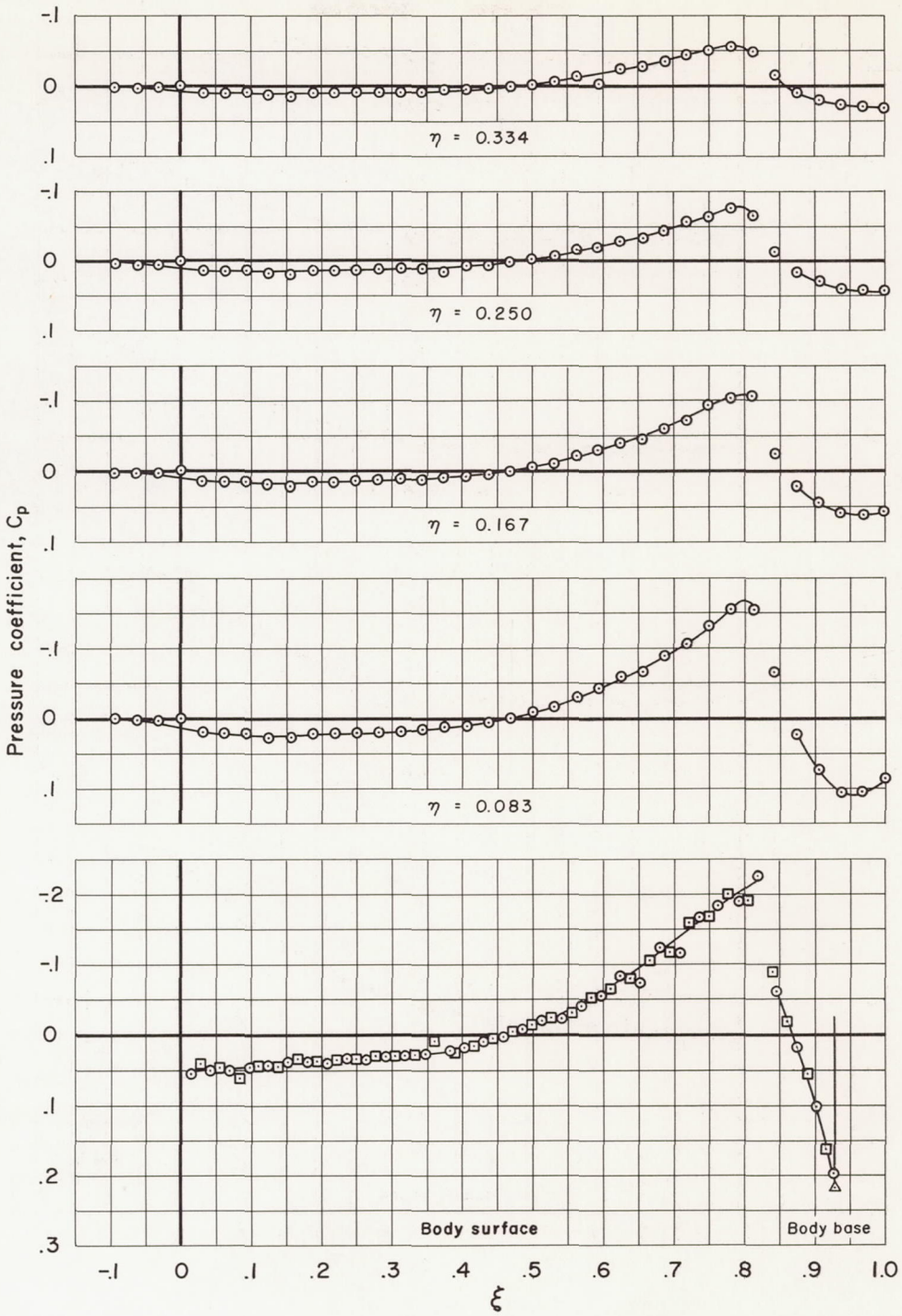

(e) M_∞ = 0.975, S_{max} at ξ = 0.70

Figure 11.- Continued.

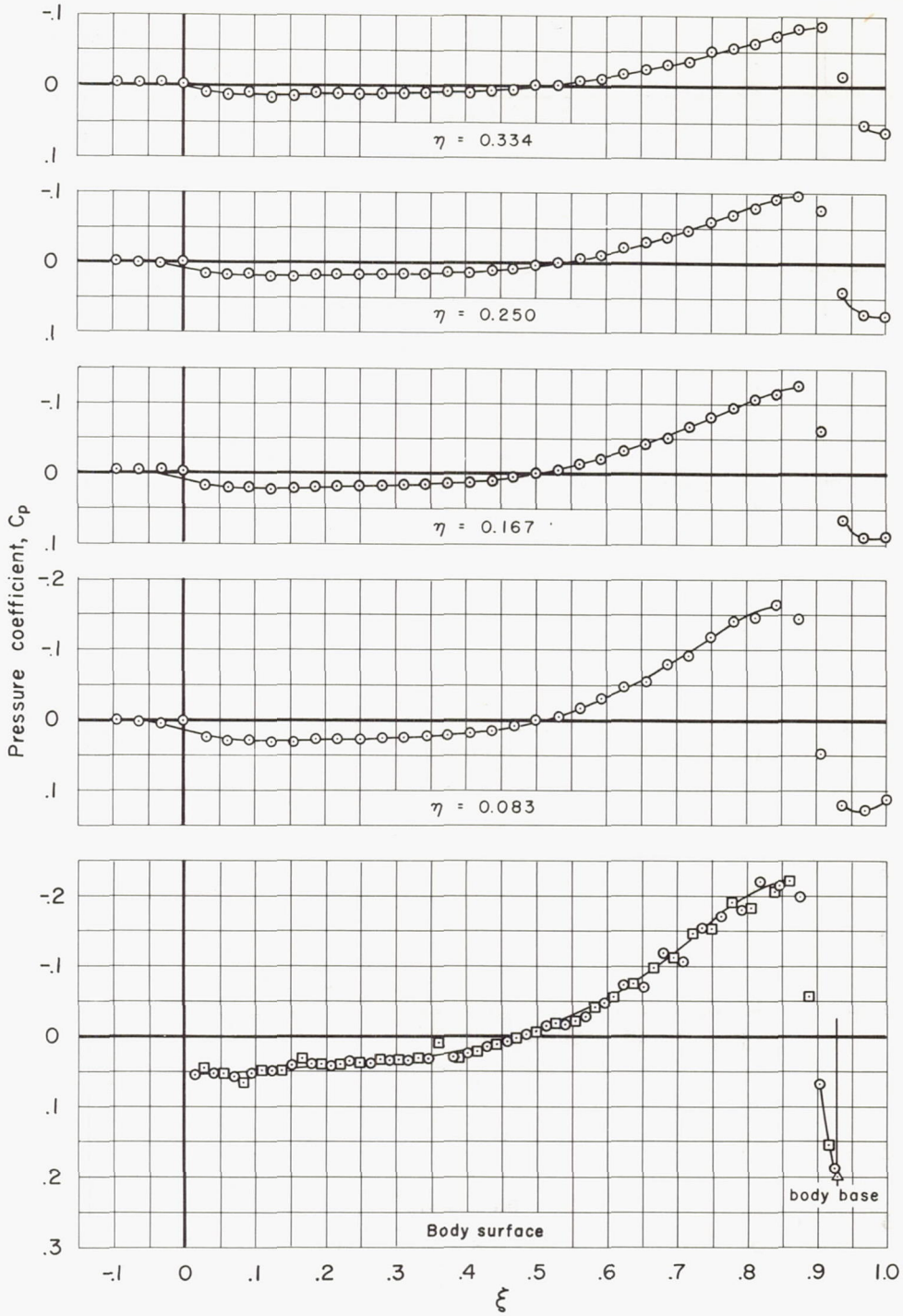

(f) M_∞ = 1.00, S_{max} at ξ = 0.70

Figure 11.- Continued.

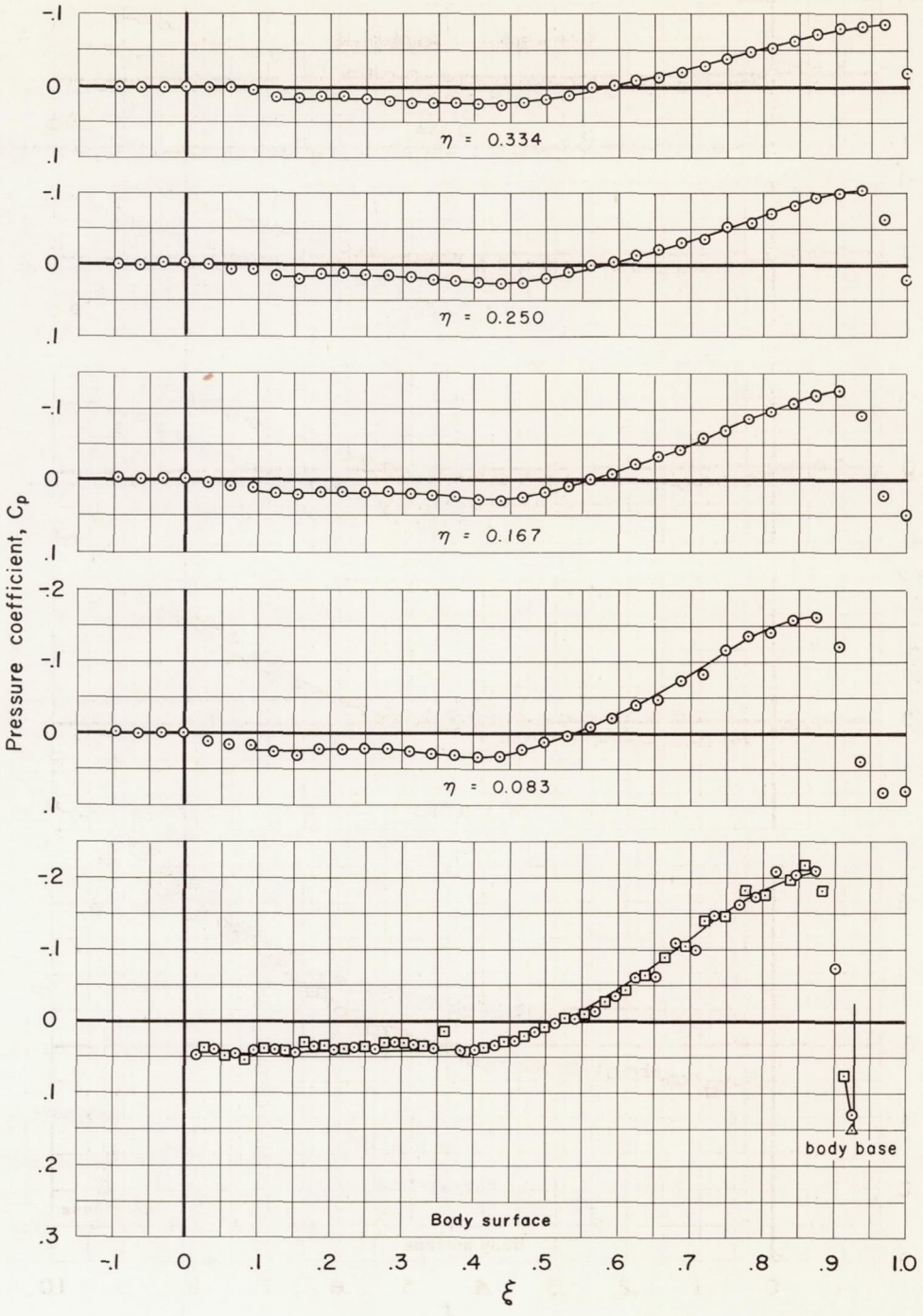

(g) M_∞ = 1.025, S_{max} at ξ = 0.70

Figure 11.- Continued.

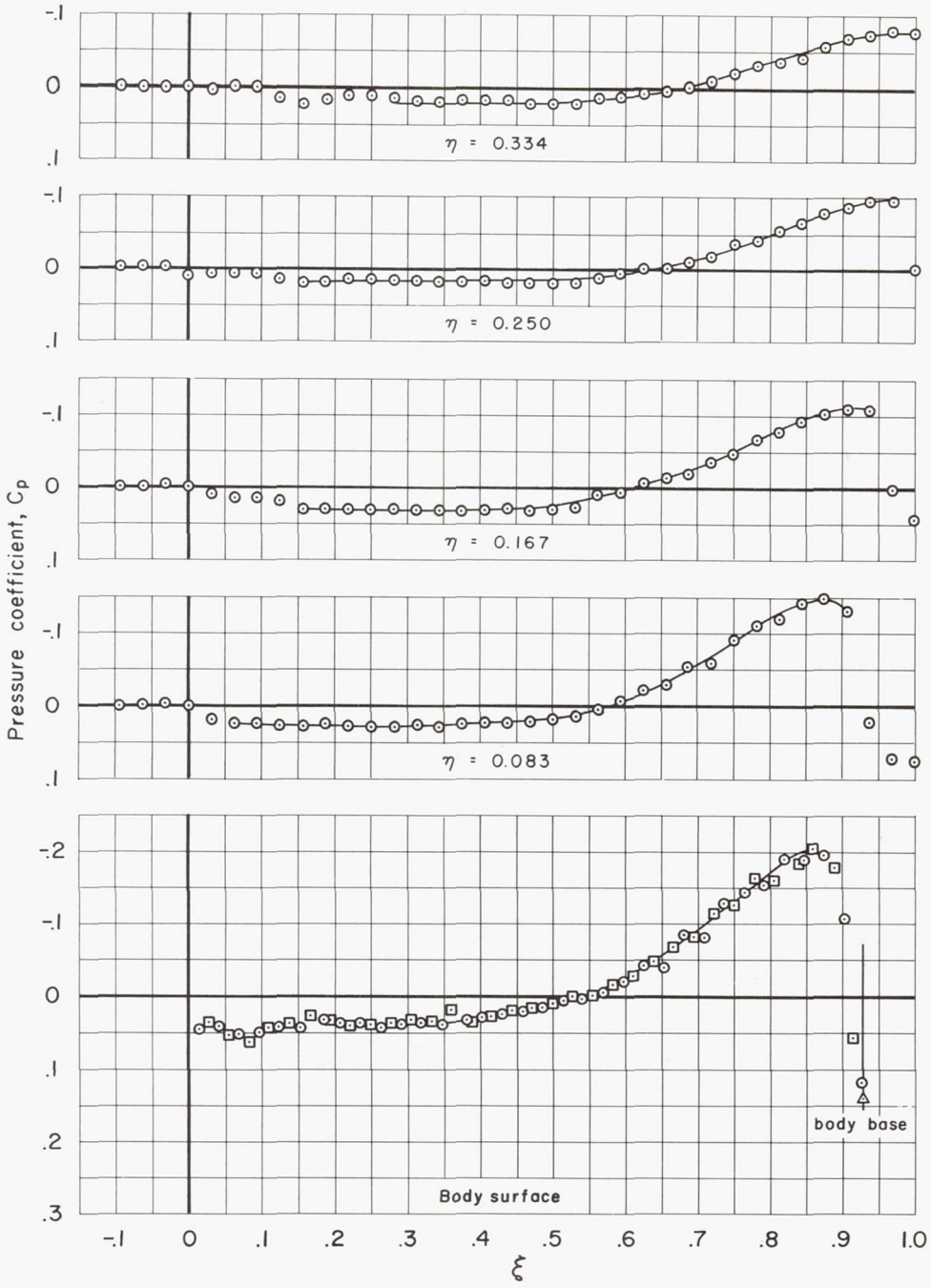

(h) M_∞ = 1.05, S_{max} at ξ = 0.70

Figure 11.- Continued.

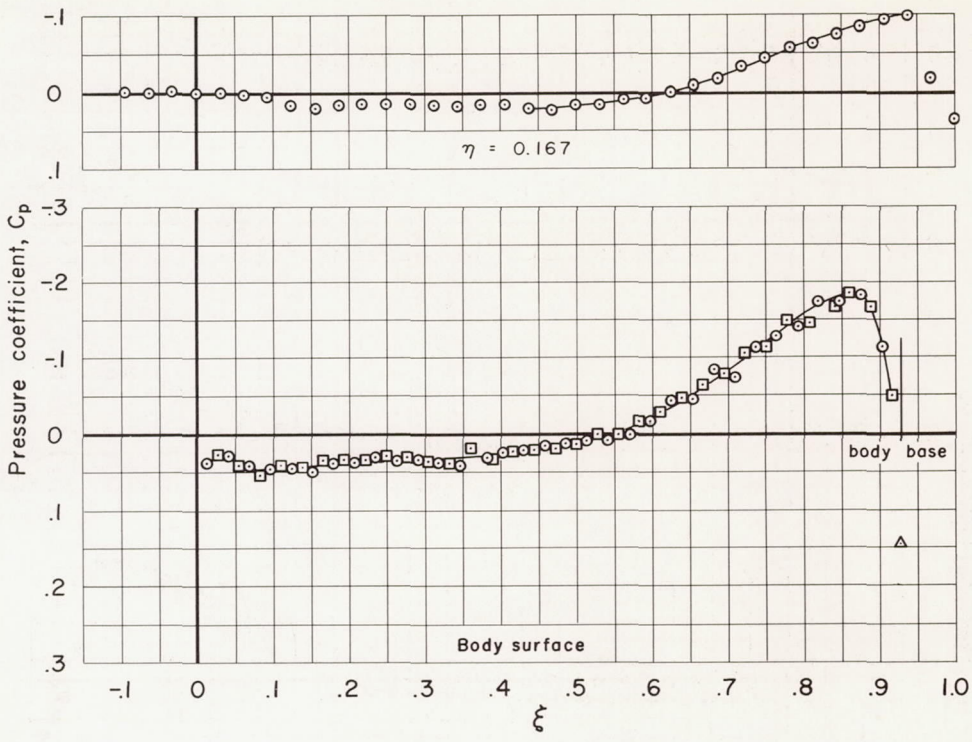

(i) $M_\infty = 1.075$, S_{max} at $\xi = 0.70$

Figure 11.- Continued.

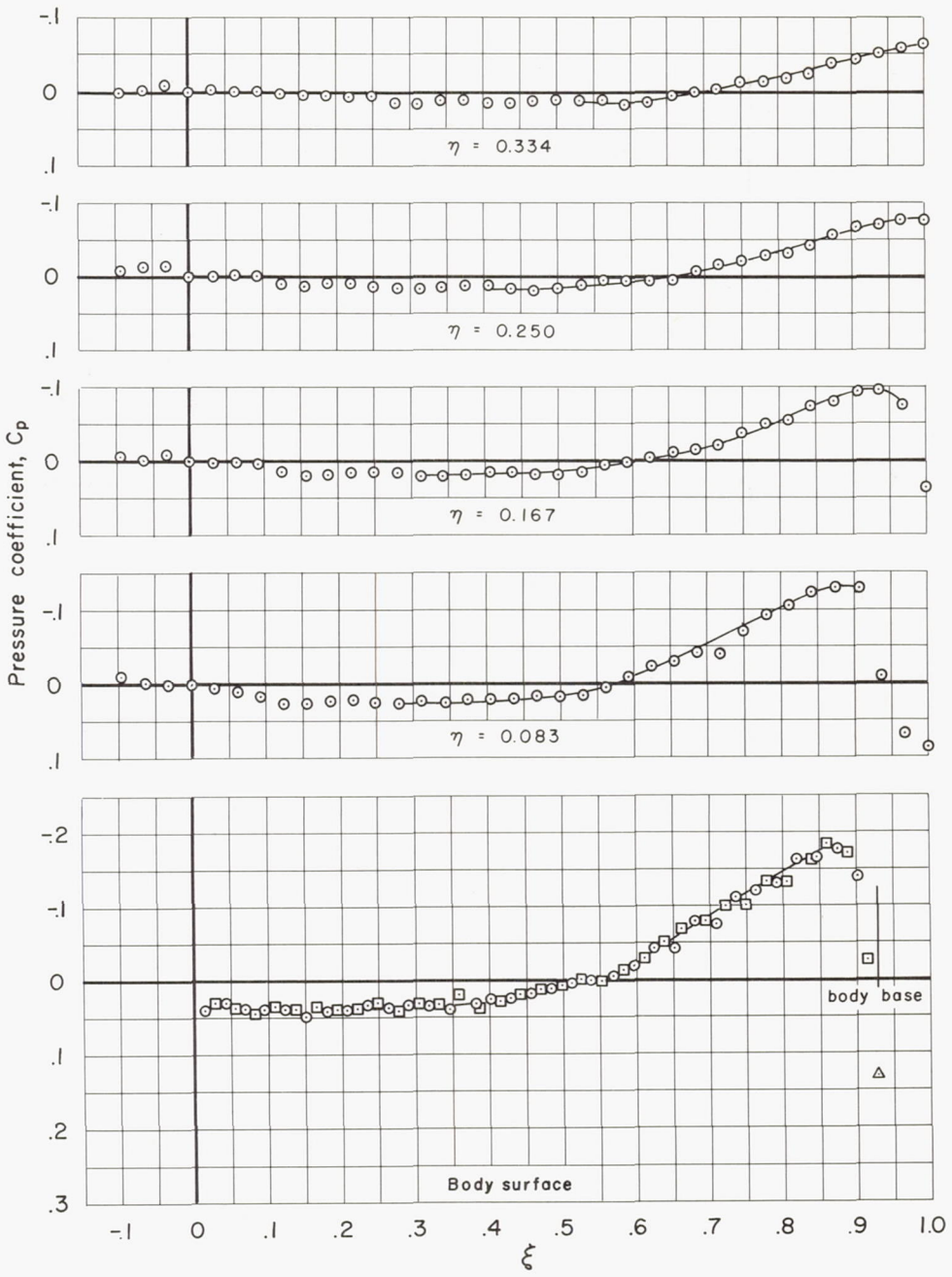

(j) M_∞ = 1.10, S_{max} at ξ = 0.70

Figure 11.- Continued.

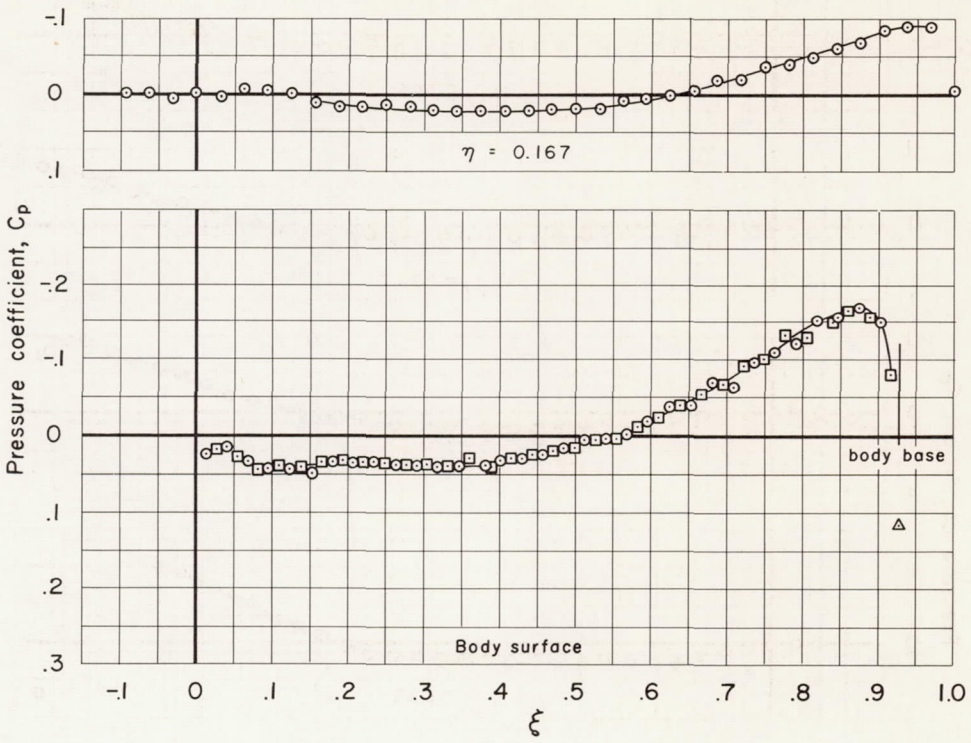

(k) $M_\infty = 1.15$, S_{max} at $\xi = 0.70$

Figure 11.- Continued.

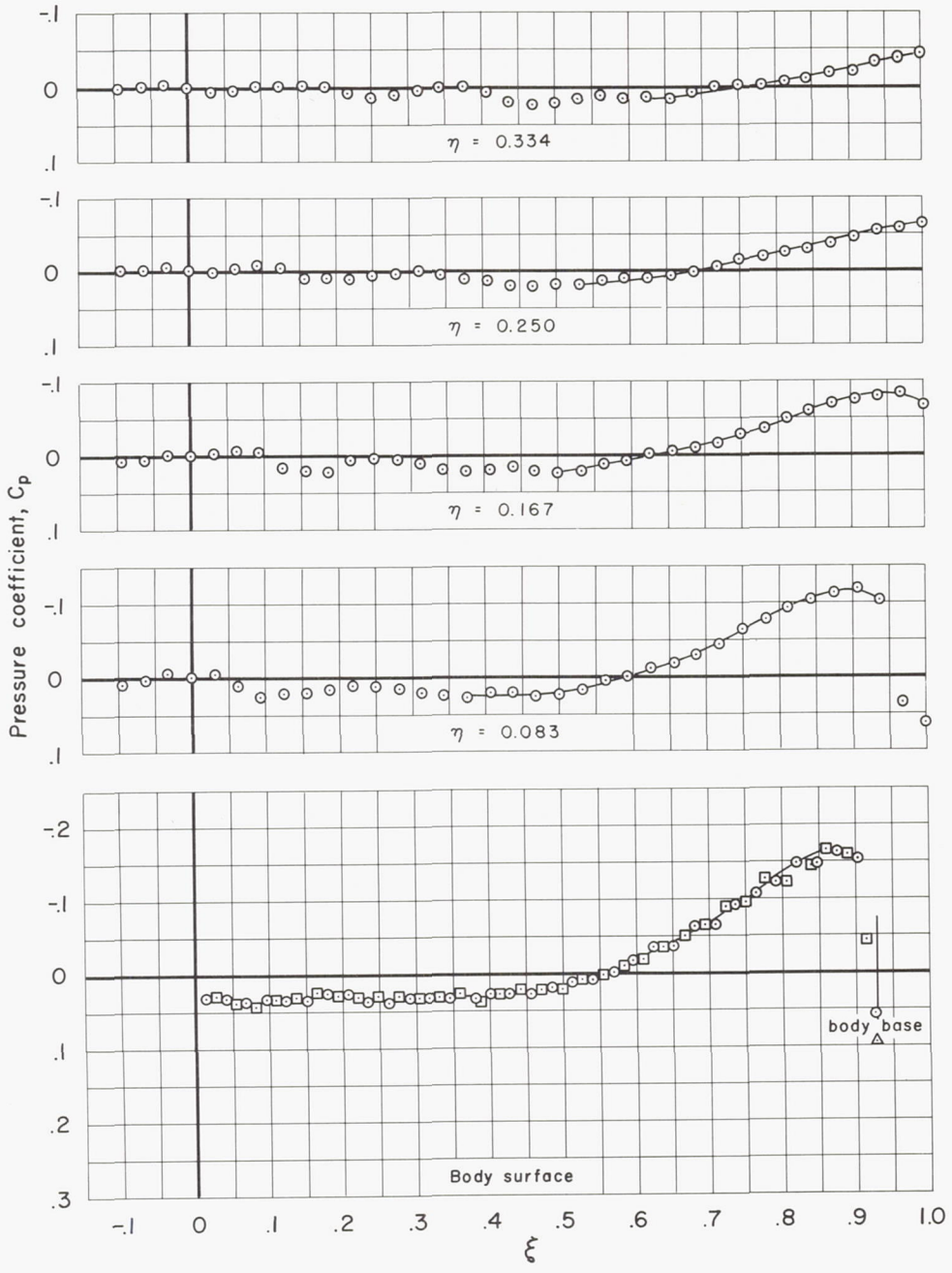

(l) M_∞ = 1.20, S_{max} at ξ = 0.70

Figure 11.- Concluded.

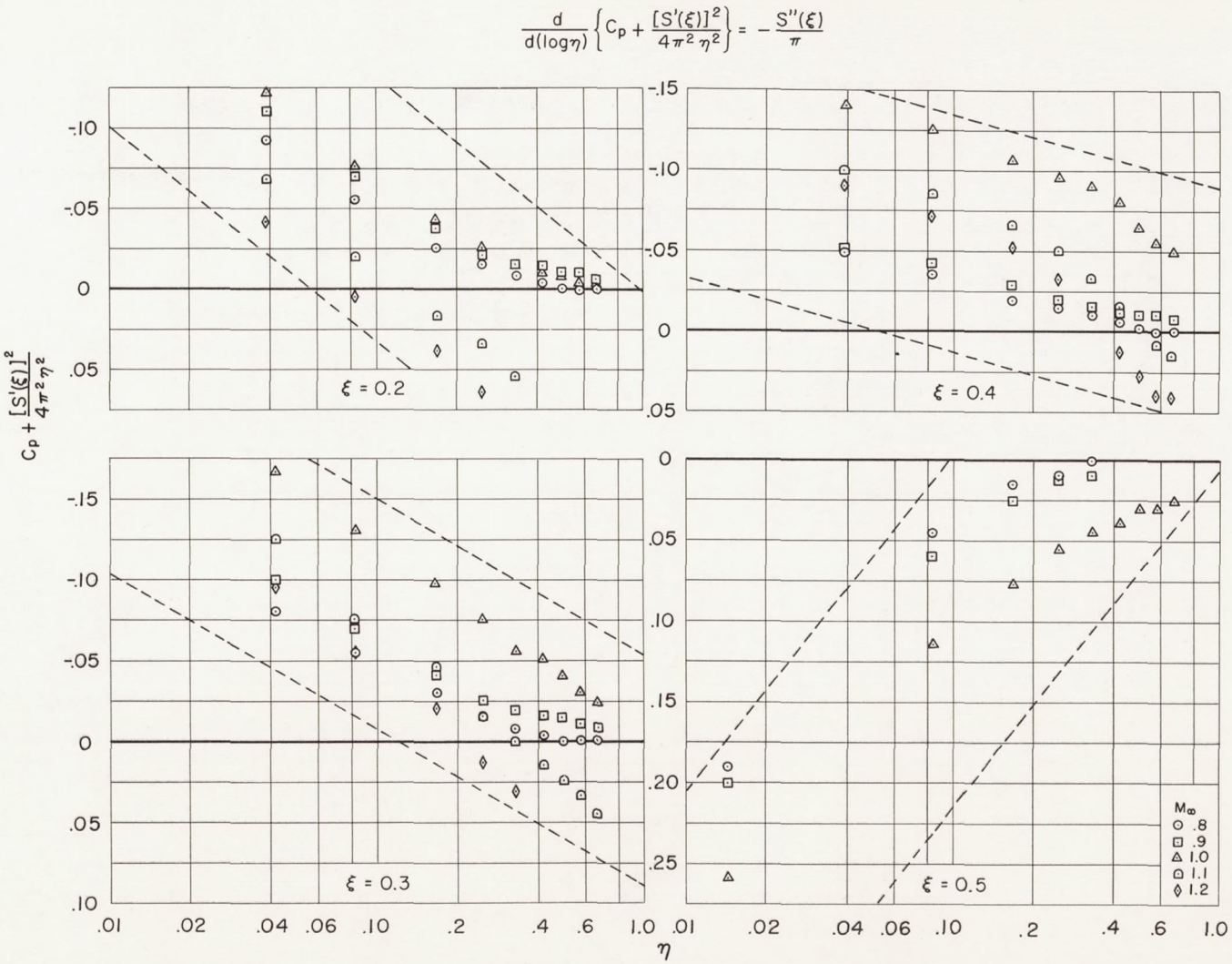

Figure 12.- Attenuation of static-pressure coefficient with radial distance for the body with maximum cross-sectional area at $\xi = 0.3$.

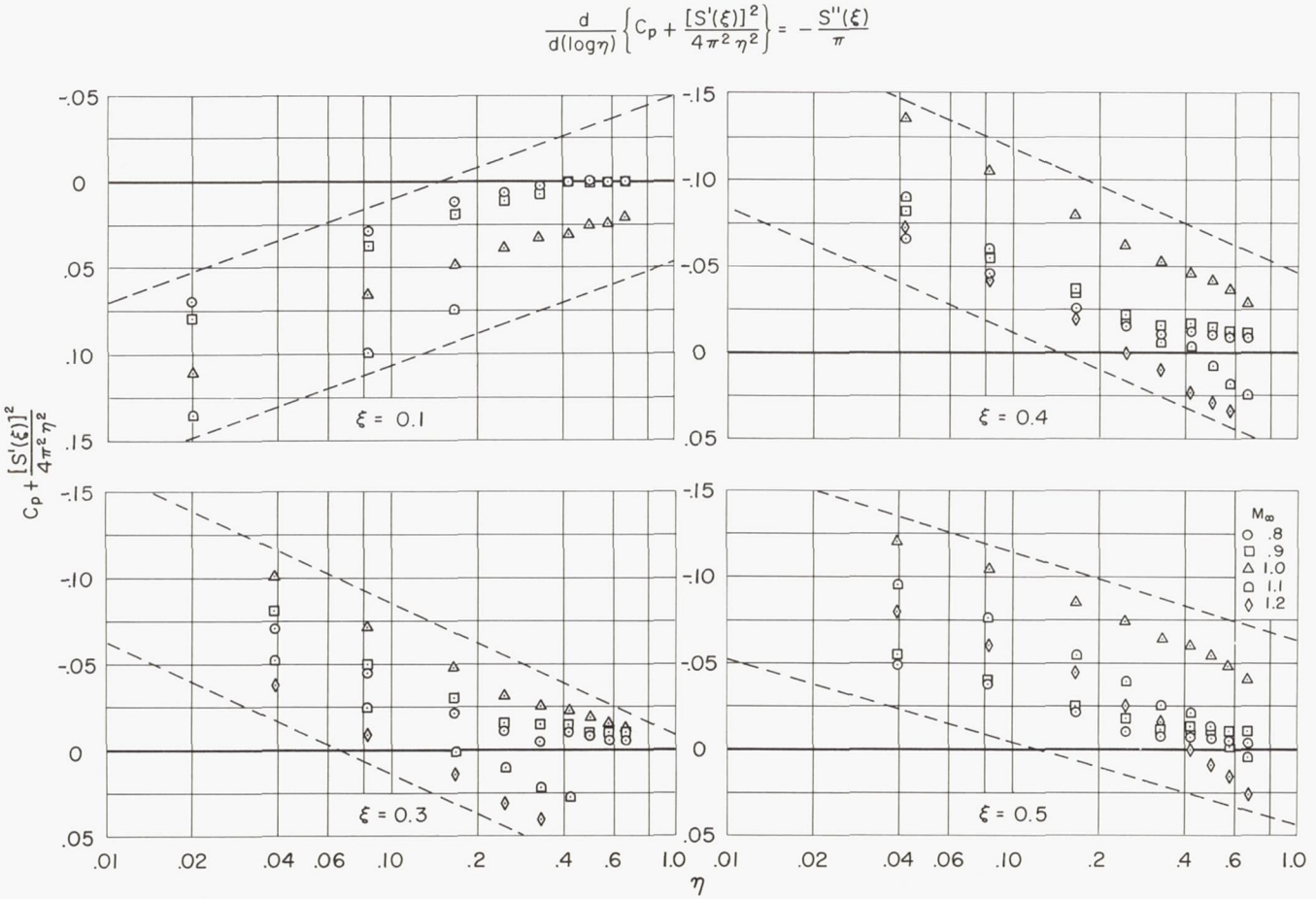

Figure 13.- Attenuation of static-pressure coefficient with radial distance for the body with maximum cross-sectional area at $\xi = 0.4$.

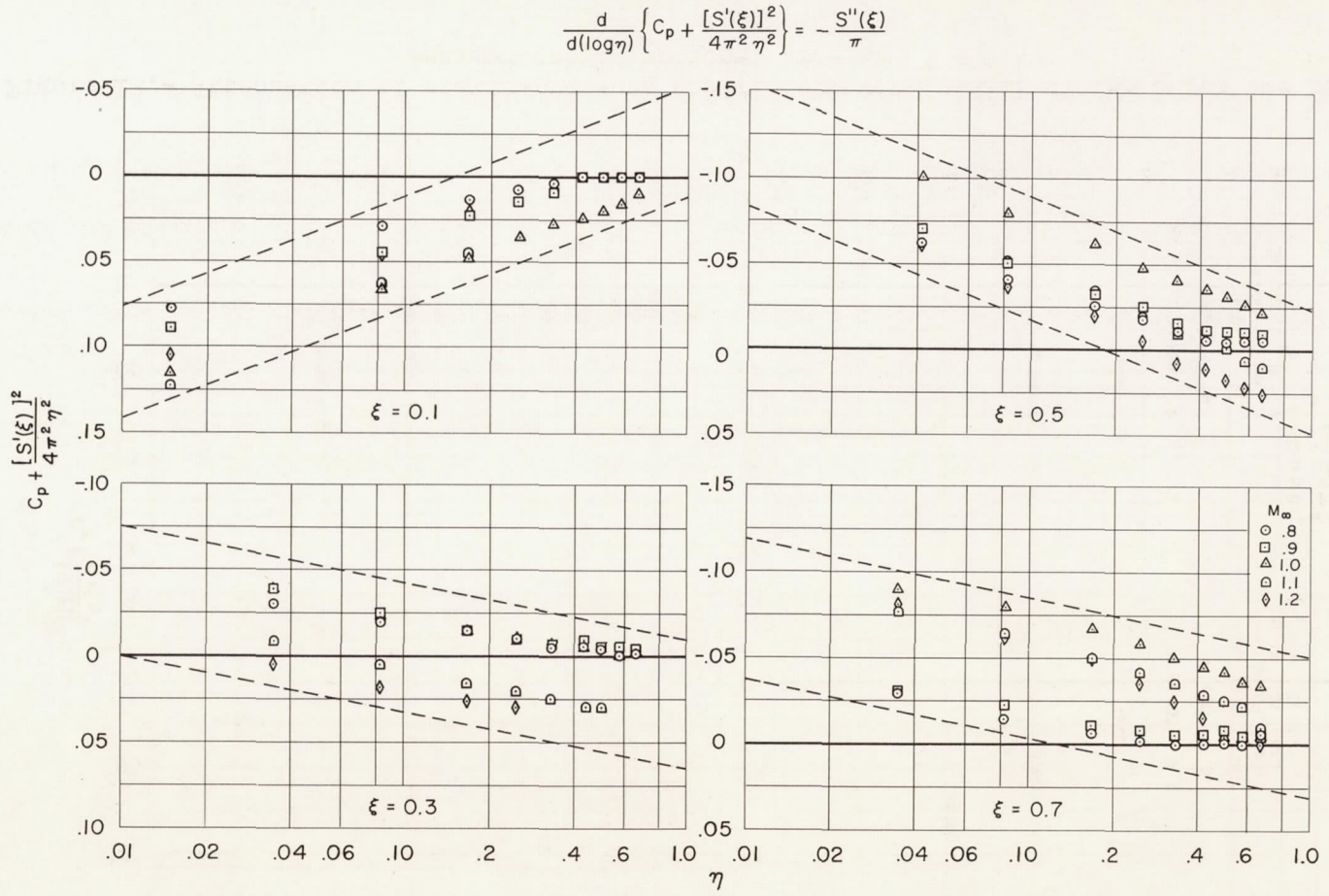

Figure 14.- Attenuation of static-pressure coefficient with radial distance for the body with maximum cross-sectional area at $\xi = 0.5$.

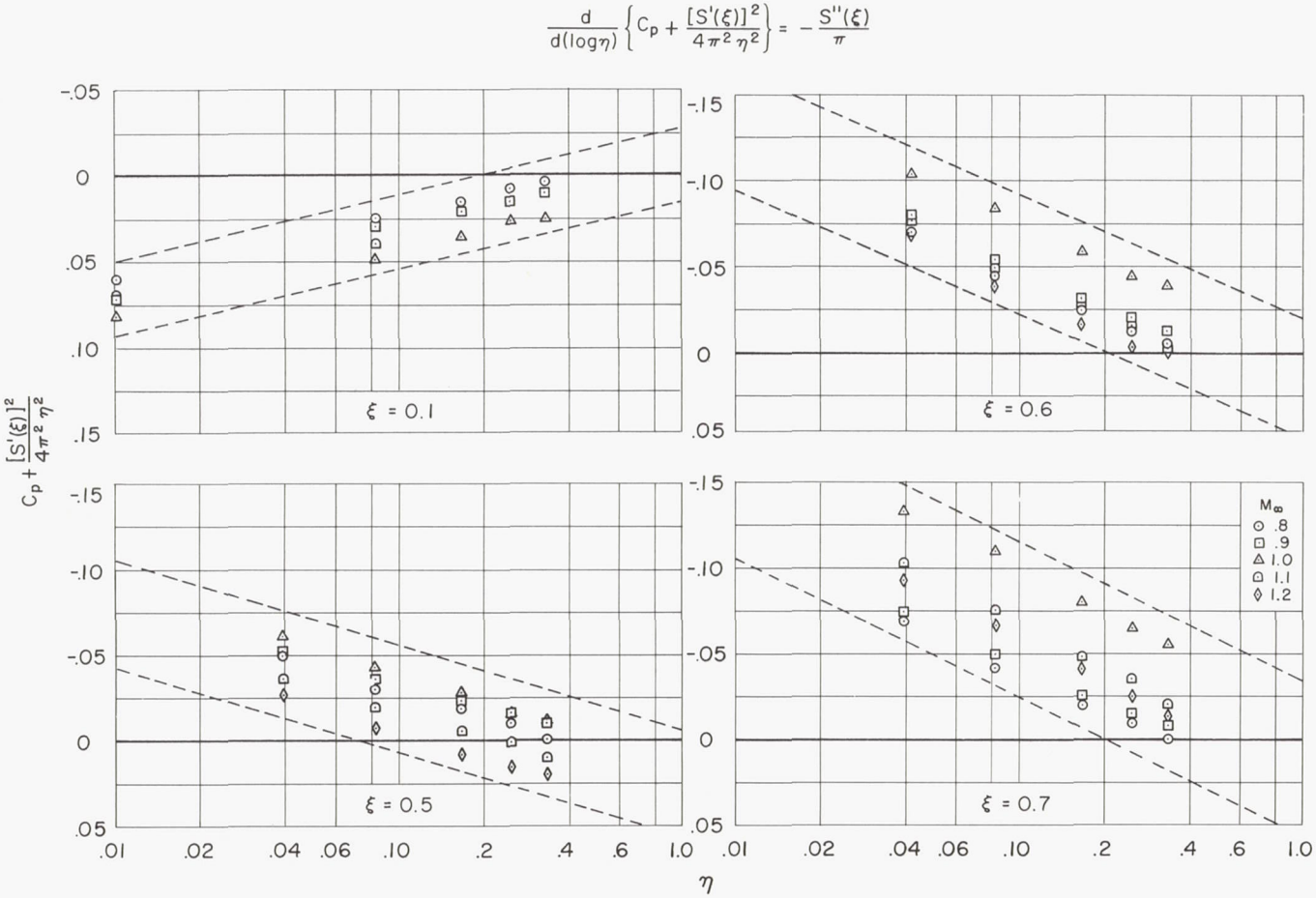

Figure 15.- Attenuation of static-pressure coefficient with radial distance for the body with maximum cross-sectional area at $\xi = 0.6$.

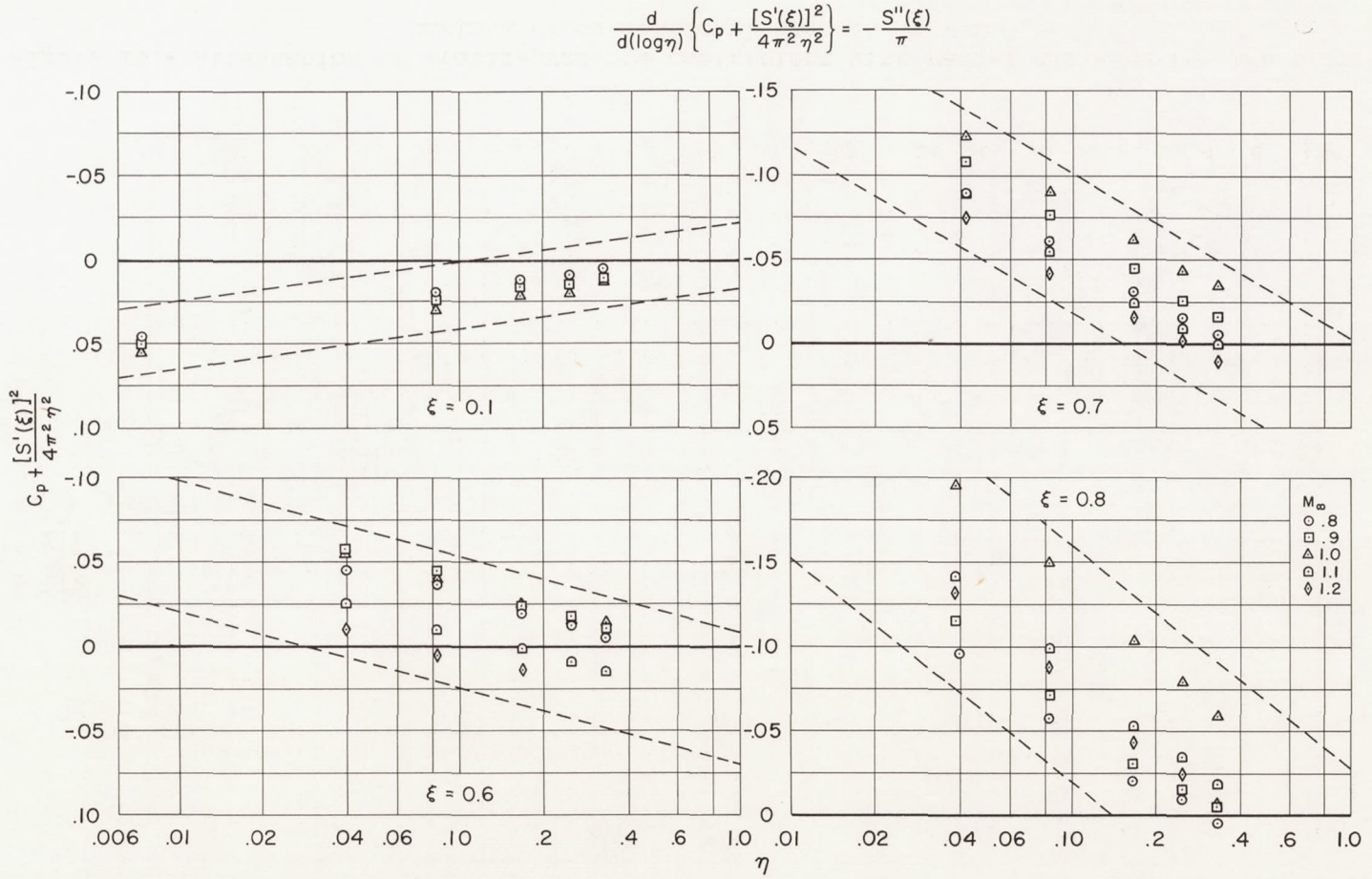

Figure 16.- Attenuation of static-pressure coefficient with radial distance for the body with maximum cross-sectional area at $\xi = 0.7$.

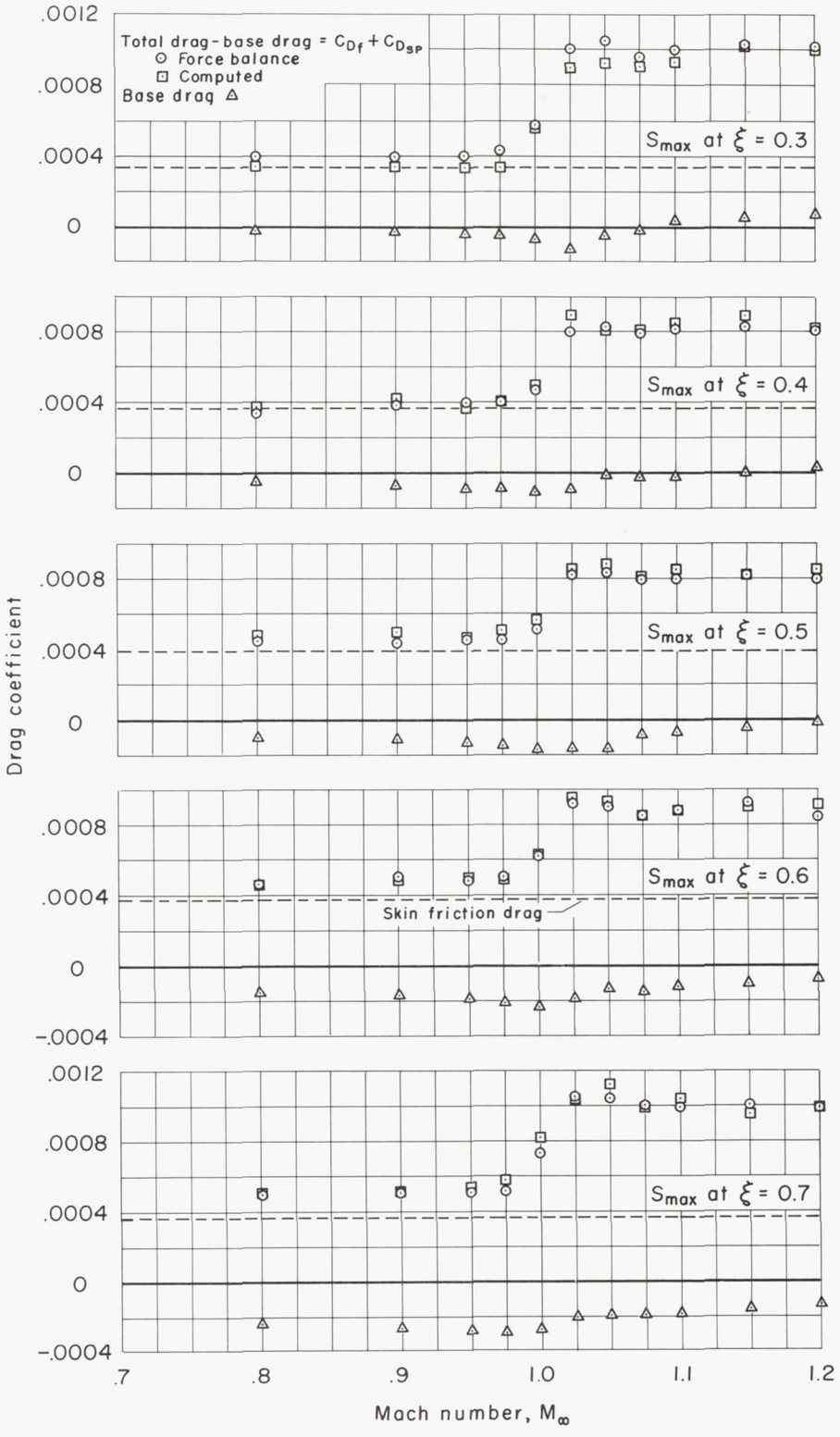

Figure 17.- Zero-lift drag coefficients.

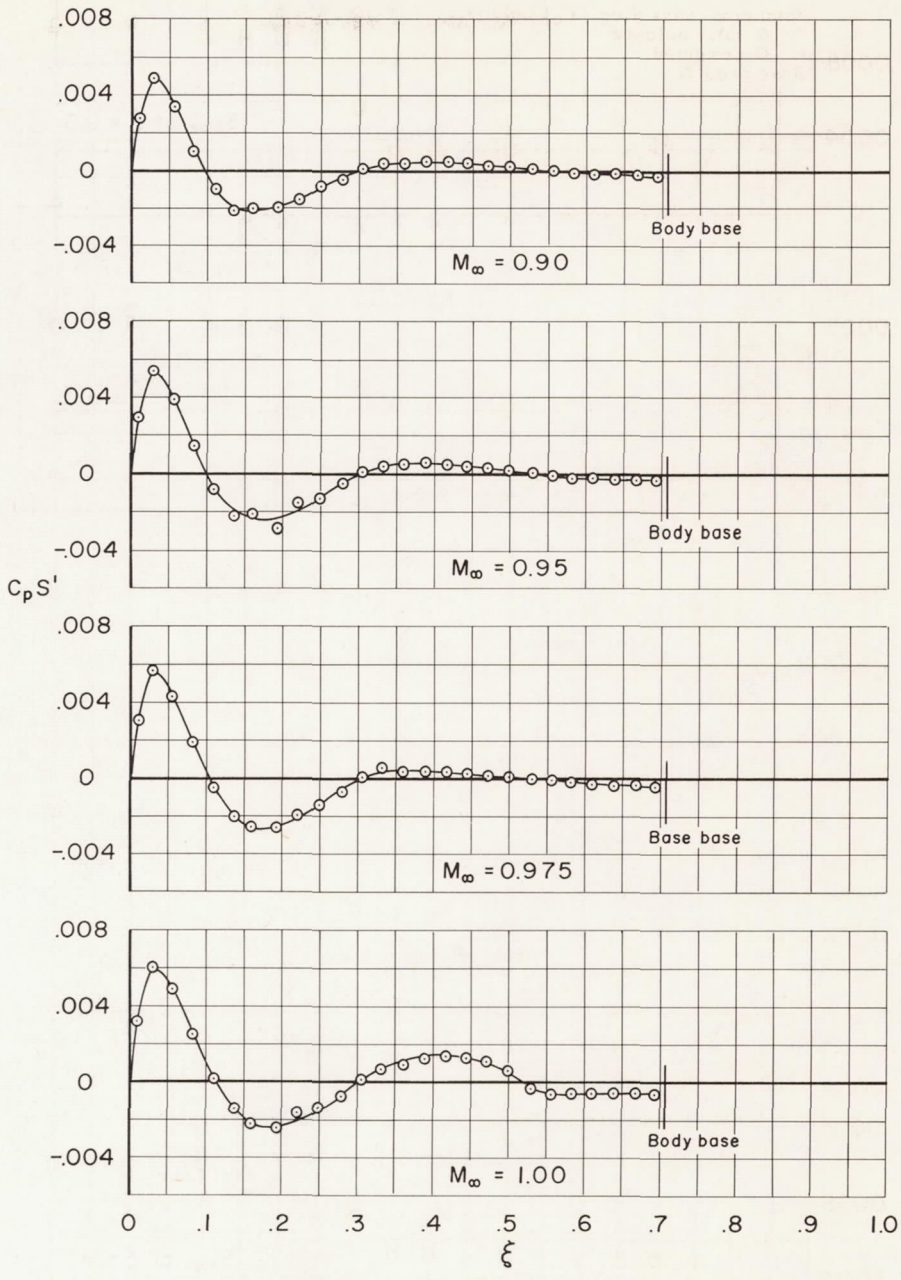

(a) M_∞ = 0.90, 0.95, 0.975, and 1.00

Figure 18.- The variation of C_pS' with ξ for the body with maximum cross-sectional area at $\xi = 0.3$.

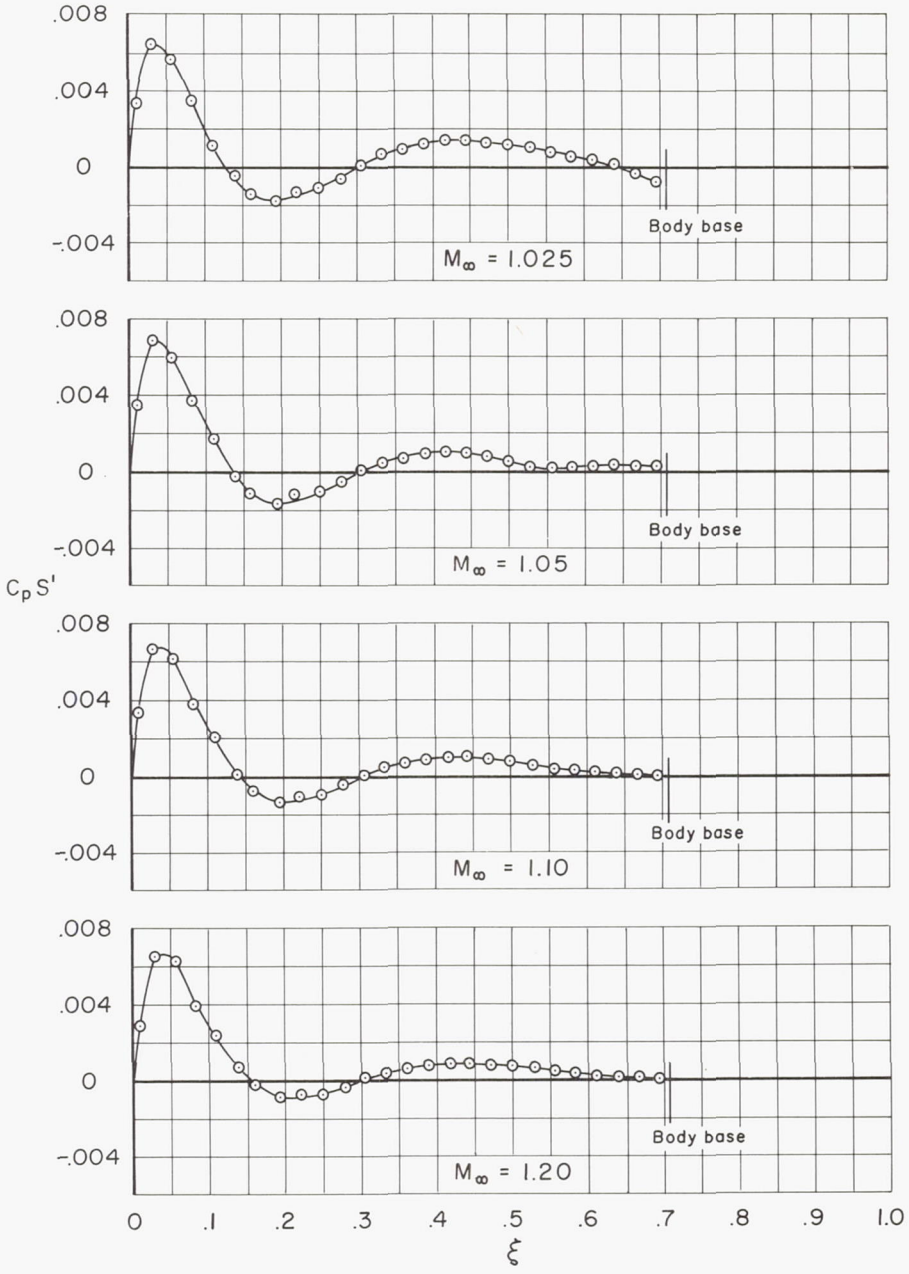

(b) M_∞ = 1.025, 1.05, 1.10, and 1.20

Figure 18.- Concluded.

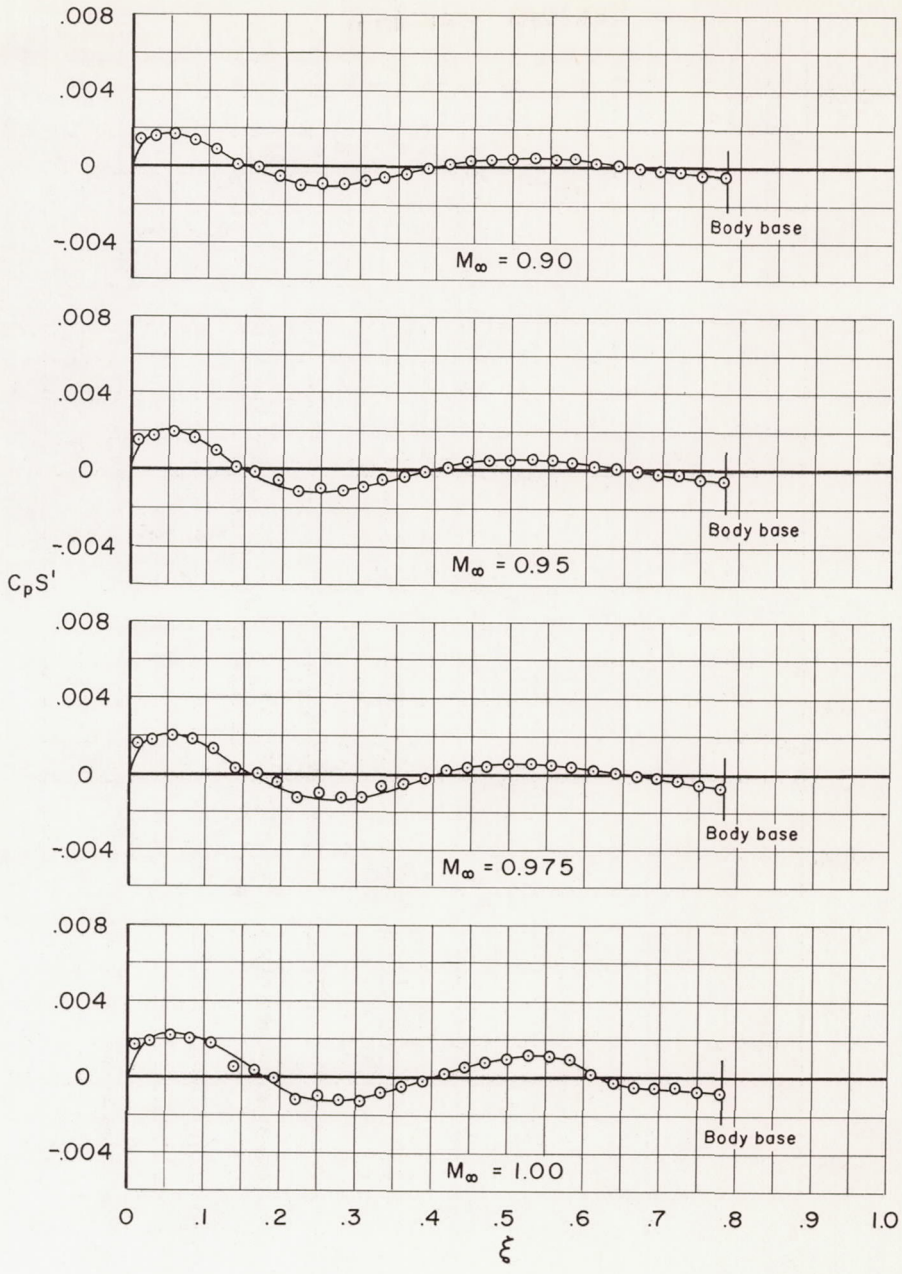

(a) M_∞ = 0.90, 0.95, 0.975, and 1.00

Figure 19.- The variation of C_pS' with ξ for the body with maximum cross-sectional area at ξ = 0.4.

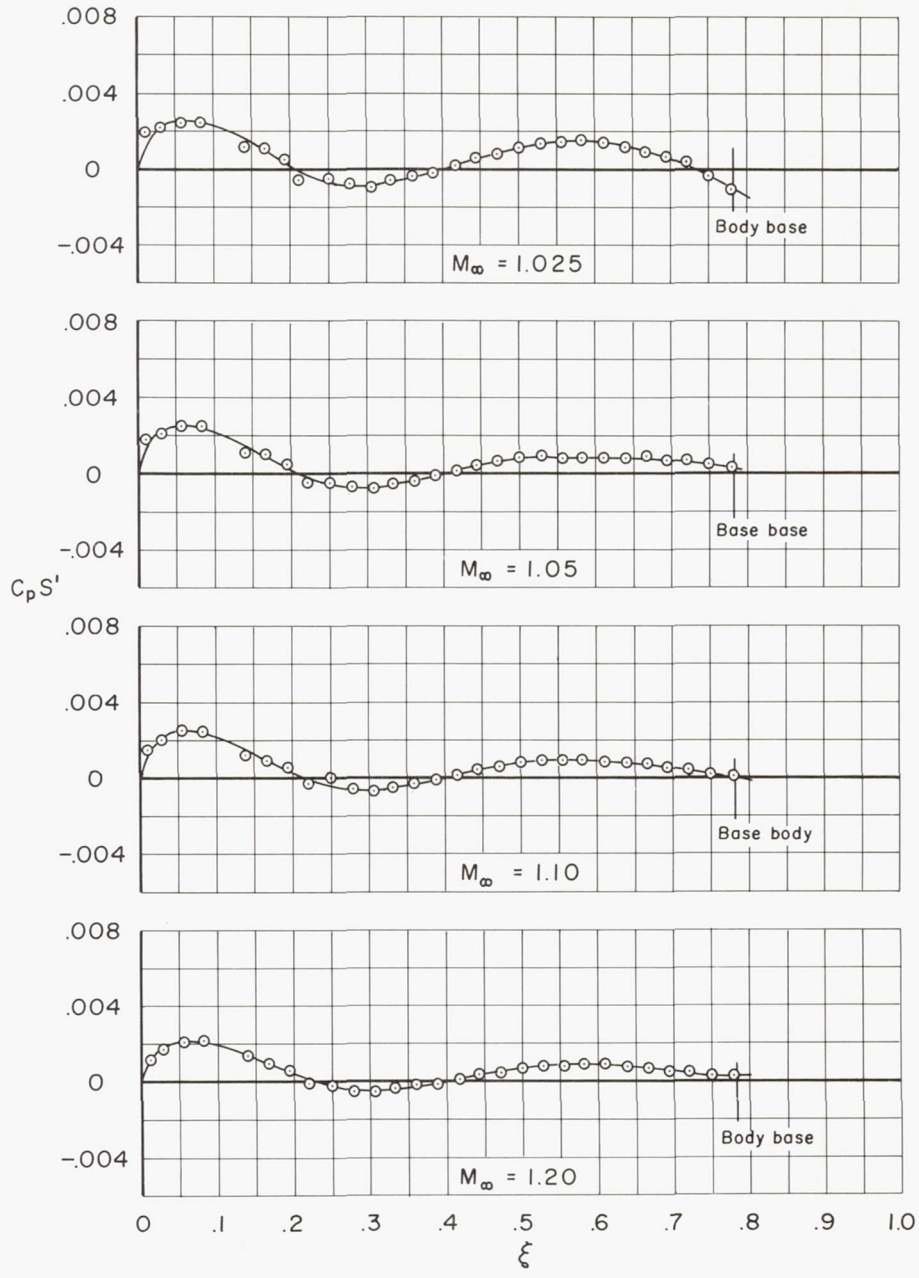

(b) M_∞ = 1.025, 1.05, 1.10, and 1.20

Figure 19.- Concluded.

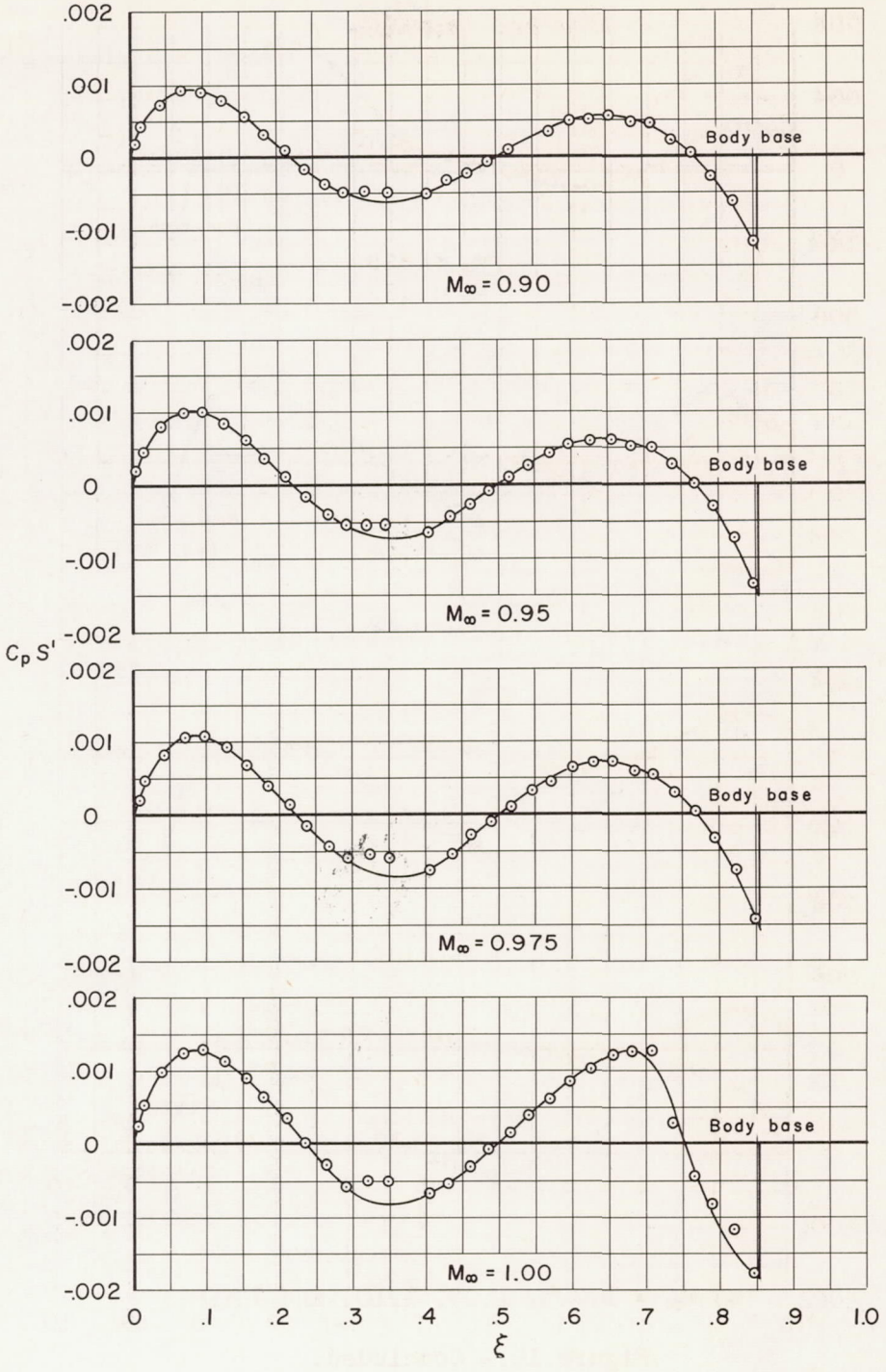

(a) M_∞ = 0.90, 0.95, 0.975, and 1.00

Figure 20.- The variation of C_pS' with ξ for the body with maximum cross-sectional area at $\xi = 0.5$.

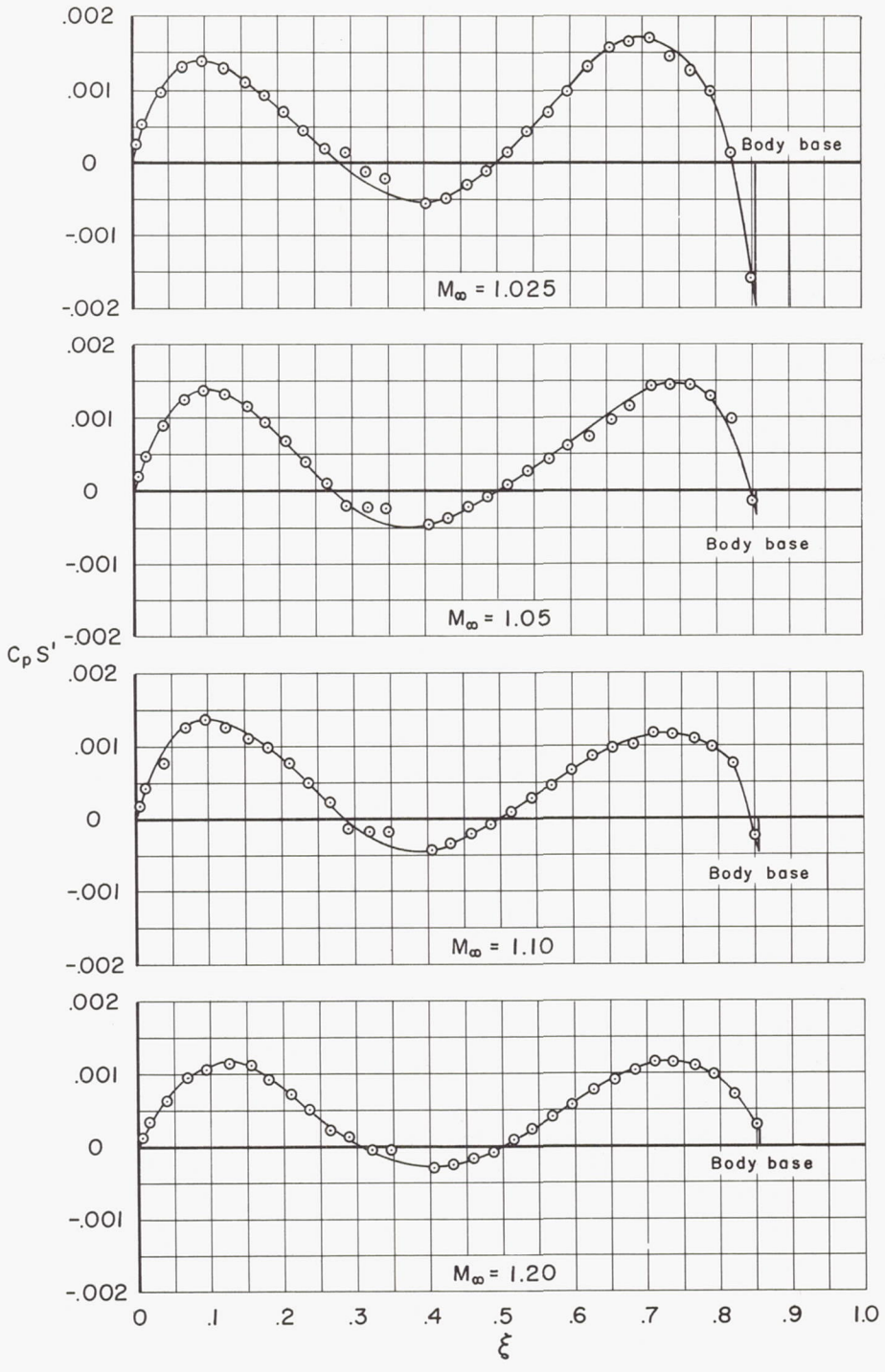

(b) M_∞ = 1.025, 1.05, 1.10, and 1.20

Figure 20.- Concluded.

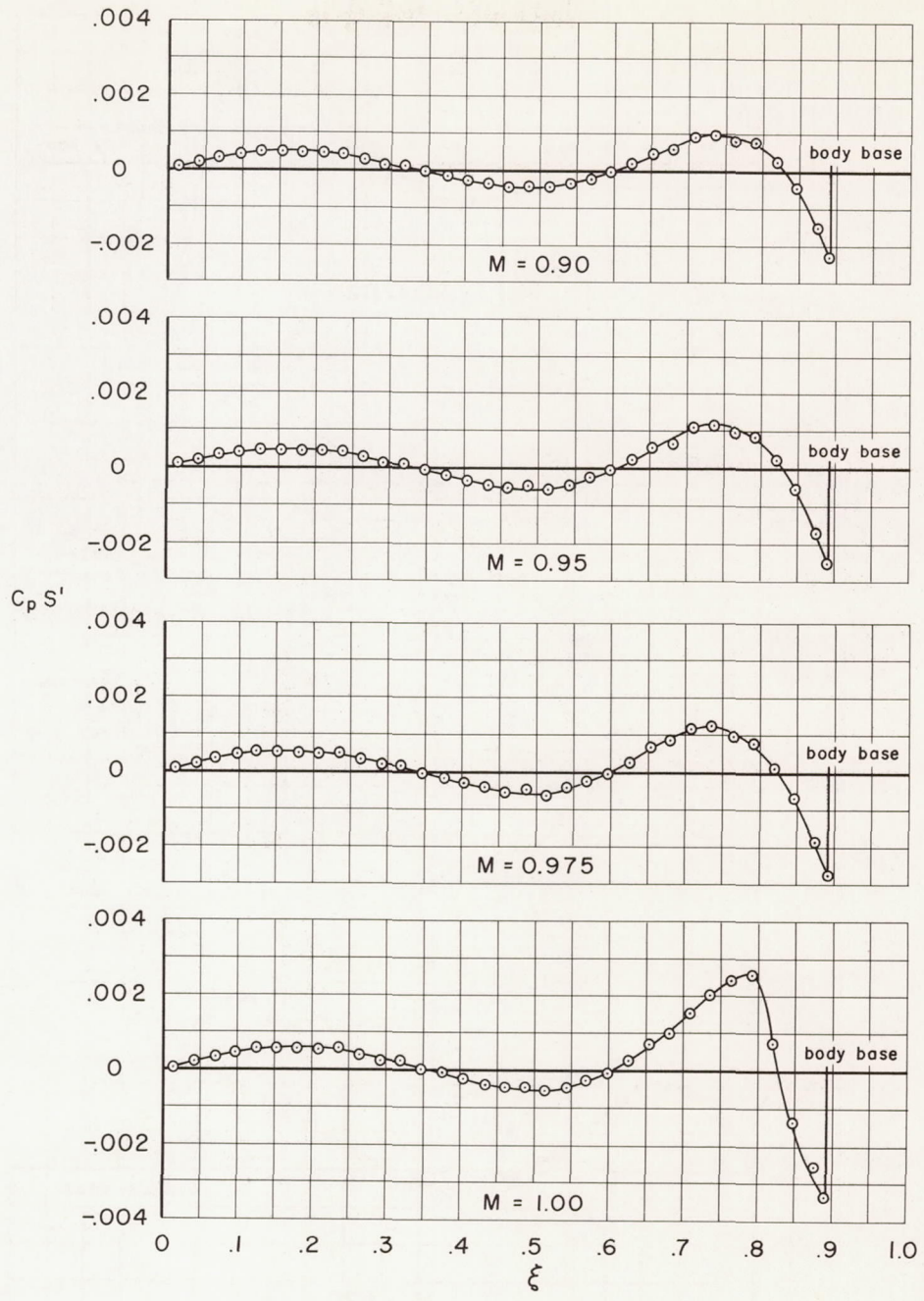

(a) M_∞ = 0.90, 0.95, 0.975, and 1.00

Figure 21.- The variation of $C_p S'$ with ξ for the body with maximum cross-sectional area at $\xi = 0.6$.

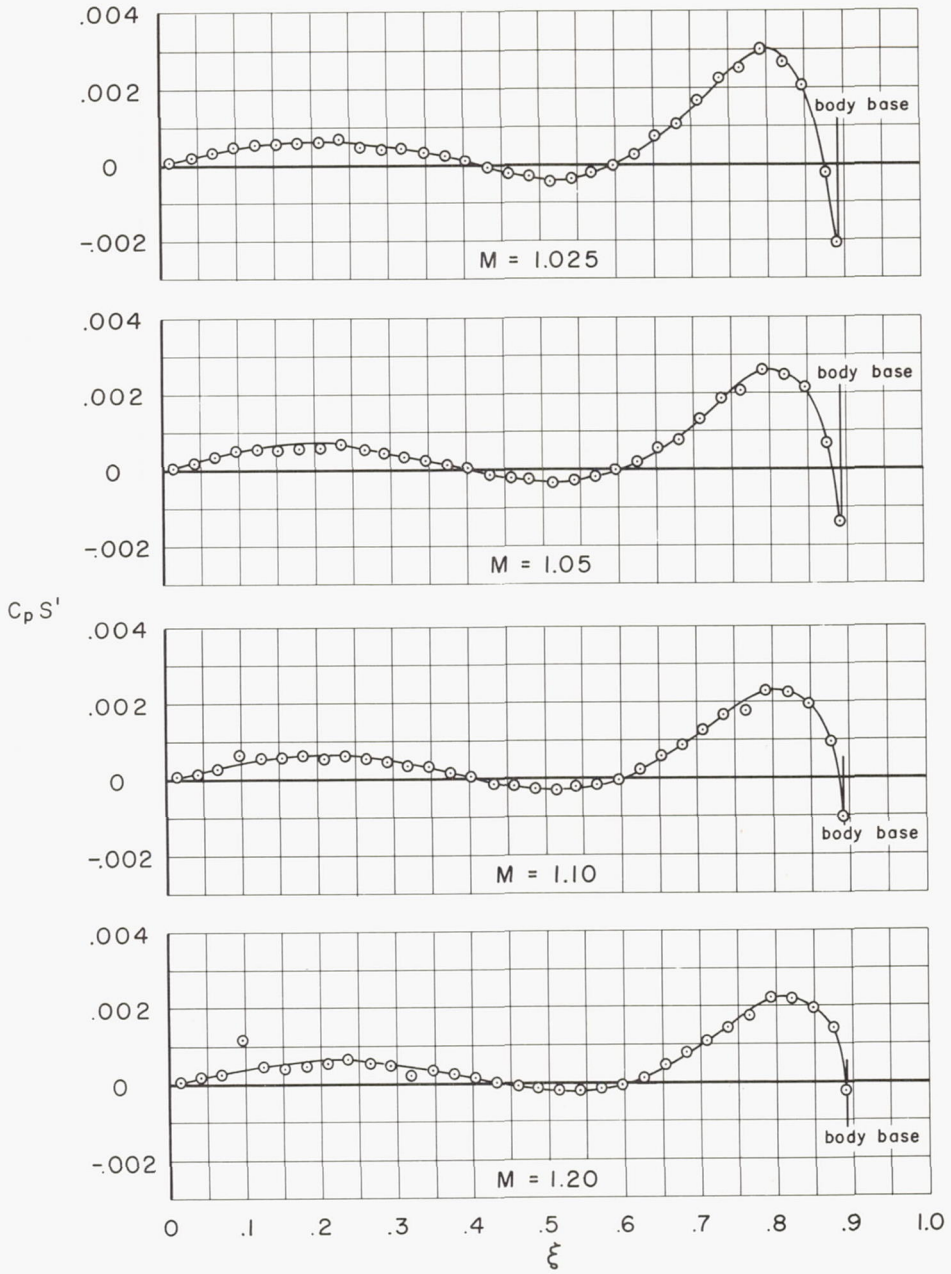

(b) M_∞ = 1.025, 1.05, 1.10, and 1.20

Figure 21.- Concluded.

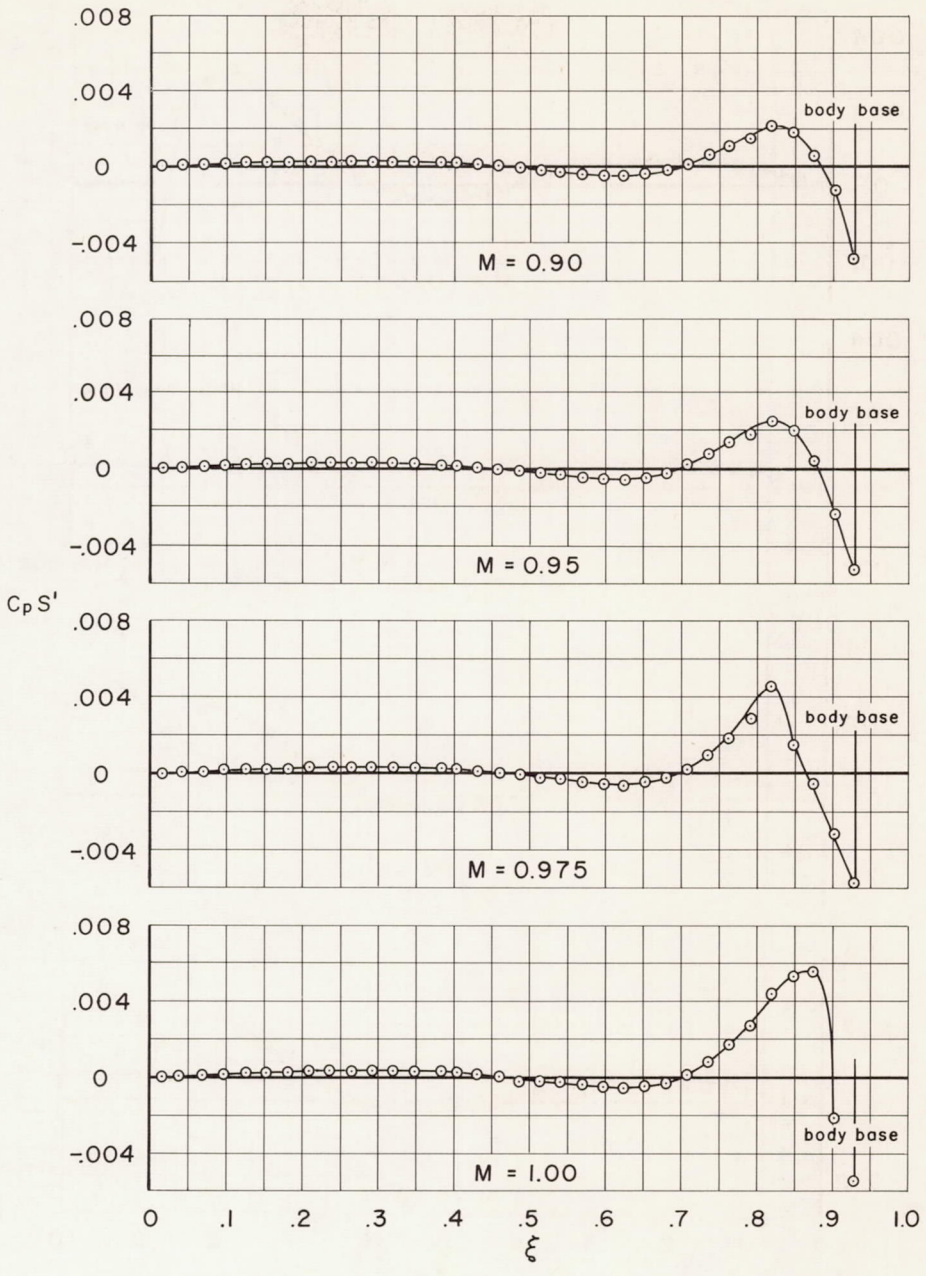

(a) M_∞ = 0.90, 0.95, 0.975, and 1.00

Figure 22.- The variation of $C_p S'$ with ξ for the body with maximum cross-sectional area at ξ = 0.7.

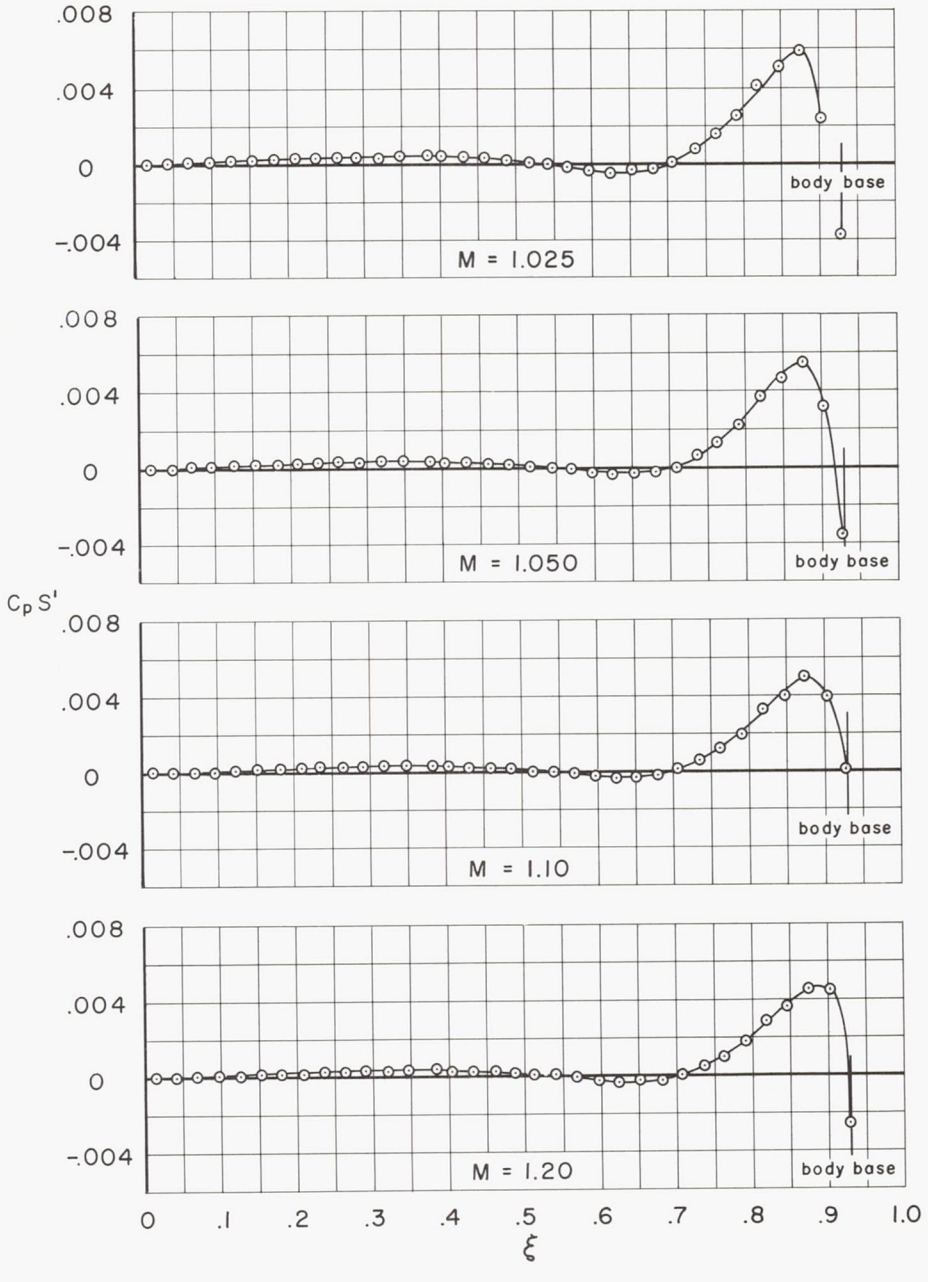

(b) M_∞ = 1.025, 1.05, 1.10, and 1.20

Figure 22.- Concluded.